MODELLING AND CONTROL OF 3D FLAPPING FLIGHT

A THESIS SUBMITTED TO
THE GRADUATE SCHOOL OF NATURAL AND APPLIED SCIENCES
OF
MIDDLE EAST TECHNICAL UNIVERSITY

BY

ÖZGÜN ÇALIŞ

IN PARTIAL FULFILLMENT OF THE REQUIREMENTS
FOR
THE DEGREE OF MASTER OF SCIENCE
IN
AEROSPACE ENGINEERING

FEBRUARY 2022

Approval of the thesis:

MODELLING AND CONTROL OF 3D FLAPPING FLIGHT

submitted by **ÖZGÜN ÇALIŞ** in partial fulfillment of the requirements for the degree of **Master of Science in Aerospace Engineering, Middle East Technical University** by,

Prof. Dr. Halil Kalıpçılar
Dean, Graduate School of **Natural and Applied Sciences**

Prof. Dr. Serkan Özgen
Head of the Department, **Aerospace Engineering, METU**

Prof. Dr. Dilek Funda Kurtuluş
Supervisor, **Aerospace Engineering, METU**

Asst. Prof. Dr. Kutluk Bilge Arıkan
Co-Supervisor, **Mechanical Engineering, TEDU**

Examining Committee Members:

Prof. Dr. Ozan Tekinalp
Aerospace Engineering, METU

Prof. Dr. Dilek Funda Kurtuluş
Aerospace Engineering, METU

Asst. Prof. Dr. Kutluk Bilge Arıkan
Mechanical Engineering, TED Uni.

Asst. Prof. Dr. Ali Emre Turgut
Mechanical Engineering, METU

Asst. Prof. Dr. Amir Nobahar Sadeghi Nam
Mechatronics Engineering, Atılım Uni.

Date: 02.02.2022

I hereby declare that all information in this document has been obtained and presented in accordance with academic rules and ethical conduct. I also declare that, as required by these rules and conduct, I have fully cited and referenced all material and results that are not original to this work.

Name, Last name : Özgün Çalış

Signature :

ABSTRACT

MODELLING AND CONTROL OF 3D FLAPPING FLIGHT

Çalış, Özgün
Master of Science, Aerospace Engineering
Supervisor: Prof. Dr. Dilek Funda Kurtuluş
Co-Supervisor: Asst. Prof. Dr. Kutluk Bilge Arıkan

February 2022, 119 pages

This thesis presents aerodynamic modelling, dynamical modelling and control studies on a flapping-wing micro air vehicle flight. The wing morphology and kinematics of nature flyers are investigated, and an aerodynamic model is created based on quasi-steady estimations and blade element theory. The model in question calculates the aerodynamic forces and pitching moment created by the flapping motion in a much shorter time than the alternating techniques, making it usable during control simulations. This model is used for realizing different flapping-wing micro air vehicles control simulations. The employability of the linear control methods such as linear quadratic regulator, and the coefficient diagram method, are tested in 2D longitudinal flight considering ideal actuator models. The 3D flight is controlled with active disturbance rejection controller by including realistic motor models and uncertainties at the wing model. Central pattern generators, biological neural networks responsible for generating rhythmic motions, are studied to achieve a bio-inspired control. A central pattern generator model is implemented into an active disturbance rejection controller based controller, bringing agility to the future bioinspired flapping-wing micro air vehicles during obstacle and danger avoidance.

Keywords: ADRC, Bio-inspired Control, Coefficient Diagram Method, Flapping-Wing MAV, Hawkmoth, LQR, Quasi-steady approach

ÖZ

KANAT ÇIRPARAK UÇUŞUN 3B MODELLEMESI VE KONTROLÜ

Çalış, Özgün
Yüksek Lisans, Havacılık ve Uzay Mühendisliği
Tez Yöneticisi: Prof. Dr. Dilek Funda Kurtuluş
Ortak Tez Yöneticisi: Dr. Kutluk Bilge Arıkan

Şubat 2022, 119 sayfa

Bu çalışmada bir çırpan kanatlı mikro hava aracının aerodinamik modellemesi, dinamik modellemesi ve kontrolü çalışmaları sunulmaktadır. Doğal uçucuların kanat morfolojisi ile kinematiği incelenmiştir ve yarı-sabit yaklaşım ve pala elementi metoduna dayalı bir aerodinamik model yaratılmıştır. Bahsi geçen model kanat çırpma hareketinden doğan aerodinamik kuvvetleri ve yunuslama momentini alternatif tekniklere göre çok daha kısa sürelerde hesaplamaktadır ve bu sebeple kontrol simülasyonlarında kullanılmak için uygundur. Bu model farklı çırpan kanatlı mikro hava aracı kontrol benzetimlerinin gerçekleştirilmesinde kullanılmıştır. Lineer kuadratik regülatör (linear quadratic regulator) ve katsayı diyagram yöntemi (coefficient diagram method) gibi doğrusal kontrol yöntemlerinin kullanılabilirlikleri 2 boyutlu boylamsal uçuş için ideal eyleyiciler kullanıldığı varsayılarak test edilmiştir. 3 boyutlu uçuş kontrolü, gerçekçi motor dinamikleri ve kanat modelindeki belirsizlikler de hesaba katılarak, doğrusal aktif bozucu girdi telafi denetimcisi (linear active disturbance rejection controller) ile yapılmıştır. Biyo-esinlenmiş denetimci yapıları elde etmek için ritmik hareketlerin üretiminden sorumlu biyolojik sinir ağları olan merkezi desen üretgeçleri (Central pattern generators) üzerinde çalışılmıştır. Bir merkezi desen üretgeç modeli, aktif bozucu girdi telafi denetimcisi temelli denetimci yapısına uygulanmıştır. Bu sayede biyo-esinlenmiş çırpan kanatlı mikro hava araçlarına engelden ve tehlikeden kaçarken çabukluk kazandırılmaktadır.

Anahtar Kelimeler: ADRC, Biyoesinlenmiş Control, Katsayı Diyagram Yöntemi, Çırpan Kanatlı Mikro Hava Aracı, Güve, Lineer Kuadratik Regülatör, Yarı-Sabit Yaklaşım

To My parents Ali Rıza and Nadide Gülen Çalış

ACKNOWLEDGMENTS

First of all, I am very grateful for the help, encouragement, and everlasting support of my advisor Prof. Dr. Dilek Funda Kurtuluş. She was not only a thesis advisor to me but a confidant, an idol, and a great guide about any issue. I always admire her integrity, rightness, and will to work for the sake of humanity.

I want to thank my thesis co-advisor Asst. Prof. Dr. Kutluk Bilge Arıkan for his advice, criticism, motivation, and brotherhood from my undergraduate education until the end of my thesis studies. It would be impossible to complete this work without his guidance. Also, his sense of morality was and always will be a path for me to achieve my goals.

I want to thank my parents, Ali Rıza and Nadide Gülen Çalış, my hugest chances in this life who were always there for me both for moral and material support. I could not have achieved any of my objectives without them.

I thank my labmates Altuga, Can, Gülay, Mürvet, Tawfiq, and Yudum for their friendship, support, and contributions. I thank my grandmom, aunts, uncles, cousins and friends.

This work was supported by TUBITAK (Project Number: 116M273).

I want to proceed in Turkish after this point.

Son olarak, bu çalışmayı gerçekleştirmemi mümkün kılan bütün kahraman ve şehitlerimize ve değişmez hedefi bize gösteren Gazi Mustafa Kemal Atatürk'e saygı ve minnetimi belirtmek istiyorum.

TABLE OF CONTENTS

LIST OF TABLES

TABLES

LIST OF FIGURES

FIGURES

CHAPTER 1

INTRODUCTION

Unmanned Aerial Vehicles (UAVs) are commonly used in applications such as ISR (intelligence, surveillance and reconnaissance) operations, military operations, rescue operations, and mapping (Newcome, 2004; Everaerts, 2008; Blom, 2010). Compared to manned vehicles, UAVs are more agile, have longer operation duration, low operational costs, work quiet, have low radar cross-section, and, most importantly, do not risk operators' or pilots' lives. With these advantages, accuracy and the precision of the operations are significantly increasing. Moreover, UAVs usage in civil (hobby and commercial) applications is increasing fastly.

UAVs are classified according to their wing types as fixed and rotary-wing UAVs. In recent years, with the development of Micro Air Vehicles (MAVs), flapping-wing MAVs have also become an area of interest. Examples for fixed wing, rotary wing, and flapping-wing MAVs are shown in Figure 1.1.

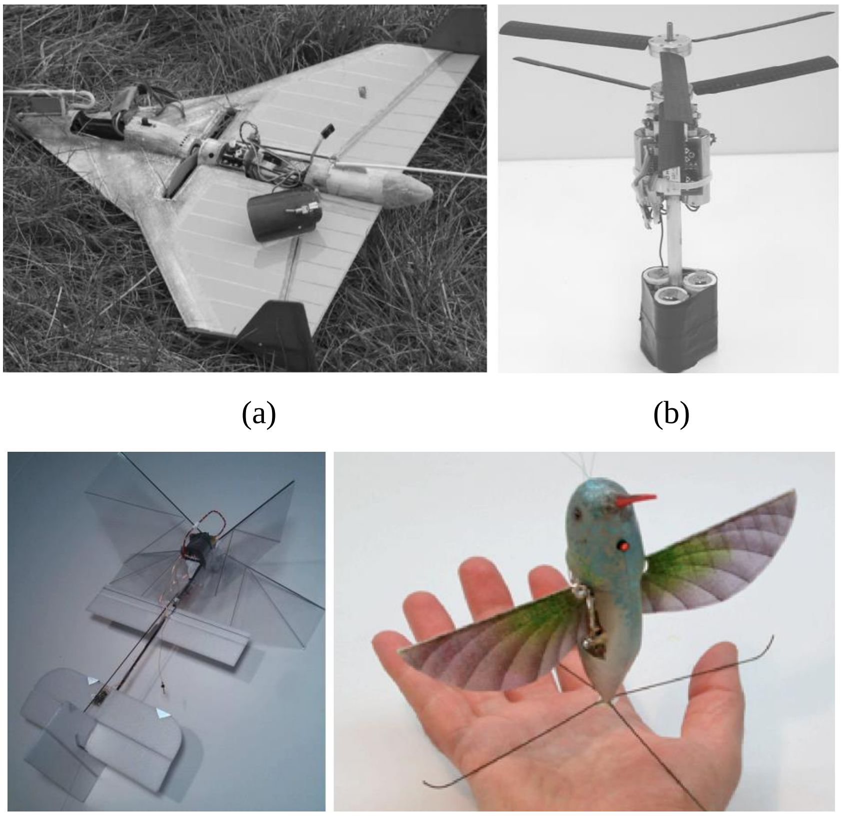

(a) (b)

(c) (d)

Figure 1.1: Different Types of Micro Air Vehicles (a) Fixed Wing (Galiński, 2006) (b) Rotary wing (Bohorquez et al., 2003) (c) Tailed Flapping-wing (Verboom et al., 2015) (d) Flapping-Wing (Keennon et al., 2012)

According to the definitions at Defense Advanced Research Projects Agency (DARPA) program, flapping-wing MAVs are aerial vehicles that have a mass of less than 100 g and wingspan length less than 15 cm (McMicheal & Francis, 1997). They are biologically inspired robots that imitates flying insects and birds such as hummingbirds. The advantages of flapping-wing MAVs are their high agility, small size, quietness, and capability of hovering, making them suitable for operations that require high maneuverability and precision (Kurtulus, 2011a; Kurtulus, 2011b; Okmen et al., 2021). Because of these influences, after 2008, flapping-wing MAVs have become a more popular research subject than other types of MAVs, and the number of conducted studies increased significantly (Ward et al., 2017). The primary purpose of these studies is to generate enough lift and thrust force to support the weight of a flapping-wing MAV and control the vehicle’s body using these forces. To achieve this, flapping-wing MAVs are examined in areas such as aerodynamics, control, navigation, structure, and material.

In this thesis work, two critical subjects for developing a flapping-wing MAV are studied, which are aerodynamics and control. The flapping motion of a flying insect is modelled, and using this model, aerodynamic forces created during the flight of a flapping-wing MAV are calculated. This model is implemented in the control architectures in order to actualize simulations with a realistic wing model. Different linear control strategies are followed to obtain a satisfactory result.

1.1 Literature Review

1.1.1 Flapping-wing Aerodynamics

The aerodynamic forces created by flying insects can not be calculated precisely using conventional aerodynamic approaches (Srygley & Thomas, 2002). This is because the aerodynamic characteristic of flapping flight differs from the helicopters and airplanes (Kurtulus, 2011a). Unlike the conventional aircraft flight, the flow at flapping flight occurs at low Reynolds numbers and high angles of attack (Frank, 2011; Kurtulus, 2015). Additionally, the flow is highly unsteady, and several unsteady effects augment the created lift during flapping, i.e., leading-edge vortex, clap-fling mechanism, wake capture (Shyy et al., 2013). Therefore, it is essential to study the low Reynolds number aerodynamics for MAV applications (Kurtulus et al., 2004; Kurtulus et al., 2005; Kurtulus et al., 2006a; Kurtulus et al., 2006b; Kurtulus, 2021; Kurtulus, 2022). Kurtulus (2018) investigated unsteady aerodynamic forces on a NACA 0012 airfoil pitching with sinusoidal oscillations and compared the results with steady airfoils at Re=1000. It is concluded that the flow is highly unsteady with the oscillating airfoil compared to the steady airfoil. On the other hand, even with the small amplitudes, the pitching frequency is deterministic also for the vortex shedding patterns but not only the magnitude of the aerodynamic forces (Kurtulus, 2019). The camber effect on unsteady aerodynamics at Re=1000 are investigated by studying on different cambered airfoils (Ahmed & Kurtulus, 2021).

1.1.1.1 Leading Edge Vortex

During the flapping flight, leading-edge vortex occurs on the top of the wing along the wing's leading edge, which causes the lift to increase (Frank, 2011; Lentink, 2013). During the stroke, the air is sucked into the vortices and decreases the pressure at the top of the wing, which yields an increased lift (Koehler et al., 2011). Meanwhile, the axial flow stabilizes the leading-edge vortex and, the vortex does not separate from the wing and causes any unsteady wake. (Dickinson et al., 1999; Sane, 2003) This way, the stable leading-edge vortex has a significant role in insect flight (Lehmann, 2004).

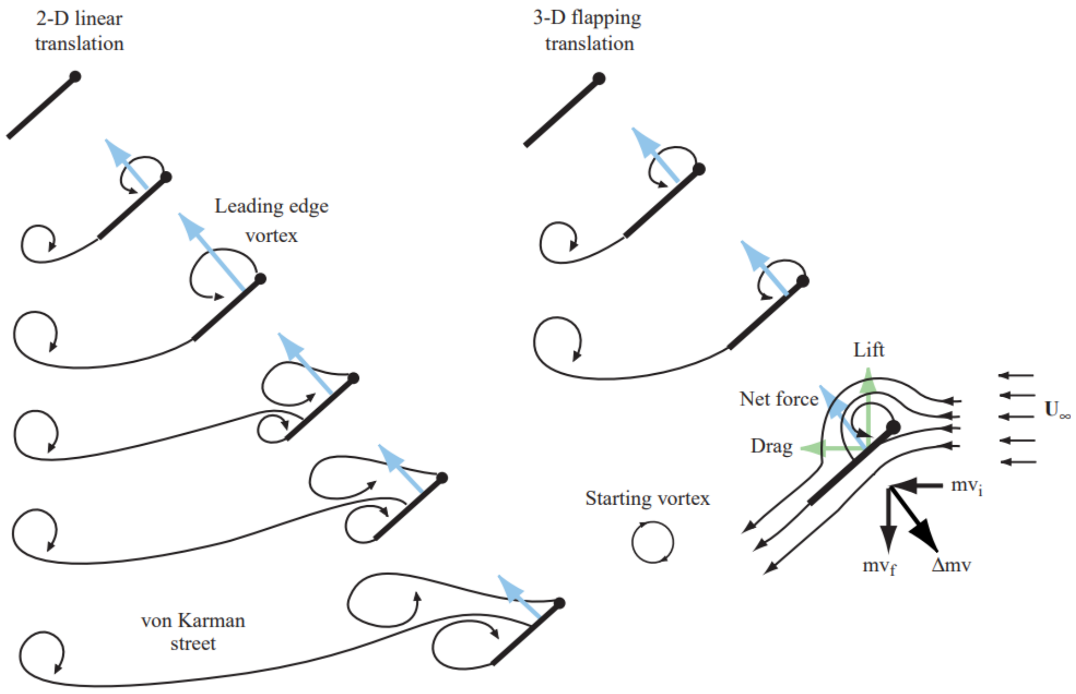

(a) (b)

Figure 1.2 Generation of leading edge vortex (a) 2D linear translation (b) 3D flapping translation (Sane, 2003)

Ellington (1996) visualized the leading-edge vortex caused during a Hawkmoth's downstroke and stated that they are the reason for the high generated lift. The experimental studies on Hawkmoths revealed that high angles of attack cause leading-edge vortex (Berg & Ellington, 1997). The leading-edge vortex tends to show up at angles of attack higher than 9° (Dickinson & Götz, 1993). Since the insects fly with angles of attack much higher than this value, the creation of a leading-edge vortex is inevitable and needs to be considered during aerodynamic calculations.

The subsequent studies also verified the influence of the leading-edge vortex on flapping flight (Kurtulus et al., 2008; Lentink & Dickinson, 2009).

1.1.1.2 Clap-and-Fling Mechanism

One of the lift enhancing action that some flying insects use is the clap-and-fling mechanism (Weis-Fogh, 1973). Insects use clap-and-fling mechanism mostly when they need high flight performance but not always (Marden, 1987). The lift is estimated to be augmented by the clap-and-fling mechanism by 12-15% (Lehmann, 2004). Some other studies suggest the influence of the clap-and-fling mechanism in lift production is even slightly more (Bennett, 1977; Marden, 1987; Lehmann et al., 2005). The influence of the clap-and-fling mechanism on aerodynamic performance becomes greater at lower Reynolds numbers (Miller & Peskin, 2005). Additionally, it is revealed that the fling phase has a more significant effect on lift enhancement than the clap phase, and with the shorter distance between the leading edges at the clap phase, the following fling phase has a more lift enhancing effect (Jadhav et al., 2019).

The clap-and-fling mechanism mainly begins at the beginning of downstroke but can also be effective at the beginning of downstroke (Lehmann et al., 2005). At the "clap" phase, the first touch between the two wings occurs at the leading edges. Subsequently, the trailing edges of the wings approach each other by rotating around the leading edge, forcing the air out from the gap between the two wings and gaining extra thrust. At the “fling” phase, the leading edges separate from each other first and create a gap between the two wings, followed by the air to fill in between the two wings. A more detailed description can be found (Shyy et al., 2013).

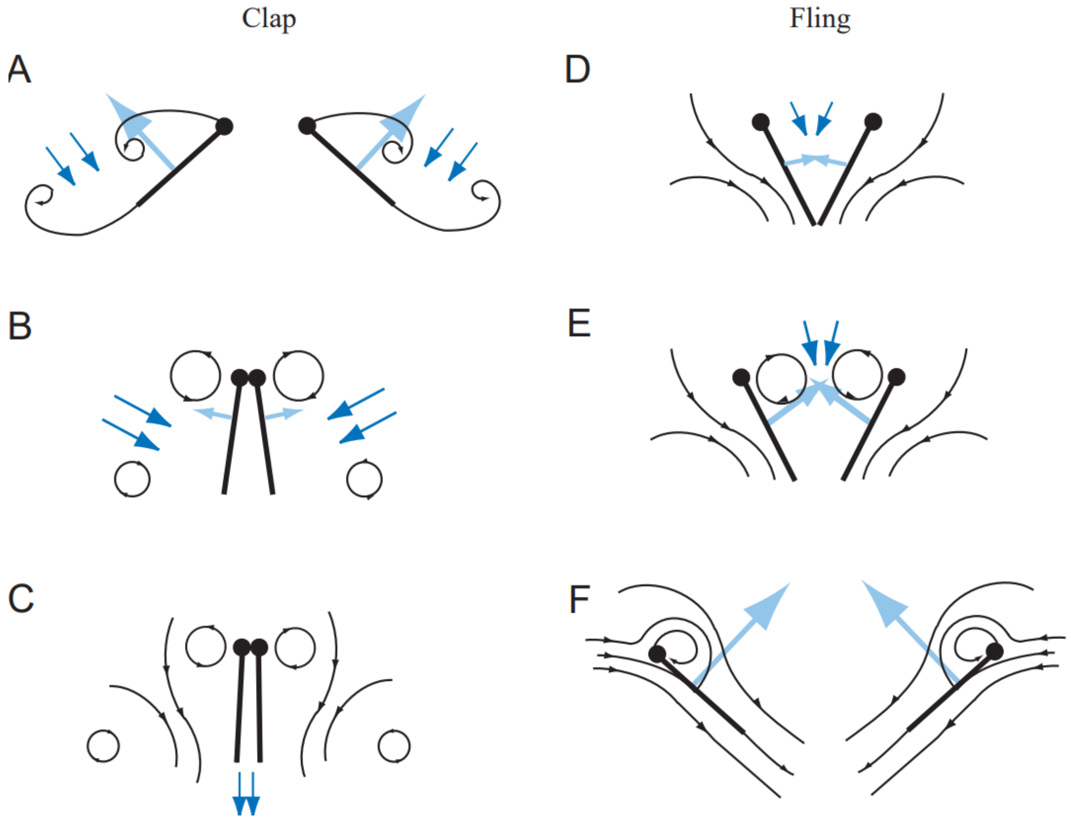

Figure 1.3 Illustration of clap and fling mechanism (A - C) illustrates the clap phase, (D - F) illustrates the fling phase. Black arrows, dark blue arrows, and light blue arrows represent flow lines, induced velocity, and net forces acting on the airfoil, respectively. (Sane, 2003)

1.1.1.3 Wake Capture

The wake capture is a lift-enhancing mechanism that mostly makes a difference during hovering (Tang et al., 2008). The wing creates wake towards the direction it moves during flapping. As the stroke reversal actualizes immediately with a rapid rotation, the wing meets the wake of the previous stroke with a positive angle of attack and thus, yields extra lift (Lehmann, 2004). At the stroke reversal, if the wing's rotation around the span actualizes with a delay, the wing may meet the wake with a negative angle of attack, which causes a negative lift (Dickinson et al., 1999). Dickinson et al. (1999) explain the wake capture mechanism as the energy passed from the wing through the surrounding fluid during a stroke and, following this, regaining some amount of this energy back again at the next stroke.

Lua et al. (2017) studied the effects of acceleration and deceleration durations on wake capture mechanism. Wang et al. (2018) investigated the effect of wake capture on aerodynamic performances at flapping motion with two ipsilateral wings using plates.

1.1.1.4 Added-Mass Effect

During the acceleration and deceleration of the wing, the wing also accelerates and decelerates the surrounding air. Consequently, a pressure acting on the wing occurs, and this effect is considered as additional wing mass and called the "added mass" effect (Chin & Lentink, 2016). When the wing's thickness is neglected, as it is going to be done in the current thesis study, the force acting on the wing due to added mass effect acts normal to the wing surface (Sane & Dickinson, 2002).

1.1.2 2D and 3D Flapping-wing Models

1.1.2.1 2D Flapping-wing Models

One can investigate the flapping kinematics in various motions: pure plunge, pure pitch, and combined plunge and pitch. Airfoils are commonly used to investigate the pure plunge motion (Ashraf et al., 2007; Kaya & Tuncer, 2007). Jones & Platzer (1997) studied different airfoils and revealed that, in the case of pure plunge motion, the thickness of the airfoil has no significant effect on propulsive efficiency.

Numerical investigations in the case of pure pitching motion are presented at (Lian, 2009). Tuncer & Platzer (2000) carried out numerical calculations of aerodynamic forces and flow separation characteristics at low-speed flows over a NACA 0012 airfoil by solving Navier-Stokes equations and using a particle tracing module in pure plunge and combined plunge and pitch motions. Better propulsion efficiency is found to be obtained in combined plunge and pitch motion. Esfahani et al. (2015) also used a NACA 0012 airfoil and concluded that forward motion has a significant thrust enhancing effect on pure plunge motion, whereas it has no significant effect on combined pitch and plunge motion. Ramamurti et al. (2001) investigated the combined plunge and pitch motions and showed that the Strouhal number is significantly related to the force generation during flapping.

1.1.2.2 3D Flapping-wing Models

Many experimental and numeric studies have been conducted with various 3D wing models such as flat plates, real insect wings, aeroelastic wings, veined wings, and cambered wings to explore the perfection behind insect flight.

Bektas et al. (2019) modelled a rigid hawkmoth Manduca sexta wing with no camber and calculated aerodynamic coefficients using computational fluid dynamics (CFD) under pure plunge motion. They revealed that positive lift is not created with pure plunge motion at zero angle of attack and with no camber. Shyy et al. (2009) conducted simulations with plunge and pitching motions, and numerical results show that leading-edge vortices have significant effects on lift enhancing during hawkmoth flight, meanwhile the tip vortices may have little impact on flapping-wing aerodynamics.

Zhang et al. (2010) modelled a flexible flapping flat plate and conducted studies in various aspects in the meaning of dynamical behaviors. Du & Sun (2008) studied the effects of twist and camber deformation of flat plates on aerodynamic performances and concluded that the influence of camber deformation is much more considerable than the twist deformation. Trizila et al. (2011) modelled 2D and 3D flapping motions with flat plates and investigated the role of unsteady effects on flapping flight. Flat plate wing models are still being used to investigate aerodynamics of flapping flight (Jones et al., 2016; Krishna et al., 2018;).

Getting inspired from hawkmoth Manduca sextas, veined wing models are created and influence of vein structures on aerodynamic performance and strength of the wing are examined (Agrawal & Agrawal 2009; Sims et al., 2010; Nakata & Liu, 2011; Nguyen & Han 2018). Bektas (2020) conducted CFD analyses with both flat and veined Manduca sexta wing models and showed that the lift increases significantly when vein structure is included at the wing's leading edge. Agrawal & Agrawal (2009) experimentally tested rigid and flexible synthetic veined wings with similar load-deformation characteristics with an MS wing. They measured more thrust with the flexible wing than the rigid wing, and they suggested that flexible wings might have more advantages in aerodynamic performance.

Au et al. (2020) investigated the aerodynamic performances of a cambered wing for different corrugation profiles. They suggested that using a proper corrugation profile can augment the wing's stiffness and replace veined structures. Engels et al. (2020) suggested that corrugation has resistance enhancing impact against extreme wing loading rather than aerodynamic performance increasing effects.

Bektas et al. (2020) used CFD and analyzed the aerodynamic and aeroelastic characteristics of a 3D hawkmoth Manduca sexta wing with various materials. They considered steady flow conditions and analyzed several angles of attack between 0° and 90°.

1.1.2.3 Unsteady Aerodynamic Modelling

Aerodynamic forces and moments change in time during the flapping motion of the wing. To calculate the effects of the wing-flapping motion on the aerodynamic forces and moments with high precision, unsteady computational fluid dynamics (CFD) analyses are being used in recent years (Sun & Tang, 2002; Hsu et al., 2010; Nakata et al., 2015; Bektas et al., 2019). Liu & Aono (2009) carried out numerical calculations on hovering insects’ wings in different sizes and discussed the Reynolds number effects on aerodynamic forces and unsteady effects during the flight.

However, since the CFD analyses take too much time, it is hard to use them in the control algorithms.

The hardness of getting Navier-Stokes equations’ solutions, required the use of different models and approaches in flapping-wing MAVs. Some of the most common ones of these models are Wagner and Theodorsen functions' usage at calculating the unsteady aerodynamic coefficients approximately (Kurtulus, 2005). These functions are first introduced at (Wagner, 1925; Theodorsen, 1935). With these functions, the instantaneous changes in stroke angles and harmonic motion of the airfoil are considered (Bisplinghoff & Ashley, 1996).

Küssner function is one of the unsteady aerodynamic models first proposed by (Küssner, 1936). With the Küssner function, dimensionless aerodynamic forces and moments are approximately computed in the existence of a vertical step gust instantly acting on the leading edge of a flat-plate airfoil where the airfoil has horizontal speed through the gust region (Cebeci et al., 2005).

Using Wagner and Küssner functions, Kurtulus et al. (2005) estimated the aerodynamic forces under the combined plunge and pitching motion of a NACA 0012 airfoil close to the numerical results, and they obtained positive lift above 30° angle of attack when the motion is symmetrical.

Alternative aerodynamic models based on the indicial approach for unsteady motions exists in the literature (Beddoes, 1984; Zbikowski, 2002; Leishman, 2002). A method for predicting unsteady aerodynamic forces on a flapping-wing preferred in several studies is the unsteady panel method (Mantia & Dabnichki, 2009; Roccia et al., 2013). The unsteady panel methods are based on some assumptions but have lower computational costs than numerical simulations (Katz & Plotkin, 2001). Han & Nguyen (2017) compared the unsteady panel method with quasi-steady and CFD methods. They concluded that the panel method is applicable for dynamic stability problems because of its relatively accurate estimations than quasi-steady approach and low computational costs than CFD.

The unsteady vortex lattice method is a numerical method for modelling and calculating the unsteady aerodynamics around a lifting surface (Konstadinopoulos et al., 1985; Long & Fritz, 2004). Simpson et al. (2013) proposed an unsteady vortex lattice method that includes the leading-edge suction effects to calculate induced drag accurately. Nguyen et al. (2016) used the unsteady vortex lattice method, together with leading-edge suction analogy and vortex-core growth models, to calculate aerodynamic forces of an insect at hover and forward flight by including wing-wake interactions. They validated the proposed method by simulating the hawkmoth Manduca sexta wing, and calculations had good agreement with CFD and experimental results.

Using the method proposed by Nguyen et al. (2016), Lee et al. (2018) calculated the aerodynamic forces by considering the unsteady effects. They then used this model to control the longitudinal dynamics of a flapping-wing MAV for trimmed conditions at hover and forward flight.

As an alternative to these studies, a further straightforward approach for calculating the aerodynamic forces and moments is the quasi-steady approach.

1.1.2.4 Quasi-Steady Approach

The quasi-steady approach is preferred in many studies at modelling flapping-wing MAV due to its advantages in terms of simplicity and speed (Sane & Dickinson, 2002; Madangopal et al., 2006; Karasek & Preumont., 2012a; Karasek & Preumont., 2012b; Lee et al., 2015; Banazadeh & Taymourtash, 2016). However, with a quasi-steady model, unsteady aerodynamic forces and moments that occur with parameters like flapping frequency, stroke angle, etc. are calculated with various assumptions. (Wright & Cooper, 2015). Another disadvantage of using quasi-steady method is that wing-wing and wing-body interactions cannot be considered (Bhatia et al., 2012). Pohly et al. (2018) stated that using a quasi-steady approach for modelling a flapping motion might be insufficient when the wing's rotation movements are sharp and fast.

However, if the rotation occurs smoothly, very close results to the ones obtained with Navier-Stokes equations can be reached via a quasi-steady approach.

Han & Han (2019), stated that the contralateral wing has a significant stabilizing effect in the lateral plane in the existence of a lateral gust. The vortex that occur during a wing beat causes an extreme angle of attack for the next beat. On the other hand, the downwash created by the contralateral wing prevents the formation of high angles of attack by attenuating the effect of the vortex. In this way, excessive aerodynamic forces do not ocur. Since the downwash caused by the contralateral wing cannot be considered with single wing analyses, much higher aerodynamic forces than the actual flight case are calculated. Han & Han (2019) has revealed that quasi-steady assumptions give more realistic results in single-wing evaluations than unsteady methods since one cannot model vortices as well as downwash with quasi-steady assumptions. For this reason, if the wing-wing interactions are not considered, using quasi-steady approach during lateral stability analyses may give more realistic results than the unsteady aerodynamic models.

The delayed stall and the Wagner effect are two effects that cannot be modelled with the quasi-steady approach and have adverse effects on each other (Weis-Fogh, 1973). Since some of the effects that cannot be modelled with a quasi-steady approach have counteracting and passivating effects, quasi-steady estimations are sufficient, especially for dynamic stability analysis and control structure designs (Taha et al., 2012).

Although the blade element approach with quasi-steady aerodynamic coefficients cannot model the effects of the wake capture effect, it is seen that the results obtained with this method are close to the experimental data (Sane & Dickinson, 2002). The effect of wake capture is negligible when the velocity of the vehicle is constant (Liang et al., 2020). Taha et al. (2012) stated that using quasi-steady model is suitable since the effects of unsteady aerodynamics are usually opposite and neglecting each other.

Wang et al. (2004) compared experimental, computational and quasi-steady results of a flapping-wing for three cases. While calculating the lift, the quasi-steady calculations gave slightly closer results to the experimental data than the computational results with the case in which there is no phase delay between the rotation and translation of the wing. However, the quasi-steady estimations underestimated the magnitudes of the lift and drag coefficients in other cases.

Wissa et al. (2020) implemented a quasi-steady aerodynamic model in a nonlinear controller to control a flapping-wing MAV. Al-Mahasneh et al. (2017) calculated aerodynamic forces with quasi-steady assumptions. Banazadeh & Taymourtash (2016) used quasi-steady assumptions to calculate aerodynamic forces at the study where an adaptive attitude and position controller for a hummingbird-like flapping-wing MAV is designed.

Kim et al. (2015) proposed a model that calculates the lift, drag, and pitching moment of an insect's flight using blade element theory with quasi-steady estimation. They divided a Hawkmoth wing into five equal strips along the span and calculated aerodynamic forces on each strip independently by considering their effects at wing roots. Unsteady effects are also considered during rotational forces calculations.

1.1.3 Dynamical Modelling and Control

Stroke plane angle is parallel to the ground and 0° for most of the insect flights during hovering (Sun, 2014); however, as the stroke plane angle increases, especially at angles more than 24°, stability of the flight increases (Xu & Sun, 2014). Hawkmoths create roll moments and tilt their body to move their body laterally. To create roll moment, they produce asymmetric lift by increasing the lift at the roll-contralateral wing and decrease the lift at the roll-ipsilateral wing. They increase the aerodynamic force produced by increasing the stroke amplitude and decrease the aerodynamic force by reducing the stroke amplitude (Greeter & Hedrick, 2016).

While the longitudinal and the lateral dynamics of flapping-wing MAVs are decoupled from each other, coupled effects exist within the longitudinal and lateral dynamics. The longitudinal dynamics can be controlled by using symmetrical changes in wing kinematics, while the lateral dynamics can be controlled by changing the wing kinematics asymmetrically (Kim & Han, 2013). Flapping frequency, mean pitching angle, mean stroke angle are the possible controls for longitudinal plane (Kim et al. 2015).

Keennon et al. (2012), actualized the flapping motion of two wings with a single motor. The study is conducted such that the roll, pitch and yaw control moments are obtained by creating asymmetrical aerodynamic forces with two wings. They used two different approachs to create control moments. In one strategy, adjustable stoppers that limit the pitching amplitude are used in which the aerodynamic forces are increased by increasing the flapping amplitude and decreased by decreasing it. In the other strategy, the wings are twisted with an adjustable rod that yields changes in the aerodynamic forces. Garcia et al. (2003) also controlled yaw motion by twisting the wing, and they stated that morphing is an effective way for controlling the roll maneuvers.

Sun & Wang, (2007) stated that the longitudinal dynamic stability of a hovering insect can be provided by feeding back pitch attitude, pitch rate, horizontal velocity and vertical velocity. The study suggested that even though the system's stability is desirable during hovering, to achieve a quick maneuver, switching of the controller that is assuring stability might help improve the agility. A similar study is also conducted by Xiong & Sun, (2009).

1.1.3.1 Linear Controllers

Different kinds of control approaches such as the Linear Quadratic Regulator (LQR), the Coefficient Diagram Method (CDM), Proportional-Integral-Derivative (PID) and Linear Active Disturbance Rejection Controller (LADRC) are available to deal with linear dynamical systems with perturbative inputs.

LQR control is preferred to stabilize flapping-wing MAVs in different studies (Bhatia et al., 2012; Biswal 2015; Lee et al., 2015; Zhang et al., 2016; Calis et al., 2019; Calis et al., 2021).

Deng et al. (2006a) studied flapping-wing MAV’s flight modelling, wing kinematics, control of hover flight, and actuator dynamics. Deng et al. (2006b) linearized the flight around hovering condition and stabilized the system with an LQR controller. They also investigated the neuromotor structures and proposed a control mechanism inspired by flying insects' neuromotor control systems.

Biswal et al. (2019) modelled a flapping-wing MAV for three cases; first by considering only the rigid body dynamics, second including the rigid body dynamics and the wing kinematics, and third, including all the rigid body dynamics, wing kinematics, and the rigid wing dynamics. They designed an LQR controller for the first and the simplest case, and the controller's robustness is proven by being implemented in the other complex cases.

The coefficient diagram method (CDM) is used in different UAV applications (Hirokawa, 2004; Giernacki, 2017). However, no flapping-wing research has been met with this method in the literature.

It is also used for various control applications of Linear Time-Invariant (LTI) systems. Ma’arif et al. (2020) tested a controller with cascaded integral trackers that track challenging reference inputs such as parabolic and polynomial. They tuned the state feedback and integral gains using the coefficient diagram method, and the proposed method was able to track the reference inputs with no steady-state error.

PID controller is also a common approach in the field of flapping-wing MAV control (Hines et al., 2011; Nakatani et al., 2016; Zhang et al., 2016).

Nakatani et al. (2016) presented a flapping-wing MAV in which the pitch and yaw angles are controlled with PID and PI controllers. They certified the employability of both of the controller types in the existence of large disturbances. Similarly, Hines et al. (2011) controlled the pitch and yaw angles with a PID controller, and the altitude with another PID controller. Using a vision-based localization system as an altitude sensor, (He et al., 2017) controlled the altitude of a flapping-wing MAV with a PID controller, and the proposed method is found to be satisfactory. Fei et al. (2019) used cascaded PD and PID controllers for position control. The proposed controller performed well both in the simulations and the actual flight. Wenfu et al. (2021) employed PID controllers and fuzzy controller for position and attitude control of a bird-like flapping robot. They found the proposed controller reliable in the existence of highly coupled effects.

Linear Active Disturbance Rejection Controller (LADRC) has served well in several UAV control applications (Li et al., 2016; Qin et al., 2017; Suhail et al., 2019; Sun et al., 2020). Yu et al. (2019) compared the response of a PID-controlled small-scale unmanned helicopter with and without an ADRC. They found the ADRC including case to be better in compensating disturbances compared to the single PID case. Sun et al. (2021) proposed a fuzzy adaptive LADRC to deal with the coupling effects and nonlinear dynamics of a quadrotor. The fuzzy adaptive LADRC had faster responses with less overshoot than LADRC and even better responses than PID controllers.

There are very few examples in the literature for the usage of ADRC in the flapping-wing MAV control applications. One of them is the bat-like flapping-wing MAV proposed by Li et al. (2021). They developed an energy optimizing and disturbance rejecting controller based on ADRC for the longitudinal dynamic model. More studies prove the suitability of ADRC based attitude controllers for the robust control of tailed flapping-wing MAVs. (Bai et al., 2020; Liang et al., 2020).

1.1.3.2 Nonlinear Controllers

Rifai et al. (2008) stated that the linear control methods are insufficient in eliminating the external disturbances and proposed a nonlinear control method. The proposed controller was able to reject the disturbances applied to the angular position and angular velocity states of the flapping-wing MAV during simulations. Banazadeh & Taymourtash, (2016) presented a nonlinear model of a flapping-wing MAV. In the study, open loop dynamics of the 6 DOF system are observed for 20 wing beat period in MATLAB/Simulink and the system has been found to be unstable. An adaptive sliding mode controller is proposed, and the stability of the controlled plant is tested with the Lyapunov method. It is concluded that the adaptive, nonlinear controller was able to overcome the disturbances and uncertainties and is preferable in disturbance rejection to the non-adaptive nonlinear controllers. Chirarattananon et al. (2014) studied adaptive controllers for altitude, attitude, and lateral controls, and the stability has been proven with Lyapunov functions. Nonlinear models and the Lyapunov method are preferred in various studies at controlling flapping-wing MAV (Wissa et al., 2020; Hashemi et al., 2020). Ferdaus et al. (2018) developed an adaptive fuzzy controller with fuzzy c-means clustering technique and the error between the reference and the output, and its derivative are the inputs of the system. The proposed fuzzy controller is tested against a PID controller, and it was better at tracking the sinusoidal input with minor steady-state error and the step input with less overshooting and oscillations.

1.1.3.3 Central Pattern Generators

1.1.3.3.1 CPGs in Engineering Applications

In recent years, control methods developed based on central pattern generators (CPGs) have been used for locomotion control in some robotic studies (Sufiyan et al., 2020; Polykretis et al., 2020). Bal et al. (2019) proposed a system based on a CPG network and Fuzzy Logic controller that controls a robot fish's swimming and yaw motion to get an adaptive and robust closed-loop controller performance. Xie et al. (2019) produced the rhythmic swimming motion using a CPG model. The model has four parameters to be adjusted, and the cruise speed of the robot fish is controlled by changing the amplitude and the frequency. Chen et al. (2021) also proposed a bioinspired, closed-loop CPG-based control structure for a robot fish.

1.1.3.3.2 CPGs in Flapping-wing Applications

Various studies are conducted for CPG-based control of flapping-wing MAVs. Bayiz et al. (2019) created wing kinematics using a CPG controller to achieve smooth transitions of the rhythmic motions of the wing. In the study, each wing motion (stroke, deviation, pitching) is controlled with a separate servo motor. Chung & Dorothy (2010) modelled the wing kinematics and the body dynamics inspired from a bat, making stroke, deviation, and pitching motions. Vehicle dynamics are stabilized by controlling the flapping frequency and the phase difference between oscillators. They used Hopf oscillator based CPG’s as an alternative to sinusoidal input functions. A Lyapunov function is proposed to evaluate the asymptotical stability. Zhang et al. (2016) used Hopf oscillators to create rhythmic inputs and compared three controllers designed for flapping-wing MAV: a nonlinear, a PID, and an LQR controller. The nonlinear controller and the PID controller had better performances in tracking the reference inputs, while the LQR had less input effort. Usage of Hopf oscillator based CPGs as an alternative to sinusoidal inputs is common in bioinspired engineering applications (Wang et al., 2017; Cao et al., 2019).

1.2 Significance of the Study and the Thesis Outline

To manipulate and control their body, insects change the aerodynamic forces they create during flight. They manage this by altering wing kinematics instantly. This way, they handle sharp maneuvers when escaping the danger, stabilize their body in the existence of a gust, or orient their body. Therefore, to develop a flapping-wing MAV inspired by a flying insect, the aerodynamics of insect flight needs to be investigated. During these investigations, aerodynamic forces that are expected to occur during an artificial wing's flapping motion must be calculated. These calculated forces are to be used at stabilizing and navigating the flapping-wing MAV’s body. To do so, exhaustive control studies must be carried on.

To control the flapping-wing MAVs, several control methods such as PID, LQR, Generalized Regression Neural Network (GRNN) (Al-Mahasneh et al., 2017), Fuzzy Logic Controller (Ferdaus et al., 2018) have been used. However, even the Coefficient Diagram Method (CDM) success in controlling the aerial vehicles has been proven several times, any flapping-wing control studies using CDM have not been found in the literature so far. In the current study, besides using LQR, a common approach in controlling the flapping-wing MAVs, LADRC, a recently preferred control approach for flapping-wing MAVs, and CDM that is not used so far are tested for controlling the flapping flight.

In this study, an insect's flapping motion and body dynamics are modelled, and these models are used to develop a controller for a flapping-wing MAV. Hawkmoth Manduca Sexta (MS), a commonly used insect species in bio-inspired flapping-wing MAV studies, is chosen to be worked on. The wing morphology and the changes in wing kinematics during hovering, forward flight, and maneuvering of a hawkmoth are studied.

In the first chapter, the importance and preliminary information about the flapping-wing MAV technology and the previous studies about the flapping-wing MAV are given by focusing more on the aerodynamics and control applications. In the second chapter, hawkmoth's wing morphologies and kinematics are investigated. The flapping motion of hawkmoth MS is modelled in MATLAB, and aerodynamic forces are calculated with quasi-steady assumptions and the blade element method. An aerodynamic model is developed to calculate the aerodynamic forces and pitching moment as the wing kinematics and body velocities change during flight. The aerodynamic model is validated by comparing its results with CFD and experimental results for different wing scales and kinematics found in the literature. This model calculates the forces produced by the flapping motion in much shorter times than

CFD simulations or experimental methods. The third chapter gives 2D and 3D modelling of a flapping-wing MAV, including the moment of inertia calculations and actuator dynamics. Different linear control strategies are followed during stability and control studies. For the 2D flight simulations, LQR control and CDM control-based applications are used to stabilize the unsteady dynamics of a flapping-wing MAV. The aerodynamic model developed in the second chapter is linearized around the hovering condition and included in the simulations. Subsequently, an integral tracker is designed for the system to track the reference commands. For the 3D flight, an active disturbance rejection controller (ADRC) is used that provides robust responses even the mathematical model of the controlled plant does not exist. This time, the nonlinear aerodynamic model is implemented into the control structure. The aerodynamic model used in control simulations can also easily be used with different wing shapes and dimensions or different flight conditions, making testing further control approaches very easy, which is one of the study's achievements. Bio-inspired controllers based on central pattern generators (CPGs) are studied. Artificial CPG models are created and implemented into the control structures. The fourth chapter gives the simulation results and evaluations of the controllers’ performances developed in the third chapter. LQR, CDM, ADRC, and the CPG-based controller performances are all given in this chapter. The fifth chapter gives final evaluations of the work done and arguments of the obtained results. In the sixth chapter, future works to be done and the parts that need improvement are discussed.

Within the scope of this study, an aerodynamic model that calculates forces due to the flapping motion much faster than the alternating techniques is developed. This rapidity in calculations allows the model to be used in control simulations. The performance of CDM is investigated for a flapping-wing MAV simulation for the first time in the literature and proved against disturbances. A bio-inspired controller is suggested using ADRC, which is prominent with its disturbance rejection capabilities.

CHAPTER 2

AERODYNAMIC MODELLING

2.1 Coordinate Definitions

Four coordinate frames that are orthonormal and right-handed coordinate frames are introduced to clarify the wing kinematics and the body dynamics. The Global Frame (X_G, Y_G, Z_G), as shown in Figure 2.1a is fixed to any point on Earth; the X_G-axis is pointing the North, the Z_G-axis is pointing the center of the Earth, and the Y_G-axis is through the out of the page. The Body Fixed Frame (X_B, Y_B, Z_B), as shown in Figure 2.1a , is fixed to the point B, which is the center of gravity of the whole body, the X_B-axis is along the insect's body, initially making an angle θ with X_G-axis. The Z_B-axis is perpendicular to the X_B-axis, as shown in Figure 2.1a , and the Y_B-axis is throughout the page. The Stroke Plane Frame (X_{sp}, Y_{sp}, Z_{sp}) is used as a reference to the flapping motion. X_{sp}-axis initially makes an angle β with the X_G-axis and points the direction of the downstroke motion. Wing Fixed Frame (X_W, Y_W, Z_W) is fixed to the wing root, as shown in Figure 2.1c. The X_W-axis is throughout the chord, the Z_W-axis is along the span and pointing the wingtip, and the Y_W-axis is through inside of the page, satisfying the right-hand rule. The wing is attached to the body from the wing root (O).

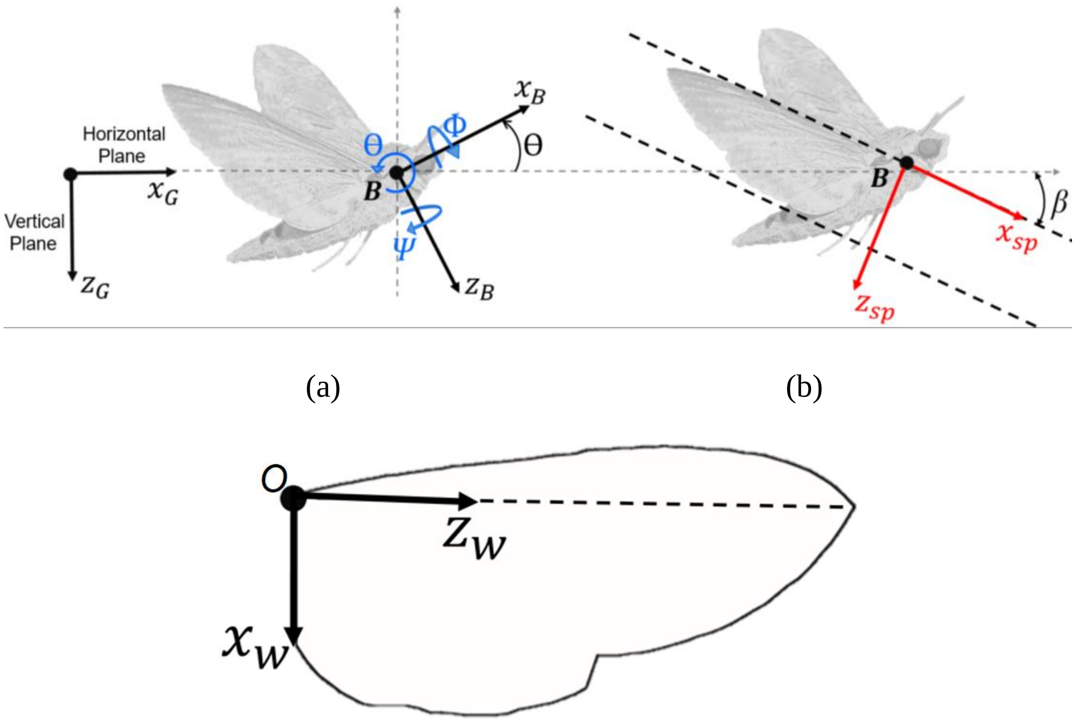

(a) (b)

(c)

Figure 2.1 Wing and body kinematic definitions and coordinate systems

2.2 Wing Kinematics

During the flapping motion, the wing rotates around three axes of the Stroke Plane Frame (X_{sp}, Y_{sp}, Z_{sp}), and these motions can be notated with three angles as the feathering angle (α), the stroke positional angle (γ), and the elevation angle (η). Note that these angles in question are different than the Euler angles. With the change of the feathering angle (α), the wing's pitching motion occurs, while with the change in the stroke positional angle (γ), and the elevation angle (η), the flapping motion occurs. The feathering angle (α) is the angle between the wing surface and the X_{sp} axis as shown in Figure 2.2a. The stroke positional angle (γ) is the angle that occurs with the back and forth motion of the wing and located between the wing and the Y_{sp} axis as shown in Figure 2.2b. The elevation angle (η) is the angle that occurs with the rotation of the wing around the X_{sp} axis as shown in Figure 2.2c.

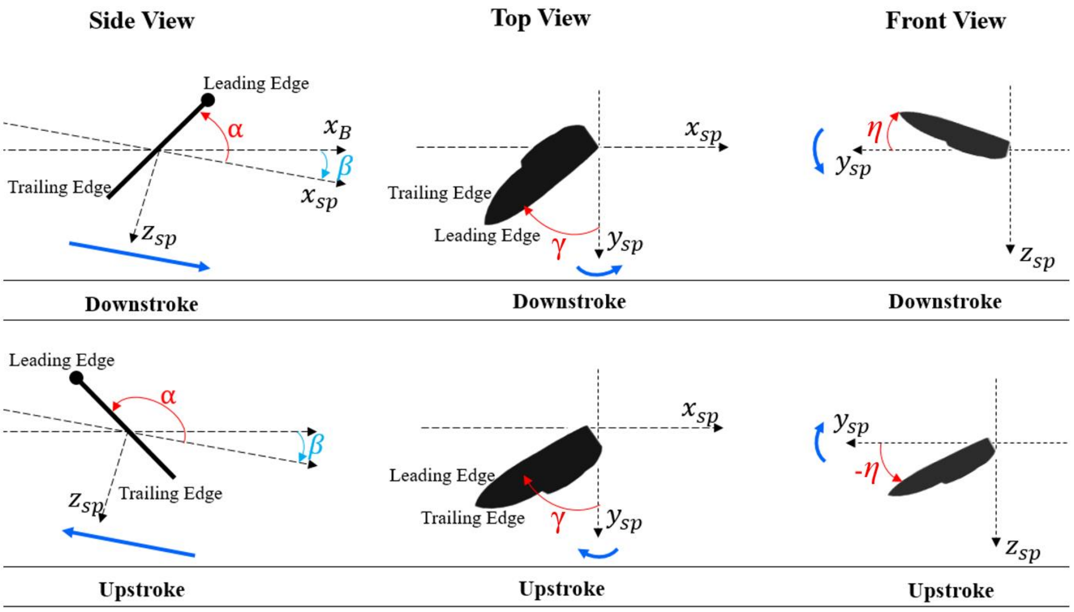

Figure 2.2 Angular definitions of flapping-wing (Dark blue lines represent the instantaneous direction of the movement, red lines represent the instantaneous wing angles)

Note that, the feathering angle (α) is equal to the angle of attack when the flapping-wing MAV is hovering and the air is still which means there is no incoming airflow other than the flow due to the flapping motion. The angle between the X_{sp} and the X_B axis is the stroke plane angle (β). Hawkmoth Manduca sextas actualize minor up and down motions, which are governed by the elevation angle (η) (Willmott & Ellington, 1997). Therefore, in the current study, the elevation angle (η) is set to zero during calculations.

2.3 Modelling 3D Flapping Motion Using Blade Element Theory with Quasi-Steady Estimation

The quasi-steady approach is a method to estimate unsteady aerodynamic forces and moments, by considering the instantaneous wing kinematics (Chin & Lentink, 2016). In other words, during quasi-steady calculations, the instantaneous forces occurred during unsteady motion are calculated as if it is steady motion with the same instantaneous velocity and attitude (Ellington, 1984). Therefore, at quasi-steady assumptions, calculated aerodynamic forces are changing with time, not because of the flow's time dependency but just because of the time dependency of the wing kinematics (Sane, 2003). However, the time course of aerodynamic force generation is adequately estimated when both rotational and translational coefficients are considered in the quasi-steady model (Sane & Dickinson, 2002).

The blade element theory is the technique in which the aerodynamic forces caused by the chordwise flow and acting on a portion of a wing are calculated. The relative velocity of the flow is calculated by summing the related components of the flapping, body, and induced velocities (Smith et al., 1996). The spanwise components of the flow are neglected during calculations. As shown in Figure 2.3 , the portions are selected along the span and located between distances r and $r + dr$ (Ellington, 1984). Total aerodynamic forces produced by the flapping motion can then be calculated by integrating the forces on each strip along the span.

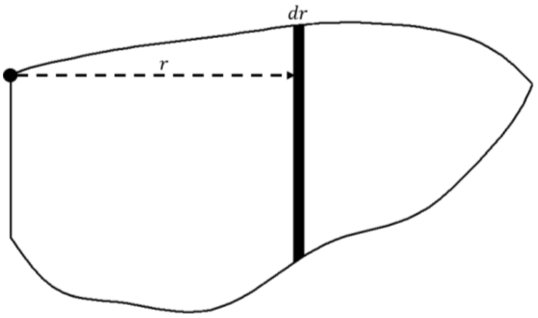

Figure 2.3 Representation of a MS wing model with one of the strips used during calculations with blade element theory

According to Truong et al. (2011), the force coefficients obtained from an unsteady flow should be used to get more realistic results while applying the blade element theory. Otherwise, using force coefficients obtained from a steady environment may cause underestimating the aerodynamic forces.

According to Sane & Dickinson (2002), the components of the instantaneous forces produced by the flapping motion are the translational forces, rotational forces, forces due to the added mass effect, and forces due to the wake capture as represented in Equation 2.1.

$$F_{instantaneous} = F_{translational} + F_{rotational} + F_{wake\ capture} + F_{added\ mass} \quad (2.1)$$

where $F_{instantaneous}$ is the instantaneous forces and the moment on the wing. $F_{translation}$ and $F_{rotation}$, are the forces occurred by the translational and rotational motion of the wing respectively. $F_{wake-capture}$ is the force because of the wake formed during a previous stroke and capture of this wake by the wing during its flapping motion and, $F_{added-mass}$ is the forces due to the added-mass inertia related to translational and rotational accelerations which are acting normal to the wing surface (Sane & Dickinson, 2002).

In the current study, the blade element theory with quasi-steady assumption is used to model 3D flapping motion. The method uses translational and rotational forces in addition to the added mass effect to calculate the instantaneous forces. Wake capture mechanism is not considered in the current study as is done also by Kim et al. (2015). Therefore, to calculate the instantaneous forces on a single strip without considering wake capture effect, Equation 2.1 is modified as shown in Equation 2.2.

$$F_{instantaneous\_i} = F_{translation\_i} + F_{rotation\_i} + F_{added-mass\_i} \quad (2.2)$$

Where subscript i denotes the number of the aerodynamic strip.

The method in the current study does not consider the wing-wing interactions, the wing-body interactions, and the spanwise components of the flow. Calculations are done at each instant of a flapping period by considering the instantanous angular positions, angular velocities, and angular accelerations. As can be expected, the results converge to a final value as the time steps converge to zero seconds. Therefore, the model gives more accurate results as the calculation repetition in a single period increases. Two thousand calculations done at equal intervals in a single period are found to be satisfactory after evaluations.

The wing is separated into equal strips along the span (b) as shown in Figure 2.4, and the lift, the drag and the moment on each aerodynamic strip is calculated.

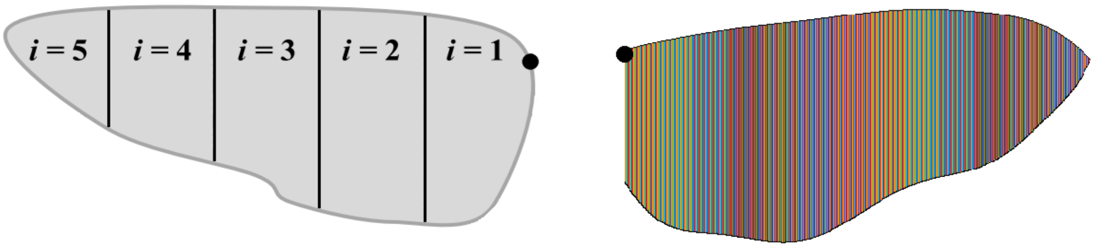

Figure 2.4 Hawkmoth wing models (a) with 5 equal strips (Kim et al 2015) (b) with 700 equal strips (Current Study)

Components of the instantaneous forces at Equation (2.2) for each of the aerodynamic strip are given as Equation (2.3) to (2.5) by Kim et al. (2015).

$$F_{translation} = \begin{bmatrix} L_{T,i} \\ D_{T,i} \\ M_{T,i} \end{bmatrix} = \begin{bmatrix} C_L \frac{\rho}{2} V_i^2 c_i dr \\ C_D \frac{\rho}{2} V_i^2 c_i dr \\ C_M \frac{\rho}{2} V_i^2 c_i^2 dr \end{bmatrix} \tag{2.3}$$

$$F_{rotation} = \begin{bmatrix} L_{R,i} \\ D_{R,i} \\ M_{R,i} \end{bmatrix} = \begin{bmatrix} C_R \rho \dot{\alpha}_i V_i c_i^2 dr \cdot cos\alpha \\ C_R \rho \dot{\alpha}_i V_i c_i^2 dr \cdot sin\alpha \\ C_R \rho \dot{\alpha}_i V_i c_i^2 dr \cdot \varepsilon_i \end{bmatrix} \tag{2.4}$$

$$F_{added-mass} = \begin{bmatrix} L_{A,i} \\ D_{A,i} \\ M_{A,i} \end{bmatrix} = \begin{bmatrix} \frac{\pi}{4} \rho c_i^2 (\ddot{\Phi} R) sin\alpha dr \cdot cos\alpha \\ \frac{\pi}{4} \rho c_i^2 (\ddot{\Phi} R) sin\alpha dr \cdot sin\alpha \\ \frac{\pi}{4} \rho c_i^2 (\ddot{\Phi} R) sin\alpha dr \cdot \varepsilon_i \end{bmatrix} \tag{2.5}$$

L_i represents lift created on each wing strip and acts at -z_{sp} direction. D_i represents drag created on each wing strip and acts at -x_{sp} direction. M_i represents moment created on each wing strip around y_{sp} axis.

Therefore, aerodynamic forces and the moment acting on each aerodynamic strip are obtained by summing translational forces, rotational forces and forces due to added-mass inertia on that strip. After Equations (2.3) to (2.5) are substituted into Equation (2.2), aerodynamic forces acting on one strip is obtained with Equation (2.6).

$$F_{instantaneous,i} = \begin{bmatrix} L_i \\ D_i \\ M_i \end{bmatrix} = \begin{bmatrix} L_{T,i} \\ D_{T,i} \\ M_{T,i} \end{bmatrix} + \begin{bmatrix} L_{R,i} \\ D_{R,i} \\ M_{R,i} \end{bmatrix} + \begin{bmatrix} L_{a,i} \\ D_{a,i} \\ M_{a,i} \end{bmatrix} = \begin{bmatrix} C_{L,i}\frac{\rho}{2}V_i^2 c_i dr \\ C_{D,i}\frac{\rho}{2}V_i^2 c_i dr \\ C_{M,i}\frac{\rho}{2}V_i^2 c_i^2 dr \end{bmatrix} +$$

$$\begin{bmatrix} C_{R,i}\rho\dot{\alpha}_i V_i c_i^2 dr \cdot cos\alpha \\ C_{R,i}\rho\dot{\alpha}_i V_i c_i^2 dr \cdot sin\alpha \\ C_{R,i}\rho\dot{\alpha}_i V_i c_i^2 dr \cdot \varepsilon_i \end{bmatrix} + \begin{bmatrix} \frac{\pi}{4}\rho c_i^2\left(\ddot{\Phi}R\right)sin\alpha dr \cdot cos\alpha \\ \frac{\pi}{4}\rho c_i^2\left(\ddot{\Phi}R\right)sin\alpha dr \cdot sin\alpha \\ \frac{\pi}{4}\rho c_i^2\left(\ddot{\Phi}R\right)sin\alpha dr \cdot \varepsilon_i \end{bmatrix} \tag{2.6}$$

Where, c_i is the chord length of the strip, dr is the strip width, ε_i, is the distance between the half chord line and the wing pitching axis Z_w and acts as a moment arm. The lift coefficient ($C_{L,i}$), drag coefficient ($C_{D,i}$), moment coefficient ($C_{M,i}$) as the functions of effective angle of attack are curve fitted from the experimental results presented by (Han et al., 2015b) and shown in Equations (2.7) to (2.9) $C_{R,i}$ is obtained from (Kim et al., 2015) and shown in Equation (2.10)

$$C_L(\alpha_i) = 0.8456sin(0.02086\alpha_i + 1.265) + 0.8452sin(0.04803\alpha_i - 1.181) + 0.04764sin(0.1169\alpha_i - 1.101) \tag{2.7}$$

$$C_D(\alpha_i) = 2.941sin(0.01935\alpha_i - 0.171) + 0.7002sin(0.06062\alpha_i - 3.867) + 0.1118sin(0.1246\alpha_i - 3.36) \tag{2.8}$$

$$C_M(\alpha_i) = 0.7671sin(0.02421\alpha_i + 2.534) + 0.3185sin(0.0747\alpha_i - 2.009) + 0.1051sin(0.1418\alpha_i - 8.034) + 0.04902sin(0.2054\alpha_i - 7.459) \tag{2.9}$$

$$C_R = \pi\left(0.75 - \frac{x_i}{c_i}\right) \tag{2.10}$$

x_i is the distance of the leading edge from the wing pitching axis Z_w. The effective angle of attack (α_i) of each stip differs from the geometric angle of attack of the wing α(t), that is inputted as one of the wing kinematics. The resultant airflow angle due to the horizontal airflow components $V_{hori,i}$, $V_{u_{sp}}$, $V_{v_{sp}}$, $V_{r_{sp}}$, and the vertical airflow components $V_{vert,i}$, $V_{w_{sp}}$, $V_{p_{sp}}$, $V_{q_{sp}}$ changes the angle of attack for each strip which yields the effective angle of attack α_i.

$$\alpha_i = \alpha(t) + arctan\left(\frac{V_{vert,i}+V_{w_{sp}}+V_{p_{sp}}+V_{q_{sp}}}{V_{hori,i}+V_{u_{sp}}+V_{v_{sp}}+V_{r_{sp}}}\right) \tag{2.11}$$

$$V_i = \sqrt{\left(V_{hori,i} + V_{u_{sp}} + V_{v_{sp}} + V_{r_{sp}}\right)^2 + \left(V_{vert,i} + V_{w_{sp}} + V_{p_{sp}} + V_{q_{sp}}\right)^2} \tag{2.12}$$

V_i, is the total inflow velocity acting on each strip. In addition to the airflow velocity that occurred by the flapping motion, considering the airflow due to the body velocity is necessary to obtain a more realistic solution. Equations (2.13) to (2.20) show the method of calculation of horizontal and vertical airflow components.

$$V_{hori,i} = -R_i\,\dot{\Phi}(t) \tag{2.13}$$

$$V_{u_{sp}} = u_{sp}cos(|\Phi(t)|) \tag{2.14}$$

$$V_{v_{sp}} = v_{sp}sin\big(-\Phi(t)\big) \tag{2.15}$$

$$V_{r_{sp}} = R_i\,r_{sp} \tag{2.16}$$

$$V_{vert,} = R_i\,\dot{\theta}(t) \tag{2.17}$$

$$V_{w_{sp}} = w_{sp}cos(|\theta(t)|) \tag{2.18}$$

$$V_{p_{sp}} = R_i\,p_{sp}cos(\Phi(t)) \tag{2.19}$$

$$V_{q_{sp}} = R_i\,q_{sp}sin(|\Phi(t)|) \tag{2.20}$$

R_i is the distance of each strip from the wing root in the direction of Z_W-axis. u_{sp}, v_{sp}, w_{sp}, p_{sp}, q_{sp} and r_{sp} are the velocity components of the wing at the stroke plane frame that are caused by the components of the body velocity u_b, v_b, w_b, p_b, q_b and r_b. Linear components of the body velocity (u_b, v_b, w_b), and the rotational components of the body velocity (p_b, q_b, r_b) that are defined at the body fixed coordinate frame are transformed to the stroke plane frame. Figure 2.5 illustrates the inflow components in the stroke plane frame.

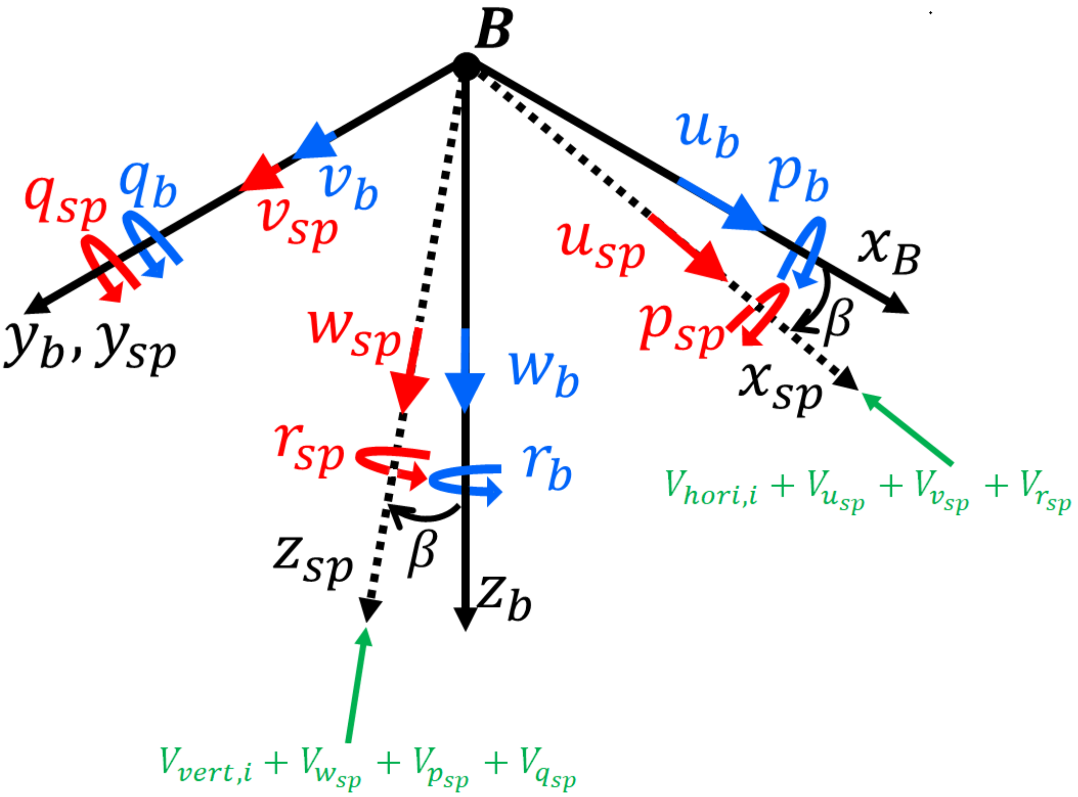

Blue arrows represent the body velocity components in the body-fixed frame; red arrows represent the body velocity components in the stroke plane frame; green arrows represent the horizontal and the vertical inflow velocity components.

Figure 2.5 The transformation of the velocity vectors between two frames (body fixed frame and stroke plane frame)

Transformations of the velocities at the body fixed coordinate frame to the stroke plane frame are realized with the transformation matrices presented in Equations (2.21) and (2.22). Transformation is performed according to Figure 2.5 which is representation of the relation of 2 coordinate frames.

$$\begin{bmatrix} u_{sp} \\ v_{sp} \\ w_{sp} \end{bmatrix} = \begin{bmatrix} \cos(\beta) & 0 & \sin(\beta) \\ 0 & 1 & 0 \\ -\sin(\beta) & 0 & \cos(\beta) \end{bmatrix} \begin{bmatrix} u_b \\ v_b \\ w_b \end{bmatrix} \tag{2.21}$$

$$\begin{bmatrix} p_{sp} \\ q_{sp} \\ r_{sp} \end{bmatrix} = \begin{bmatrix} \cos(\beta) & 0 & \sin(\beta) \\ 0 & 1 & 0 \\ -\sin(\beta) & 0 & \cos(\beta) \end{bmatrix} \begin{bmatrix} p_b \\ q_b \\ r_b \end{bmatrix} \tag{2.22}$$

The wing kinematics used in the current study are given at Equations (2.23) to (2.29). Equation (2.24) and (2.25) are the first and second derivatives of Equation (2.23), respectively. Equation (2.27) is the derivative of Equation (2.26), which is zero in this study since the elevation angle (η) is not changing. Equation (2.29) is the derivative of Equation (2.28) and gives the rate of change of the feathering angle (α) with time.

$$\gamma(t) = \gamma_{amp} \sin(2\pi f t) + \bar{\gamma} \tag{2.23}$$

$$\dot{\gamma}(t) = \gamma_{amp} \cdot \left(\frac{\pi}{180}\right)(2\pi f) \cos(2\pi f t) \tag{2.24}$$

$$\ddot{\gamma}(t) = -\gamma_{amp} \cdot (\pi/180)(2\pi f)^2 \cdot sin(2\pi f t) \tag{2.25}$$

$$\eta(t) = \eta_{amp} \sin(2\pi f t) + \bar{\eta} \tag{2.26}$$

$$\dot{\eta}(t) = \eta_{amp} \cdot \left(\frac{\pi}{180}\right)(2\pi f) cos(2\pi f t) \tag{2.27}$$

$$\alpha(t) = \frac{\alpha_{amp}}{\tanh(C_\alpha)} \cdot \tanh(C_\alpha \cdot \sin(2\pi f t + \psi_\alpha)) + \bar{\alpha} \tag{2.28}$$

$$\dot{\alpha}(t) = \frac{\alpha_{amp}}{\tanh(C_\alpha)} \cdot (\pi/180)(2\pi f) \cdot [1 - (\tanh(C_\alpha \cdot \sin(2\pi f t + \psi_\alpha)))^2] \cdot (C_\alpha \cdot \cos(2\pi f t + \psi_\alpha)) \tag{2.29}$$

Hawkmoths flaps their wings with a frequency between 24.5 Hz and 26.5 Hz, and most of the time, they keep this frequency (Willmott & Ellington, 1997). In order to support the weight of a Hawkmoth the flapping frequency during hovering is chosen to be 26.1 Hz. Other system inputs used for the dynamic stability analyses in the current study are given in Table 2.1.

Table 2.1 Parameters values used to create wing kinematics similar to a Hawkmoth's flapping motion

Parameters	**Values**
$\alpha_0(°)$	90
$\alpha_{amp}(°)$	45
$\gamma_0(°)$	0
$\gamma_{amp}(°)$	-55.4
$\eta_0(°)$	0
$\eta_{amp}(°)$	0
$f(Hz)$	26.1
C_α	4.5

α_0 and α_{amp} are the mean and the amplitude values of the feathering angle (α), respectively, which means the wing rotates around an angle α_0 up to $\alpha_0 + \alpha_{amp}$ at the upstroke and down to $\alpha_0 - \alpha_{amp}$ at the downstroke as illustrated in Figure 2.6a. Similarly, γ_0 and γ_{amp} are the mean and the amplitude values for the stroke positional angle (γ), respectively, while η_0 and η_{amp} are the mean and the amplitude values for the elevation angle (η), respectively. The wing kinematics are also represented in Figure 2.6.

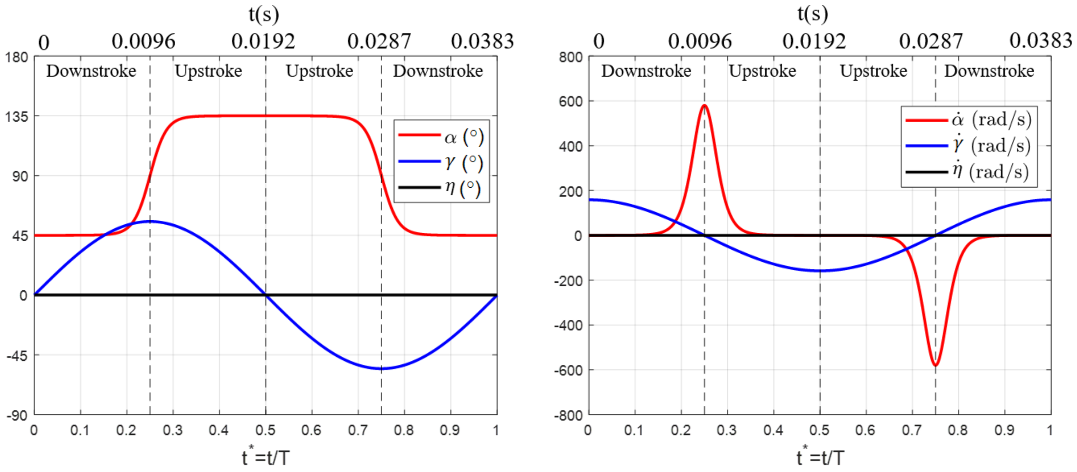

Figure 2.6 (a) Angular positions of the wing for one flapping period (b) Angular velocities of the wing for one flapping period

2.3.1 Wing Geometry

Aerodynamic forces that are created with the flapping motion vary according to the geometric features of the wings. A simplified model of the Hawkmoth wing used by Usherwood & Ellington (2002) is modelled in the current study. They regarded the forewing and underwing of a hawkmoth Manduca sexta shown in Figure 2.7a as a joint, single wing as shown in Figure 2.7b.

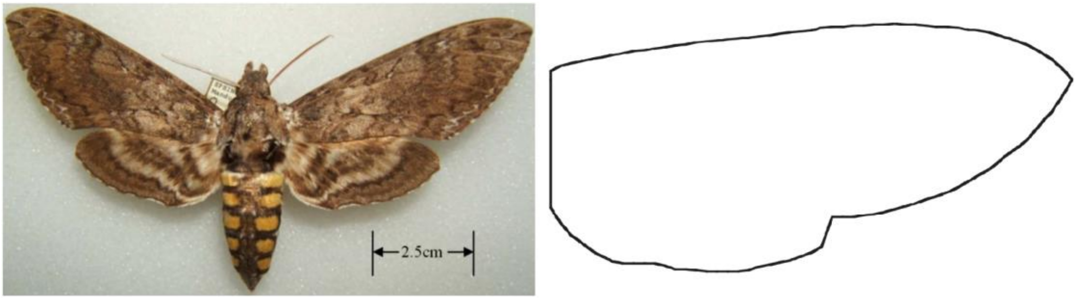

(a) (b)

Figure 2.7 (a) A Female hawkmoth Manduca sexta (Hanrahan, 2006) (b) Simplified Manduca sexta wing model (Usherwood & Ellington, 2002)

As shown in Figure 2.8, the wing shape is introduced to the model by two functions, one creating the leading edge and the other creating the trailing edge. The functions used to create the wing shape are given in Equations (2.30) and (2.31).

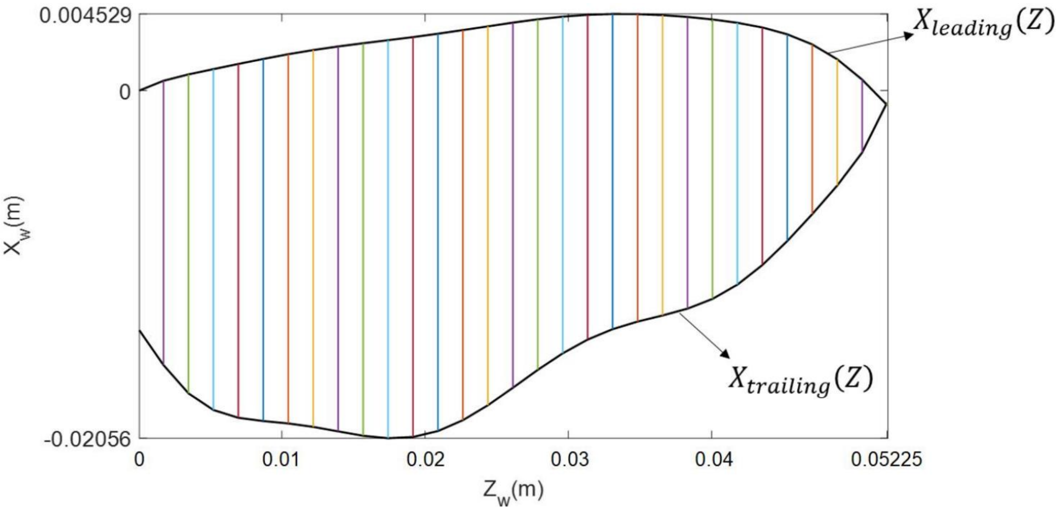

Figure 2.8 Wing model with 30 equal strips along the span (b)

$$X_{leading} = -1.246 \cdot 10^9 \cdot z^8 - 7.249 \cdot 10^7 \cdot z^7 + 3.105 \cdot 10^7 \cdot z^6 - 2.271 \cdot 10^6 \cdot z^5 + 6.48 \cdot 10^4 \cdot z^4 - 553.4 \cdot z^3 - 7.91 \cdot z^2 + 0.295 \cdot z + 2.033 \cdot 10^{-5} \qquad (2.30)$$

$$X_{trailing} = 5.783 \cdot 10^{10} \cdot z^8 - 1.567 \cdot 10^{10} \cdot z^7 + 1.698 \cdot 10^9 \cdot z^6 - 9.458 \cdot 10^7 \cdot z^5 + 2.895 \cdot 10^6 \cdot z^4 - 4.857 \cdot 10^4 \cdot z^3 + 440.7 \cdot z^2 - 2.238 \cdot z - 0.01382 \qquad (2.31)$$

Insects and birds flying at low Reynolds numbers have significantly small wing thickness, and effects of the wing thickness at low Reynolds number flight are investigated by Kurtulus (2016). The wing thickness is assumed to be infinitesimal small during calculations, so the wing's mass is neglected. Since the The wing is assumed to be solid, so no flection effect or cambered structure is considered. More lift can be obtained when the wing camber, elasticity, and vein structure is considered (Bektas, 2020).

Geometric parameters of the hawkmoth wing models used in different studies are given in Table 2.2.

Table 2.2 Geometric parameters for different MS wing models

Parameters **Wing Models**	$b\ (m)$	$\bar{c}\ (m)$	**Area** (m^2)	**Aspect Ratio**
Hawkmoth Manduca sexta (Mao & Gand, 2003)	0.0519	0.01826	0.0009478	5.68
Hawkmoth Manduca sexta (Kim & Han, 2014)	0.0483	0.01809	0.00088375	5.34
Simplified Hawkmoth MS Model (Usherwood & Ellington, 2002)	0.05225	0.01846	0.00096469	5.66
Current Study at 2D flight control	0.05225	0.01816	0.0009491	5.75
Current Study at 3D flight control (2.75x Scale Up Model)	0.14369	0.05132	0.00073739	5.75

2.3.2 Validation Cases

The aerodynamic model is validated with the 3D pure plunge motion and the 3D flapping motion. The studies that use the Manduca sexta wing are preferred as the validation cases. The validation results are presented in the following sections.

2.3.2.1 3D Pure Plunge Validation Cases

The 3D pure plunging cases used for validation are obtained from Bektas et al. (2019). They used computational fluid dynamics (CFD) to solve the Navier-stokes equations with a simplified hawkmoth Manduca sexta wing identical to the represented one shown in Figure 2.7b.

The number of mesh that Bektas et al. (2019) used is 2020648 with a time step (Δt) of 0.0001s and the mesh domain and the boundary layers are represented in Figure 2.9.

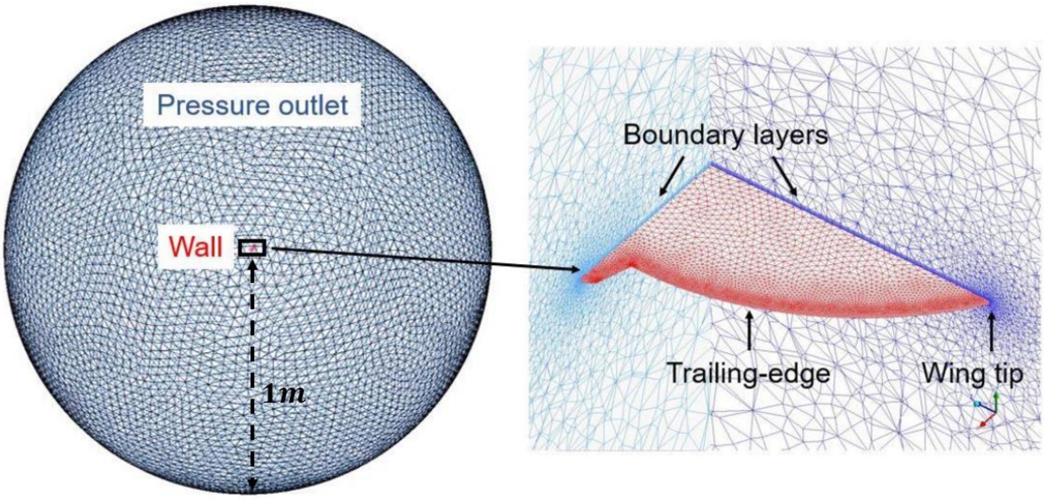

Figure 2.9 (a) Boundary conditions for CFD Analysis in hover (pressure outlet=Blue, wall=red) (b) zoomed in view of the mesh structure and the boundary layers around the wing (Bektas et al. 2019)

In the study, the equations solved are laminar, incompressible, unsteady and 3D Navier-Stokes equations.

The aerodynamic model is tested with two different cases for the pure plunging motion which are Case 2 and Case 6 of (Bektas et al., 2019). The kinematic parameters of the cases are presented in Table 2.3.

Table 2.3 Wing kinematics used for the validation cases. Case 1 and Case 2 in the current study are equivalent to Case 2 and Case 6 of (Bektas et al. 2019)

Case Number	$\alpha_0(°)$	$\alpha_{amp}(°)$	$\gamma_0(°)$	$\gamma_{amp}(°)$	$\eta_0(°)$	$\eta_{amp}(°)$	$f(s^{-1})$	$\beta(°)$
1	90	0	0	60.7	0	0	26.1	15
2	90	0	0	60.7	0	0	26.3	90

The position of the wing at some instants of downstroke are illustrated in Figure 2.10.

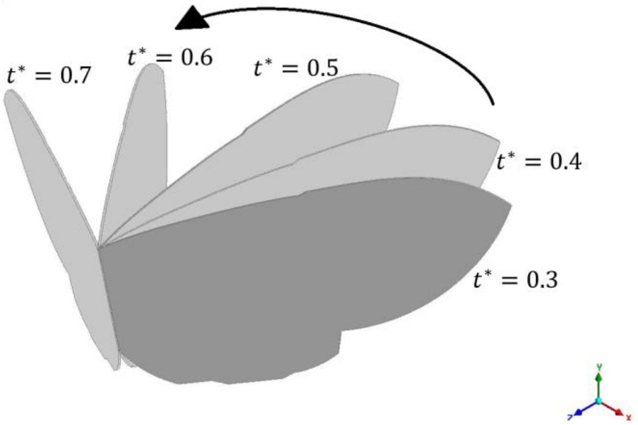

Black arrow represents the direction of motion during downstroke

Figure 2.10 Illustration of the wing positions of the hovering Manduca Sexta obtained from Bektas, M (2020) both for validation case 1 and case 2.

Since the validation cases in this section are pure plunge motions, the angle of attacks, which are the same as the feathering angle (α) for the cases, are kept constant at 90° during the flapping motion. The wing kinematics that refer to Case 1 are shown in Figure 2.11.

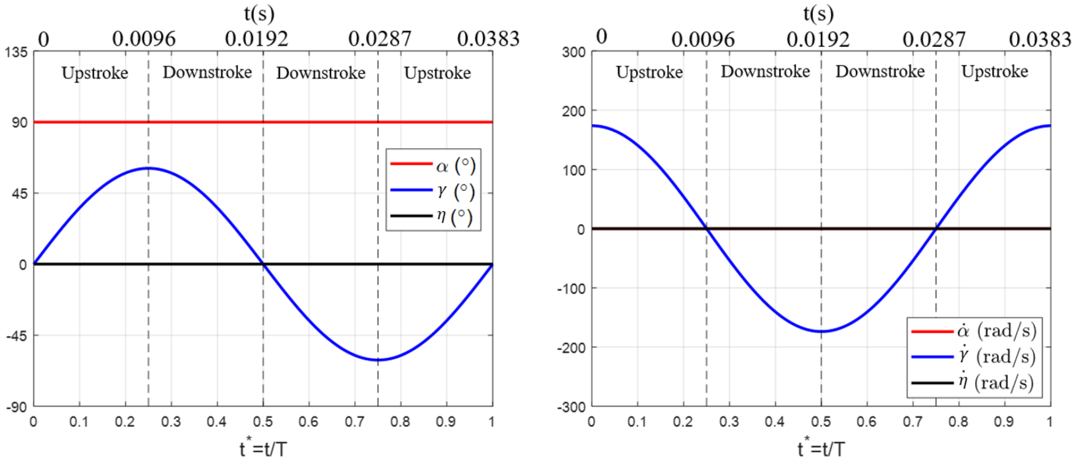

(a) (b)

Figure 2.11 Wing kinematics for the pure-plunge motion, validation case 1

The dimensionless vertical and horizontal forces obtained for Case 1 are compared in Figure 2.12.

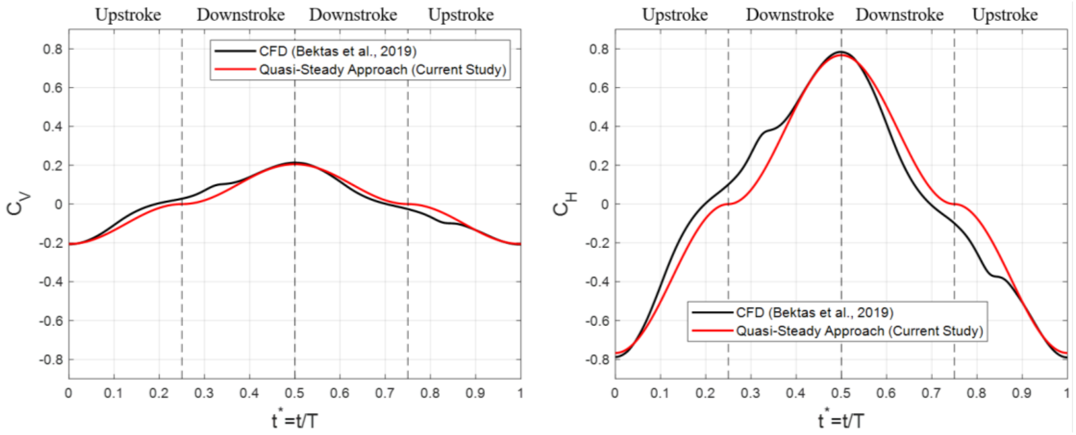

(a) (b)

Figure 2.12 Comparison of the CFD and the aerodynamic model for Manduca Sexta wing (Case 1) (a) C_V (b) C_H

The error between the results of the two methods is given in Figure 2.13 for Case 1. The error is observed to be maximum at 0.318T and 0.818T, which are shortly after the stroke reversals. Meanwhile, it is observed to be minimum at 0T and 0.5T, which are the middle of the upstroke and downstroke, respectively.

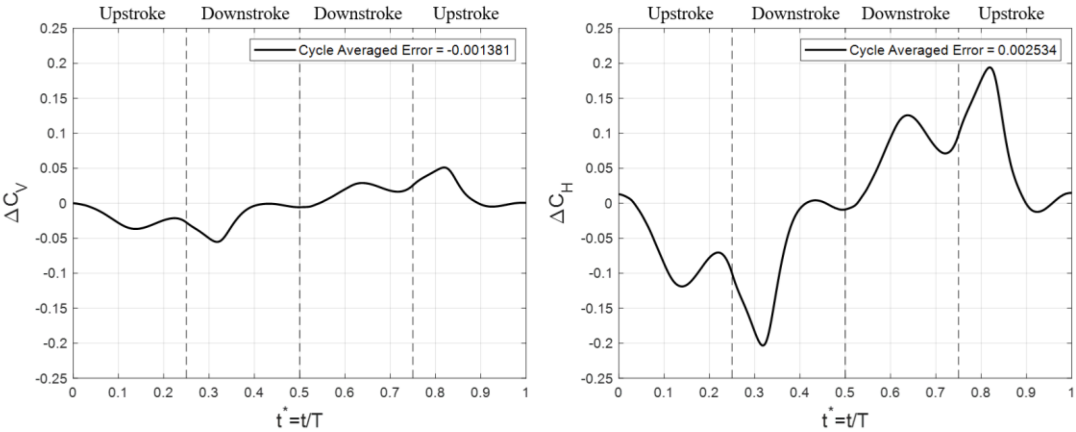

(a) (b)

Figure 2.13 The difference between the CFD and the aerodynamic model for Manduca Sexta wing (Case 1) (a) C_V error (b) C_H error

The dimensionless Z-vorticity contours for the instants where the error is maximum and the error is minimum are obtained from the study Bektas, M. (2020) conducted and given in Figure 2.14 for Case 1.

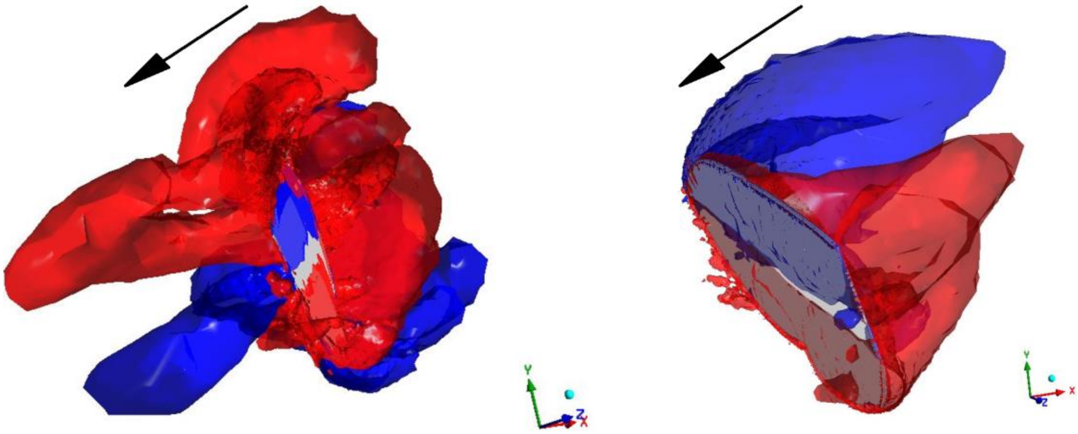

(a) (b)

Black arrows represent the direction of motion

Figure 2.14 Dimensionless Z-vorticity contours at the instant where (a) the error is maximum $t^* = \mathrm{t/T} = 0.31$ (b) the error is minumum $t^* = \mathrm{t/T} = 0.5$ for the validation case 1

The wing kinematics that refer to Case 2 are represented in Figure 2.15.

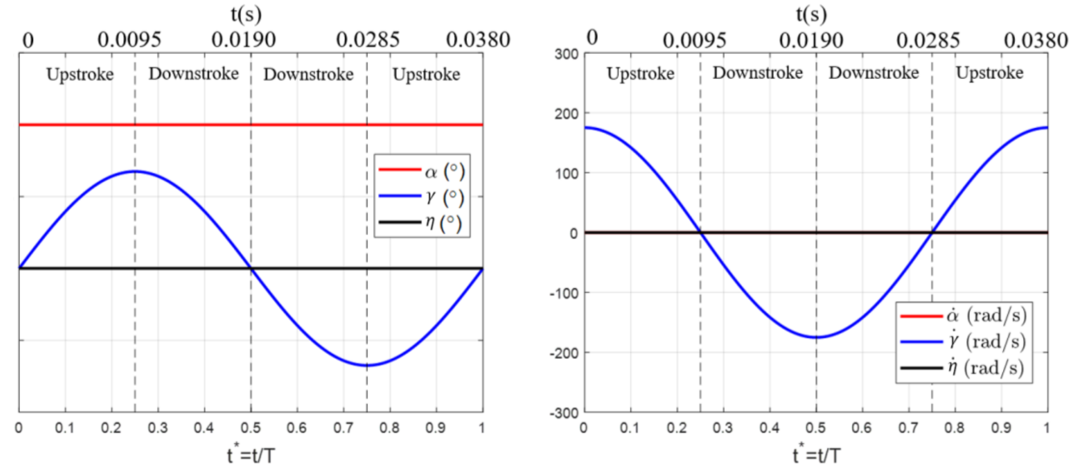

(a) (b)

Figure 2.15 Wing kinematics for the pure-plunge motion, validation case 2

The dimensionless vertical and horizontal forces obtained for Case 2 are compared in Figure 2.16.

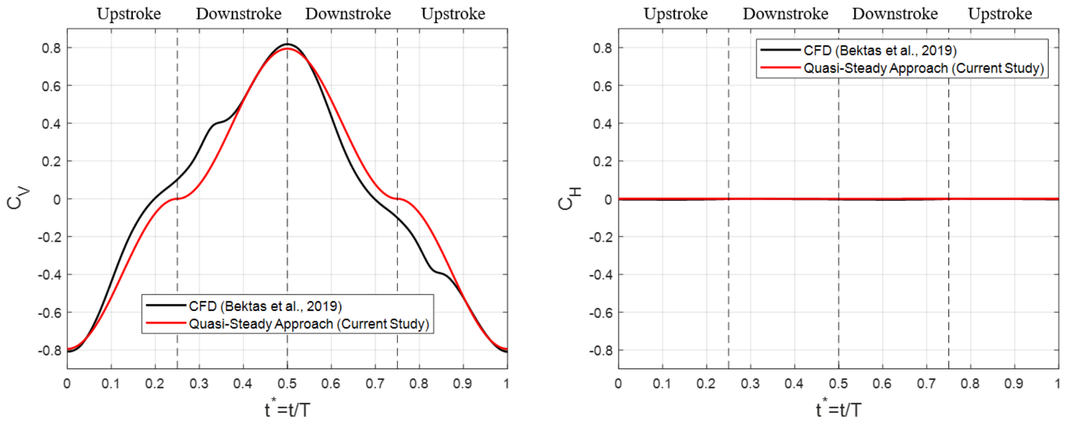

(a) (b)

Figure 2.16 Comparison of the CFD and the aerodynamic model for Manduca Sexta wing (Case 2) (a) C_V (b) C_H

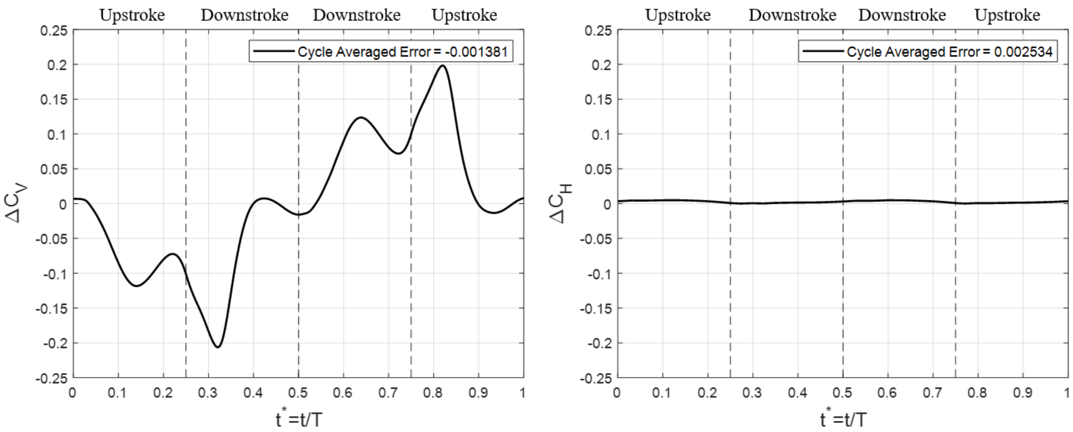

(a) (b)

Figure 2.17 The difference between the CFD and the aerodynamic model for Manduca Sexta wing (Case 2) (a) C_V error (b) C_H error

The dimensionless Z-vorticity contours for the instants where the error is maximum and the error is minimum are obtained from the study Bektas, M. (2020) conducted and given in Figure 2.18 for Case 2.

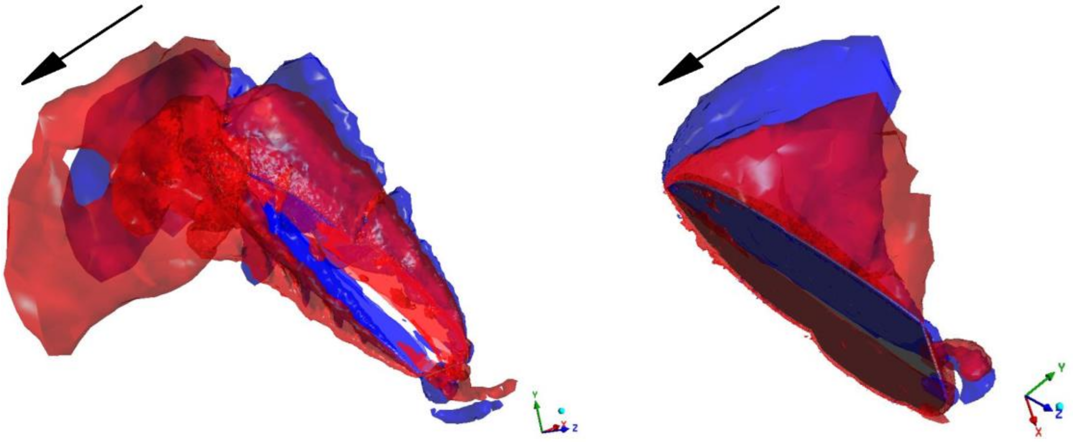

(a) (b)

Black arrows represent the direction of motion

Figure 2.18 Dimensionless Z-vorticity contours at the instant where (a) the error is maximum $t^* = \mathrm{t/T} = 0.31$ (b) the error is minumum $t^* = \mathrm{t/T} = 0.5$ for the validation case 2

As a result of the comparisons, it is determined that the aerodynamic model obtained with the quasi-steady approach calculates the forces obtained by the pure plunge motion with high accuracy. The major differences occurred at 0.31T, and 0.81T might be caused by the unsteady effects since they are not captured by the quasi-steady approach.

CFD solutions obtained by Bektas, M. (2020) are investigated to clarify the effects that cause the differences between the two solutions. Figure 2.14 and Figure 2.18 show that the vorticities are more dominant in the regions close to the wingtip. In addition, clockwise vorticities (blue) are observed around the leading edge, whereas counter clockwise vorticities (red) are observed around the trailing edge. However, the main reason for the failure of the current quasi-steady model in predicting the forces at the beginning of the downstroke ($t^* = 0.31$) is the complicated and dominant vorticities resulting from the previous stroke, as shown in Figure 2.14a and Figure 2.18a. Since these vortex traces disappear through the middle of the stroke ($t^* = 0.5$), as shown in Figure 2.14b and Figure 2.18b, the results of the two methods converge to each other.

The difference between the results of the aerodynamic model and the CFD analysis is even less when cycle averaged values are compared. The model underestimated the aerodynamic forces at around 0.31T but overestimated at around 0.81T, compensating each other when the averaged values are used. As a result, if the average values are used, the aerodynamic model created within the scope of the study is sufficient to model the pure plunge flapping motion.

Moreover, for both pure-plunge cases, with the CFD calculations, it took 26 hours and 10 minutes for ANSYS/Fluent to calculate the aerodynamic forces with a 2 CPU 16 core Intel Xeon Z640 workstation computer (Bektas et al., 2019). However, with the aerodynamic model created in the current study, it lasted 12 seconds to calculate the aerodynamic forces created with a flapping motion.

2.3.2.2 3D Flapping (pitch/plunge) Motion Validation Case

The 3D flapping motion case used for validation is presented by (Han et al., 2015a). They used an experimental setup and a scaled-up hawkmoth wing model with a span (b) of 0.25 meters and an aspect ratio (AR) of 3.09. They used an additional length of 0.025 meters at the wing root to place the sensor, increasing the span to 0.0275 meters. The experiment is operated at Reynolds number of 7400, which is similar to a real hawkmoth wing Reynolds number in hover.

Reynolds number (Re) is a paremeter which gives the ratio of the inertial forces to the viscosity forces and given in Equation (2.32).

$$Re = \frac{\rho_f U_\infty \bar{c}}{\mu} \tag{2.32}$$

where,

$$\bar{c} = \frac{AR}{b} = \frac{3.09}{0.025} = 0.08091\ m \tag{2.33}$$

where, ρ_f, U_∞, $\bar{c}$, μ are the density of the fluid, velocity of the fluid, mean aerodynamic chord and the dynamic viscosity of the fluid respectively.

The wing kinematics that refer to the flapping motion validation case are shown in Figure 2.19.

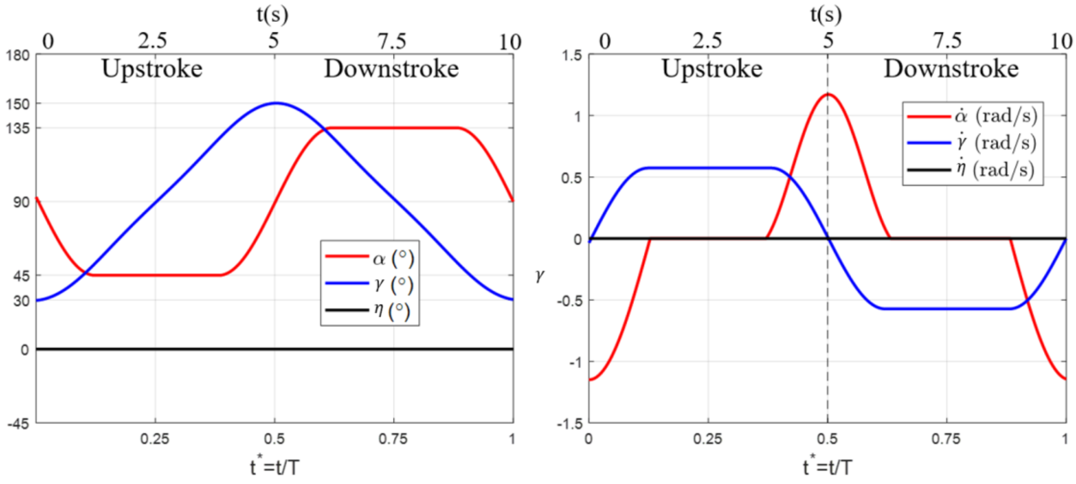

(a) (b)

Figure 2.19 Wing kinematics for the flapping motion validation case

The dimensionless lift and drag forces obtained for flapping motion validation case are compared in Figure 2.20.

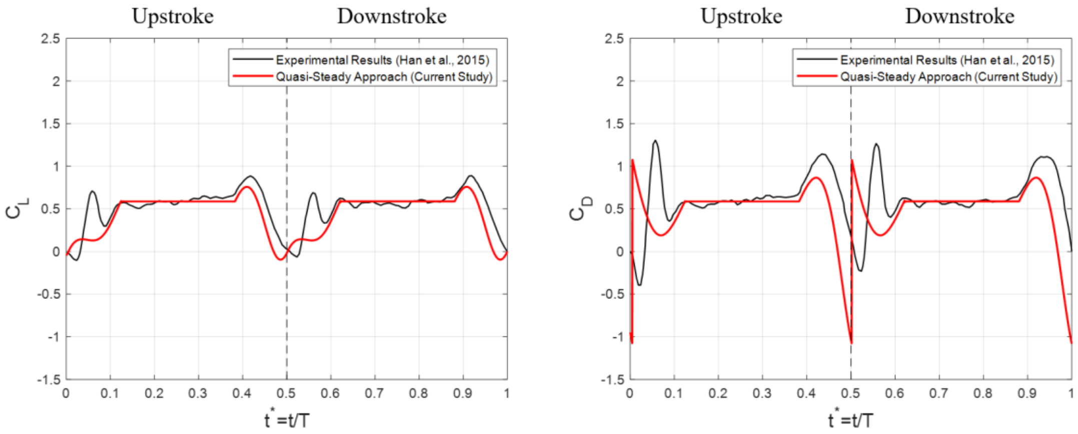

(a) (b)

Figure 2.20 Comparison of the experimental results and the aerodynamic model results (a) C_L (b) C_D

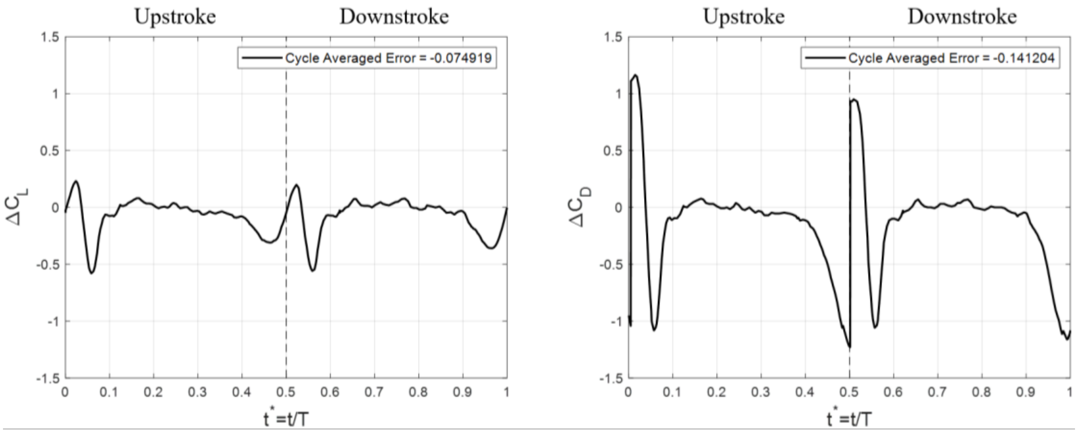

(a) (b)

Figure 2.21 The difference between the experimental results and the aerodynamic model results (a) C_L error (b) C_D error

As seen in Figure 2.20, the aerodynamic forces obtained during one period with the model are compared with the experimental data. The magnitude of the forces resulting from the translational movement of the wing is estimated with high accuracy. Although the time and the direction of peaks arising during the wing rotation are predicted correctly in 0.462T and 0.962T, the magnitudes of the peaks are underestimated with the model. The peaks that occur at 0.058T and 0.558T could not be spotted with the aerodynamic model at all. The reason is that these peaks result from unsteady effects such as wake traces from previous strokes (wake capture) that cannot be modelled with a quasi-steady approach. Besides, the previous stroke causes an induced velocity region that changes the distribution of the downwash velocity of the wing (Kurtulus, 2005). Therefore, to estimate the aerodynamic forces of a 3D flapping motion more accurately, one must take these unsteady effects into account.

The aerodynamic model based on the quasi-steady estimations and blade element theory successfully estimated aerodynamic forces created by the 3D pure plunge motion only with minor errors. The model becomes even more reliable during the cycle-averaging evaluations since the error vanishes when the total forces are computed. When it comes to calculating the aerodynamic forces that occurred from the 3D flapping motion, the model is still utilizable in cycle-averaging applications like the current study. However, for real-time applications, a more sophisticated, unsteady effect-considering method must be used.

CHAPTER 3

DYNAMICAL MODELLING AND CONTROL

Firstly, dynamical modelling of a flapping-wing MAV system including the modelling of the rigid body dynamics, actuator dynamics and inertia calculations are given in this section. Later, different linear control strategies and their applications are shown for 2D and 3D models.

The frequently changing aerodynamic loads are forcing the relatively slow body dynamics to oscillate, but the flapping frequencies of the insects are too large compared to their natural frequencies. Hence, the body is not affected by the oscillatory changes but can only answer the mean values of the aerodynamic forces (Taha et al., 2020). This is a fact that makes the usage of a cycle averaging technique for aerodynamic force and moment calculation proper during the control simulations of a flapping-wing MAV. On the other hand, one should note that the vibration has a natural stabilization effect on bodies, and according to Taha et al. (2020), natural hoverers such as insects and hummingbirds utilize this vibration effect to stabilize their body. Therefore, since the vibration effect is not considered with the averaging technique, the mathematical model of the body dynamics might show up more unstable than the actual body dynamics. This study uses the averaging method to calculate aerodynamic forces, and the flapping-wing MAV body is considered a rigid body. Therefore, the aforementioned passive stabilization mechanism that insects might utilize is neglected.

3.1 Dynamical Modelling of the Flapping-wing MAV

In this section 2D and 3D models developed in this study are given.

3.1.1 Moment of Inertia Calculations

This section gives the moment of inertia calculations and the assumptions done.

3.1.1.1 Wing Moment of Inertia

Previously, it was stated that the wing thickness is neglected. This condition was valid for the aerodynamic force and moment calculations. However, to calculate inertia, the wing needs to have mass, so needs to have thickness. Therefore, only for inertia calculations the wing is assumed to have thickness which is 0.3 mm. Note that the wing thickness was neglected at the aerodynamic force calculations.

The approximate moments of inertia of a single wing are calculated according to the Equations (3.1) to (3.3).

$$J_{w_{xx}} = \int (y^2 + z^2) dm = \int \left(\left(\frac{t_w}{2} \right)^2 + R(i)^2 \right) m(i) \tag{3.1}$$

$$J_{w_{yy}} = \int (x^2 + z^2) dm = \int (\Delta c(i)^2 + R(i)^2) m(i) \tag{3.2}$$

$$J_{w_{zz}} = \int (x^2 + y^2) dm = \int \left(\Delta c(i)^2 + \left(\frac{t_w}{2} \right)^2 \right) m(i) \tag{3.3}$$

where, t_w is the wing thickness, $R(i)$ is the distance of the i^{th} strip from the wing base in z_w-axis direction. Δc is the distance of the center of the relevant strip from the x_w-axis. $m(i)$ is the mass of the i^{th} strip. A 2.75x scaled up wing model that is presented in Table 2.2 is used for 6-DOF dynamical modelling and control studies. The calculated moments of inertia of the wing are given in Table 3.1.

Table 3.1 Predicted wing inertia values

$J_{w_{xx}}\ (kg\ m^2)$	$J_{w_{yy}}\ (kg\ m^2)$	$J_{w_{zz}}\ (kg\ m^2)$
0.000026562	0.000028466	0.0000019049

3.1.1.2 Body Moment of Inertia

The moment of inertia calculations are done by taking into account some actuator and sensor models' weights that are likely to be used.

Table 3.2 Predicted inertia values for the wing and the body

	Wing	**Body**
$J_{xx}\ (kg\ m^2)$	0.000026562	0.00024758
$J_{yy}\ (kg\ m^2)$	0.000028466	0.00024758
$J_{zz}\ (kg\ m^2)$	0.0000019049	0.00024758

As shown in Table 3.2, the body is assumed to be symmetrical around three axes, so the moment of inertias are assumed to be identical. During control simulations, the only difference in inertias occur due to the wing inertias, which are calculated in Section 3.1.1.1.

3.1.2 6-DOF Modelling of a Flapping-wing MAV

Equations for the trimmed flight are obtained using Flat Earth, Body-Axes 6 degree of freedom equations from Etkin, (2005) and adapted for the study as shown below. The translational dynamics are given in Equations (3.4) to (3.6).

$$\dot{u} = rv - qw - gsin(\Theta) + \frac{F_{ae_x}}{m} \tag{3.4}$$

$$\dot{v} = -ru + pw + gsin(\Phi)cos(\Theta) + \frac{F_{ae_y}}{m} \tag{3.5}$$

$$\dot{w} = qu - pv + gcos(\Phi)cos(\Theta) + \frac{F_{ae_z}}{m} \tag{3.6}$$

The rotational dynamics are given in Equations (3.7) to (3.9).

$$M_x = J_{xx}\dot{p} - J_{xz}(\dot{r} + pq) - (J_{yy} - J_{zz})qr - J_{yz}(q^2 - r^2) - J_{xy}(\dot{q} - rp) \tag{3.7}$$

$$M_y = J_{yy}\dot{q} - J_{xz}(r^2 - p^2) - (J_{zz} - J_{xx})rp - J_{xy}(\dot{p} - qr) - J_{yz}(\dot{r} - pq) \tag{3.8}$$

$$M_z = J_{xx}\dot{r} - J_{xz}(\dot{p} + qr) - (J_{xx} - J_{yy})pq - J_{xy}(p^2 - q^2) - J_{yz}(\dot{q} - rp) \tag{3.9}$$

It is desired to obtain the system dynamics for hovering condition. The roll angle is assumed as 0^o during hover ($\Phi = 0^o$). At this phase, the flapping-wing MAV is assumed as symmetric in all three directions. Therefore, the products of inertia are neglected $\left(J_{xz} = J_{yz} = J_{xy} = 0\right)$. After the aformentioned values are substituted into Equations (3.4) to (3.9), 6-DOF rigid body dynamics equations valid for hovering case are obtained as Equations (3.10) to (3.15).

$$\dot{u} = rv - qw - gsin(\Theta) + \frac{F_{ae_x}}{m} \tag{3.10}$$

$$\dot{v} = -ru + pw + \frac{F_{ae_y}}{m} \tag{3.11}$$

$$\dot{w} = qu - pv + gcos(\Theta) + \frac{F_{ae_z}}{m} \tag{3.12}$$

$$\dot{p} = \frac{M_x}{J_{xx}} + \left(J_{yy} - J_{zz}\right)\frac{qr}{J_{xx}} \tag{3.13}$$

$$\dot{q} = \frac{M_y}{J_{yy}} + (J_{zz} - J_{xx})\frac{rp}{J_{yy}} \tag{3.14}$$

$$\dot{r} = \frac{M_z}{J_{zz}} + \left(J_{xx} - J_{yy}\right)\frac{pq}{J_{zz}} \tag{3.15}$$

The system model that is reduced to 3DOF is presented in Section 3.1.3.

3.1.3 3DOF Modelling of a Flapping-wing MAV

In this section, modelling of the 3DOF longitudinal flight dynamics of a hovering flapping-wing MAV are given.

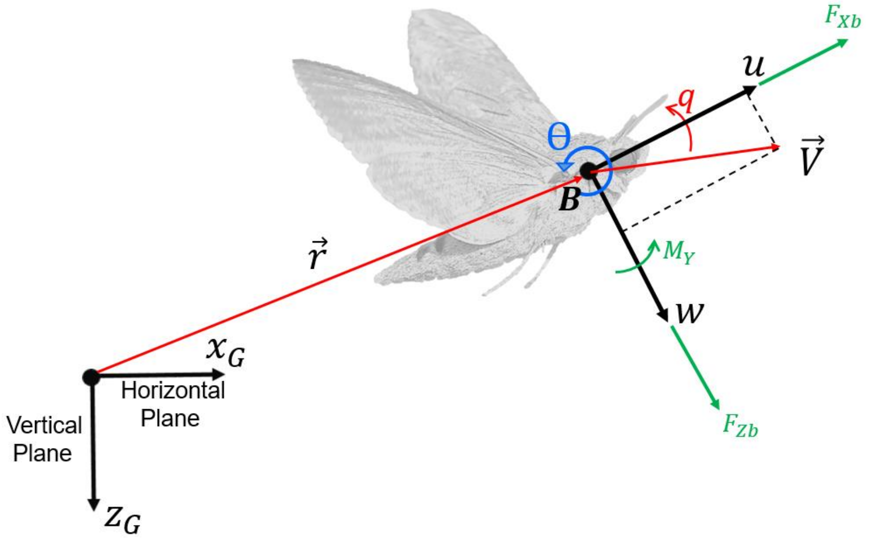

Figure 3.1 Illustration of the 2D Body Dynamics

$$\dot{x}_B = u\cos\theta + w\sin\theta \tag{3.16}$$

$$\dot{z}_B = -u\sin\theta + w\cos\theta \tag{3.17}$$

The aerodynamic forces and moments are included in F_{x_b}, F_{z_b} and M_y. The LTI model is obtained for hovering flight. In this section, 2D flight of a flapping-wing MAV is studied and the velocity components are obtained as Equation (3.18).

$$\vec{V} = \dot{x}_B\vec{\imath} + \dot{z}_B\vec{k} = u\vec{\imath} + w\vec{k} \tag{3.18}$$

To obtain the acceleration components of the body, derivative of Equation is obtained.

$$\dot{\vec{V}} = \dot{u}\vec{\imath} + u\dot{\vec{\imath}} + \dot{w}\vec{k} + w\dot{\vec{k}} \tag{3.19}$$

$$\dot{\vec{V}} = \dot{u}\vec{\imath} - uq\vec{k} + \dot{w}\vec{k} + wq\vec{\imath} \tag{3.20}$$

From the Equation (3.20), the acceleration of the body in the horizontal plane $\left(a_{x_B}\right)$, and the acceleration of the body in the vertical blane are obtained as given in Equations (3.21) and (3.22).

$$a_{x_B} = \dot{u} + qw \tag{3.21}$$

$$a_{z_B} = \dot{w} - qu \tag{3.22}$$

Since the total forces acting on the body in the horizontal plane are the mass times the acceleration of the body at the same plane, $\dot{u}$ is obtained as shown below.

$$\sum F_{x_B} = ma_{x_B} \tag{3.23}$$

$$F_{x_B} = F_{ae_x} - mgsin(\theta) \tag{3.24}$$

$$a_{x_B} = \frac{F_{ae_x}}{m} - gsin(\theta) \tag{3.25}$$

When Eqution (3.21) is substituted into Equation (3.25), Equation (3.26) is obtained.

$$\dot{u} = -gsin(\theta) - qw + \frac{F_{ae_x}}{m} \tag{3.26}$$

Since the total forces acting on the body in the vertical plane are the mass times the acceleration of the body at the same plane, $\dot{w}$ is obtained as shown below.

$$\sum F_{z_B} = ma_{z_B} \tag{3.27}$$

$$F_{z_B} = F_{ae_z} + mgcos(\theta) \tag{3.28}$$

$$a_{z_B} = \frac{F_{ae_z}}{m} + gcos(\theta) \tag{3.29}$$

By substituting Equation (3.22) into Equation (3.29), Equation (3.30) is obtained.

$$\dot{w} = gcos(\theta) + qu + \frac{F_{ae_z}}{m} \tag{3.30}$$

Total moment acting to the point B which is the center of gravity of the body $\left(M_{y_B}\right)$ is equal to the moment of inertia times the rotational acceleration of the body $(\dot{q})$.

$$\sum M_{y_B} = J_Y \dot{q} \tag{3.31}$$

$$\dot{q} = \frac{M_{y_B}}{J_Y} \tag{3.32}$$

Using Equations (3.16), (3.17), (3.26), (3.30) and (3.32), the state equations are obtained as shown in Equations (3.33) to (3.38).

$$\dot{x}_1 = \dot{x}_B = \mathrm{ucos\theta} + \mathrm{wsin\theta} \tag{3.33}$$

$$\dot{x}_2 = \dot{u} = -gsin\theta - qw + \frac{F_{ae_x}}{m} \tag{3.34}$$

$$\dot{x}_3 = z_B = -\mathrm{usin\theta} + \mathrm{wcos\theta} \tag{3.35}$$

$$\dot{x}_4 = \dot{w} = gcos\theta + qu + \frac{F_{ae_z}}{m} \tag{3.36}$$

$$\dot{x}_5 = \dot{\theta} = q \tag{3.37}$$

$$\dot{x}_6 = \dot{q} = \frac{M_{Y_B}}{J_Y} \tag{3.38}$$

where, the state variables are $x = [x_B \ u \ z_B \ w \ \theta \ q]^T$, and $\frac{F_{ae_x}}{m} = \hat{F}_{XB}, \frac{F_{ae_z}}{m} = \hat{F}_{ZB}, \frac{M_{Y_B}}{J_Y} = \hat{M}_{YB}$. The six state variables are the distance of the body from the initial position in the horizontal plane (x_B), the velocity of the body in the horizontal plane (u), the distance of the body from the initial position in the vertical plane (z_B), the velocity of the body in the vertical plane (w), the body picth angle (θ), and the rate of change in the body pitch angle (q). The system matrix A is obtained by the Jacobian Matrix method. The system matrix A and the mean aerodynamic stability derivatives are shown in Equation (3.39).

$$A = \begin{bmatrix} 0 & \cos(\theta) & 0 & \sin(\theta) & 0 & 0 \\ 0 & \partial\hat{F}_{XB}/\partial \mathrm{u} & 0 & \partial\hat{F}_{XB}/\partial \mathrm{w} & \partial\hat{F}_{XB}/\partial \theta - gcos\theta & \partial\hat{F}_{XB}/\partial \mathrm{q} \\ 0 & -\sin(\theta) & 0 & \cos(\theta) & 0 & 0 \\ 0 & \partial\hat{F}_{ZB}/\partial \mathrm{u} & 0 & \partial\hat{F}_{ZB}/\partial \mathrm{w} & \partial\hat{F}_{ZB}/\partial \theta - gsin\theta & \partial\hat{F}_{ZB}/\partial \mathrm{q} \\ 0 & 0 & 0 & 0 & 0 & 1 \\ 0 & \partial\hat{M}_{YB}/\partial \mathrm{u} & 0 & \partial\hat{M}_{YB}/\partial \mathrm{w} & \partial\hat{M}_{YB}/\partial \theta & \partial\hat{M}_{YB}/\partial \mathrm{q} \end{bmatrix} \tag{3.39}$$

The aerodynamic model presented in Section 2 is used by getting linearized around the trim condition. Small perturbations are applied to the state variables, and the slope of the changes in the mean aerodynamic forces are used as the stability derivatives in Equation (3.39). After the values of the stability derivatives are substituted into Equation (3.39), the system matrix A is obtained as Equation (3.40).

$$\mathrm{A} = \begin{bmatrix} 0 & 0.7683 & 0 & 0.6401 & 0 & 0 \\ 0 & -1.953 & 0 & 0.7775 & -5.9245 & -0.0533 \\ 0 & -0.6401 & 0 & 0.7683 & 0 & 0 \\ 0 & -2.3930 & 0 & 0.9613 & -6.5739 & -0.0621 \\ 0 & 0 & 0 & 0 & 0 & 1 \\ 0 & 65.6034 & 0 & -29.0895 & 0 & 1.4521 \end{bmatrix} \tag{3.40}$$

The hovering flapping-wing MAV system has its eigenvalues in Equation (3.41), which means the system is unstable.

$$\lambda = [0 \;\; 0 \;\; -5.6594 \;\; 3.0615 \pm 5.0513i \;\; -0.0032] \tag{3.41}$$

The hovering flapping-wing MAV system has an unstable oscillatory mode resulting from the complex-conjugate eigenvalue pair ($3.0615 \pm 5.0513i$) located at the positive side of the real part and two stable non-oscillatory modes resulting from the eigenvalues that are located at the negative side of the real axis ($-5.6594, -0.0032$).

3.1.4 Modelling of Actuator Dynamics

Four brushless direct current (BLDC) servo motors and two BLDC motors are needed to manipulate three controls for each wing mechanism. On the other hand, a UAV needs to weigh less than 100 grams to be classified as a MAV. Therefore, satisfying the weight constraints is a difficult challenge in the development process of a MAV.

In the current study, mathematical models of the actuator dynamics are included in the controller design to put the controller to a more realistic test. However, at this stage, the weights of the actuators are ignored.

The motor's inductance is very small and has no significant effect compared to resistance when applying Kirchhoff's law, so; it can be neglected as it is done by Bouabdallah (2007). By neglecting the inductance, the second order motor transfer function can be reduced to first order.

To maniputale the flapping frequency, a Portescap 16ECS36 Ultra EC Slotless BLDC mathematical model is used. The first order motor transfer function obtained from Nise, N S., (2020) is used to model the actuator dynamics and given in Equation (3.42), where the output is the angular velocity in (rad/s), and the input is the applied voltage in (V).

$$\frac{\Omega_m(s)}{E_a(s)} = \frac{\frac{K_t}{R_i J_t}}{s+\frac{1}{J_t}\left(D_m+\frac{K_t K_e}{R_i}\right)} \tag{3.42}$$

where,

K_t: Motor Torque Constant in $\frac{N\,m}{A}$

K_e: Back EMF Constant in $\frac{V}{rad/s}$

R_i: Internal Resistance in Ω

J_t: Total inertia ($rotor\ inertia + wing\ inertia$) in $kg\ m^2$

D_m: Motor viscous friction constant in $N\ m\ s$

After the values given in Table are substituted into Equation , the first order transfer function of the Portescap 16ECS36 Ultra EC Slotless BLDC is obtained as presented in Equation (3.43).

$$G(s) = \frac{\Omega_m(s)}{E_a(s)} = \frac{131.89}{0.0032s+1} \tag{3.43}$$

Table 3.3 Motor Specifications

Data / Model	K_t	K_e	R_i	J_t	D_m
Portescap 16ECS36 Ultra EC Slotless BLDC	0.0035	0.00373	0.65	$1.3116 * 10^{-7}$	$2.0761 * 10^{-5}$
Faulhaber BLDC-servomotors 1645 BHS	0.0039	0.00391	0.684	$5.9 * 10^{-8}$	$2.2692 * 10^{-5}$
Faulhaber BLDC-servomotors 1645 BHS	0.0039	0.00391	0.684	$5.9 * 10^{-8}$	$2.2692 * 10^{-5}$

To manipulate the mean feathering angle ($\bar{\alpha}$) and the mean stroke positional angle ($\bar{\gamma}$) Faulhaber BLDC-servomotors 1645 BHS are used. The mathematical models of the servomotors are obtained as from Equation , given by Nise (2020) where the output is the angular position in (rad), and the input is the applied voltage in (V).

$$\frac{\alpha_0(s)}{E_a(s)} = \frac{\gamma_0(s)}{E_a(s)} = \frac{\frac{K_t}{R_i J_t}}{s^2 + \frac{1}{J_t}\left(D_m + \frac{K_t K_e}{R_i}\right)s} \tag{3.44}$$

After the values in Table are substituted into Equation (3.44), the transfer functions for the motors to manipulate the mean feathering angle ($\bar{\alpha}$) and the mean stroke positional angle ($\bar{\gamma}$) are obtained as given in Equations (3.45) and (3.46), respectively.

$$G(s) = \frac{\alpha_0(s)}{E_a(s)} = \frac{126.75}{0.0014s^2+s} \tag{3.45}$$

$$G(s) = \frac{\gamma_0(s)}{E_a(s)} = \frac{126.75}{0.0029s^2+s} \tag{3.46}$$

3.2 Control of the Flapping-Wing MAV

As a result of the comprehensive literature research that focuses on the controls that insects use during the maneuver, and preferred controls for flapping-wing MAV maneuvers, a summary for possible controls to be used to control a flapping-wing MAV is achieved as shown in Figure 3.2.

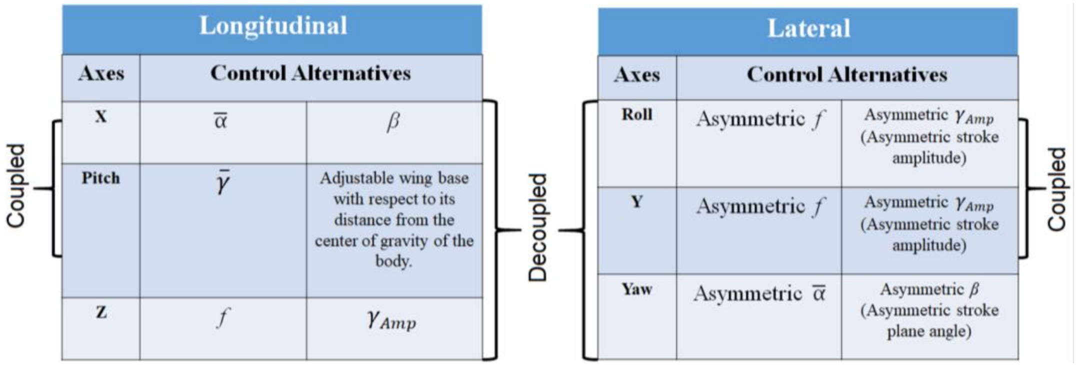

Longitudinal		
Axes	Control Alternatives	
X	$\bar{\alpha}$	β
Pitch	$\bar{\gamma}$	Adjustable wing base with respect to its distance from the center of gravity of the body.
Z	f	γ_{Amp}

Lateral		
Axes	Control Alternatives	
Roll	Asymmetric f	Asymmetric γ_{Amp} (Asymmetric stroke amplitude)
Y	Asymmetric f	Asymmetric γ_{Amp} (Asymmetric stroke amplitude)
Yaw	Asymmetric $\bar{\alpha}$	Asymmetric β (Asymmetric stroke plane angle)

Figure 3.2 Possible controls to be utilized to control the flight of a flapping-wing MAV.

In the subsequent sections, some of the control alternatives shown in Figure 3.2 are used to control the flapping-wing MAV model.

The control studies are conducted in two phases. 3DOF insect flight is controlled in the first phase by considering the actual Hawkmoth Manduca Sexta body/wing morphology. However, actualizing the flight of approximately 1.4 grams of a vehicle is not possible in today's technology when the weights of the actuators, sensors, power supply, and essential mechanisms are considered. Therefore, 6-DOF flight control is studied in the second phase by considering more realistic flapping-wing MAV weight and inertia values. The morphological values of the flapping-wing MAVs that are used in the simulations are given in Table .

Table 3.4 Morphological parameters of the flapping-wing MAV for different cases

	Mass (g)	I_{xx} **(kg·m^2)**	I_{yy} **(kg·m^2)**	I_{zz} **(kg·m^2)**
Longitudinal Dynamics Control	1.456	-	$266.7 \cdot 10^{-9}$	-
3D Flight Control	83.4	0.00027414	0.00027605	0.00025138

3.2.1 Control of the Longitudinal Dynamics

In this section, the longitudinal dynamics of the flapping-wing MAV modelled in Section 3.1.3 are controller with different control techniques: the LQR control and the coefficient diagram method.

The control matrix B is achieved by getting the derivatives of the six state equations with respect to two control inputs. The control inputs are determined as the stroke plane angle (*β*) and the flapping frequency (*f*). The control matrix B with the control derivatives is presented in Equation (3.47).

$$B = \begin{bmatrix} 0 & 0 \\ \partial\delta\hat{F}_{XB}/\partial\delta\beta & \partial\delta\hat{F}_{XB}/\partial\delta f \\ 0 & 0 \\ \partial\delta\hat{F}_{ZB}/\partial\delta\beta & \partial\delta\hat{F}_{ZB}/\partial\delta f \\ 0 & 0 \\ \partial\delta\hat{M}_{YB}/\partial\delta\beta & \partial\delta\hat{M}_{YB}/\partial\delta f \end{bmatrix} \tag{3.47}$$

Using the aerodynamic model presented in Section 2, mean aerodynamic forces and their responses to the changes in the control inputs are calculated. Therefore, small perturbations are given to the control inputs, and slopes of the changes are used as the control derivatives. After the control derivatives are substituted, the control matrix B becomes, as shown in Equation (3.48).

$$B = \begin{bmatrix} 0 & 0 \\ -8.5368 & 0.2858 \\ 0 & 0 \\ -4.9804 & -0.7915 \\ 0 & 0 \\ 0 & 1.7947 \end{bmatrix} \tag{3.48}$$

The state-space representation of the system is given in Equations (3.49) and (3.50), which is a general form of state-space representation.

$$\dot{x} = Ax + Bu \tag{3.49}$$

$$y = Cx + Du \tag{3.50}$$

For the current study, the output matrix C is assumed to be six by six identity since all the system states are assumed to be measured. The feedforward matrix D is taken as 0. A controller architecture shown in Figure 3.3. is designed, and the methods used to calculate inner and outer loop gains are given in the following sections.

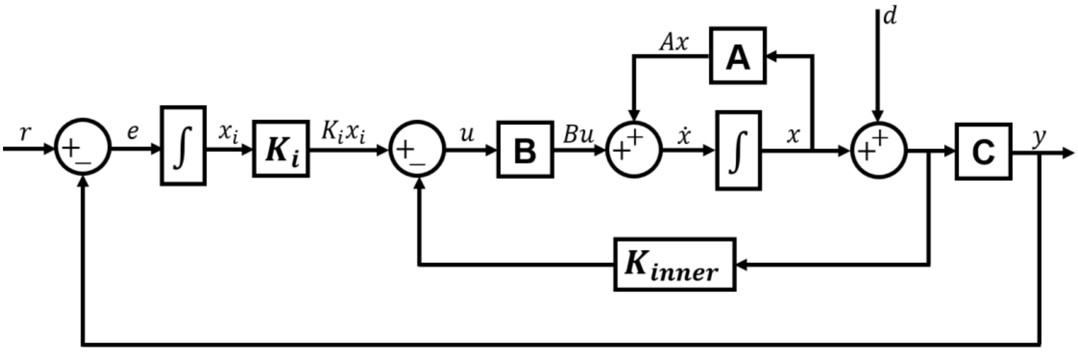

Figure 3.3 Block diagram representation of the LTI System with inner loop and outer loop controllers

Two integral trackers in order to track inputs for two position states, x_B ,and z_B, are added to the system, which augments the system matrix A to eight-by-eight matrix and the control matrix B to eight-by-two matrix. The augmented matrices $A_{Augmented}$ and $B_{Augmented}$ are shown in Equations (3.51) and (3.52), and used during the gain calculation phases.

$$A_{Augmented} = \begin{bmatrix} A & [0] \\ -C & [0] \end{bmatrix} \tag{3.51}$$

$$B_{Augmented} = \begin{bmatrix} B \\ [0] \end{bmatrix} \tag{3.52}$$

3.2.1.1 LQR Controller

Linear Quadratic Regulator (LQR) is a full-state feedback control method in which the optimal control solution is sought for a Linear Time-Invariant (LTI) system. It is a modern control technique and widely used in different types of UAV applications. Based on the users' priorities, i.e., whether the system's performance or the energy used by the actuators is essential, the optimal gain is calculated to stabilize the LTI system.

In the current study, an LQR is one of the controllers that are used. In order to find the optimal gain, the cost function given in Equation (3.53) was minimized by iteratively changing the values of Q and R matrices. The weight matrices were obtained manually after dozens of trials.

$$J = \frac{1}{2}\int_0^{\infty}(x_B^T Q x_B + u_b^T R u_b)dt \tag{3.53}$$

In order to minimize Equation (3.53) the state weight matrix Q and the control weight matrix R were chosen as shown in Equations (3.54) and (3.55).

$$Q = \begin{bmatrix} 10 & 0 & 0 & 0 & 0 & 0 \\ 0 & 1 & 0 & 0 & 0 & 0 \\ 0 & 0 & 100 & 0 & 0 & 0 \\ 0 & 0 & 0 & 1 & 0 & 0 \\ 0 & 0 & 0 & 0 & 10 & 0 \\ 0 & 0 & 0 & 0 & 0 & 1 \end{bmatrix} \tag{3.54}$$

$$R = \begin{bmatrix} 0.001 & 0 \\ 0 & 0.001 \end{bmatrix} \tag{3.55}$$

To obtain a solution for S, the Ricatti Equation presented in Equation (3.56) is solved using the weight matrices given in Equations (3.54) and (3.55).

$$A^T S + SA - SBR^{-1}B^T S + Q = 0 \tag{3.56}$$

and using S, the controller gain is calculated with Equation (3.57).

$$K = R^{-1}B^T S \tag{3.57}$$

After solving the Ricatti Equation, the gain matrix for the augmented system is obtained as shown in Equation (3.58).

$$K = \begin{bmatrix} 1000889 & 270346 & -1715075 & 47348 & 341549 & -14096 & 470439 & -2129049 \\ 55256.86 & 13980.9 & -82911.99 & 2653.4 & -20177.9 & -1908.1 & 41532.6 & -87133.12 \end{bmatrix} \tag{3.58}$$

The values of columns one to six are used as the state feedback gain (inner loop gain) that is employed to stabilize the system, and the 7th and 8th column values are used as the integral gain (outer loop gain), which is used to track position commands.

The inner loop controller gain (K_{inner}) and the Integral Tracker Gain (K_i) are calculated as presented in Equations (3.59) and (3.60) respectively.

$$K_{inner} = \begin{bmatrix} 1000889 & 270346 & -1715075 & 47348 & 341549 & -14096 \\ 55256.86 & 13980.9 & -82911.99 & 2653.4 & -20177.9 & -1908.1 \end{bmatrix} \tag{3.59}$$

$$K_i = \begin{bmatrix} 470439 & -2129049 \\ 41532.6 & -87133.12 \end{bmatrix} \tag{3.60}$$

3.2.1.2 Coefficient Diagram Method

In the control theory, the Coefficient Diagram Method (CDM) is an algebraic approach, which is said to be in the middle of the classical control and the modern control (Manabe, 1998). With the CDM, the desired characteristic equation is easily obtained by specifying the system's time response and solving simple algebraic equations (Kim & Manabe, 2001).

The same control architecture presented in Figure 3.3 is used in this section, but the controller gains are calculated with the Coefficient Diagram Method.

The target characteristic polynomial is obtained from Equation (3.61).

$$P_m(s) = \prod_{j=1}^{n-1} \chi_{n-j}^{j} / \tau^n \left[\left\{ \sum_{i=2}^{n} \left(\prod_{j=1}^{i-1} \frac{1}{\chi_{i-j}^{j}} \right) (\tau s)^i \right\} + \tau s + 1 \right] \qquad (3.61)$$

From Equation (3.61), the desired characteristic equation in the form of Equation (3.62), is obtained.

$$P_m(s) = s^n + a_{n-1}s^{n-1} + \cdots + a_1 s + a_0 \qquad (3.62)$$

When the stability index is taken as suggested by Kara (2014), as given in Equations (3.63) and (3.64), the desired characteristic equation is obtained as presented in Equation (3.65). Calculations are made for the time constant $\tau = 1.6$.

$$\chi_2 = \chi_3 = \chi_4 = \chi_5 = \chi_7 = \chi_7 = 2 \qquad (3.63)$$

$$\chi_1 = 2.5 \qquad (3.64)$$

$$P_m(s) = 0.0000001s^8 + 0.00001s^7 + 0.0005s^6 + 0.0125s^5 + 0.15625s^4 + 0.97654s^3 + 3.05168s^2 + 4.76826s + 2.98016 \qquad (3.65)$$

The gain matrix is calculated with the aim of placing the eigenvalues of the augmented system given in Equations (3.51) and (3.52) to the locations of the characteristic equations' roots. The gain matrix is obtained as shown in Equation (3.66).

$$K = \begin{bmatrix} 233.70 & 5.5 & -536 & -17.4 & -63 & -12 & 312.5 & -655.6 \\ -1275.8 & -22.5 & 2545.8 & 56.8 & 314.3 & 62.7 & -1667 & 3027 \end{bmatrix} \qquad (3.66)$$

The first six columns of the gain matrix is used as the state feedback gain (inner loop gain), which is employed to stabilize the system, and the last 2 columns are used as the integral gain (outer loop gain), which is utilized to track the reference position inputs. The gain matrices for the inner loop controller (K_{inner}), and the outer loop controller (K_i) are presented in Equations (3.67) and (3.68).

$$K_{inner} = \begin{bmatrix} 233.70 & 5.5 & -536 & -17.4 & -63 & -12 \\ -1275.8 & -22.5 & 2545.8 & 56.8 & 314.3 & 62.7 \end{bmatrix} \tag{3.67}$$

$$K_i = \begin{bmatrix} 312.5 & -655.6 \\ -1667 & 3027 \end{bmatrix} \tag{3.68}$$

3.2.2 Controlling the 3D Flight

In the 6-DOF control section, the actuators dynamics and the nonlinear wing model are considered in the simulations. The control system and the dynamics of the 3D flapping flight are shown in Figure 3.4.

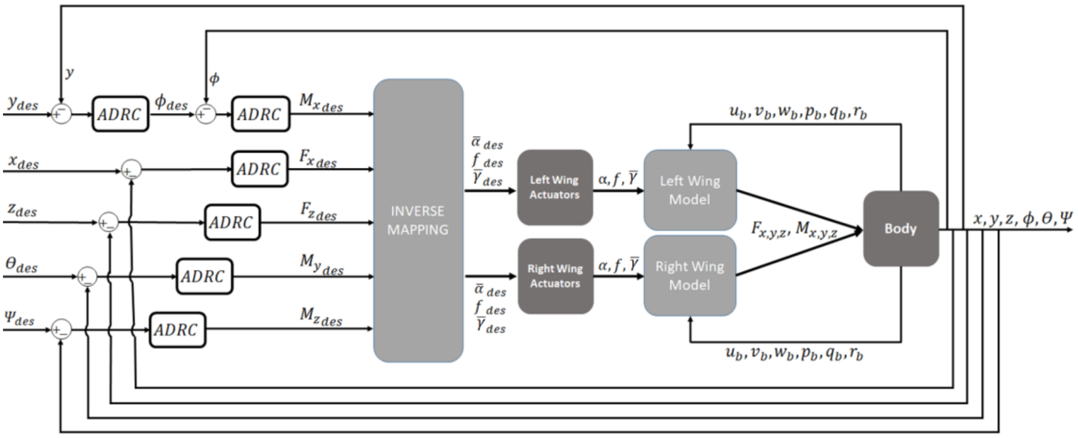

Figure 3.4 Control system demonstration for the 3D flight

In Figure 3.4, α_{des} and f_{des} for the left and the right wings are calculated as given in Equations (3.69) to (3.72).

$$\alpha_{des_l} = \bar{\alpha} + \Delta\bar{\alpha} \tag{3.69}$$

$$\alpha_{des_r} = \bar{\alpha} - \Delta\bar{\alpha} \tag{3.70}$$

$$f_{des_l} = \bar{f} + \Delta\bar{f} \tag{3.71}$$

$$f_{des_r} = \bar{f} - \Delta\bar{f} \tag{3.72}$$

By changing the value of $\Delta\bar{\alpha}$ and $\Delta\bar{f}$, asymmetric forces are produced, and consequently, yaw and roll moments are created, respectively.

The flapping-wing MAV is an underactuated system, and in any of the cases, there is no actuation directly in the direction of y. Therefore, an underactuated controller design is needed to be able to control the system in three directions. A relation between the created force in the y_b-axis and the created vertical force can be considered as given in Equation (3.73).

$$m\ddot{y} = -f_z \cos(\theta)\, sin(-\Phi) \tag{3.73}$$

Assuming $\theta \approx 0$ around hovering condition Equation (3.73) can be rearranged as Equation (3.74).

$$\Phi_{des} = \sin^{-1}\left(\frac{m\ddot{y}}{f_z}\right) \tag{3.74}$$

Calculation of the actuator transfer functions were given in Section 3.1.4.

3.2.2.1 PID Controller

Even if PID is an old control method, it is widely used in the industry because of its simplicity and reliability. PID controller is an error eliminating linear controller, and the term PID comes from Proportional-Integral-Derivative. The output data obtained by sensors or observers are feedbacked to the system continuously and subtracted from the reference input, which gives the error. This type of controller can be also implemented as Proportional (P) Controller, Proportional-Derivative (PD) Controller, and Proportional-Integral (PI) Controller according to the application needs. If a ‘P’ controller is preferred, the error is multiplied with a number which is called Proportional Gain (K_P) and the control signal is fed to the plant. The higher the gain is set, the higher the control signal is, which yields a faster convergence. The function of the integral component is to reduce the steady-state error. Even if the convergence is complete, there might still be a difference between the reference input and the output, which is called the steady-state error. The ‘I’ component integrates the steady-state error, which gives a higher value than the error and multiplies this value with Integral Gain (K_I). Therefore, the controller reads a high error even if the steady-state error is small until the error is reduced to 0. The ‘D’ component is employed to reduce the overshoot by decreasing the control signal. The derivative of the error is multiplied with Derivative Gain (K_D). The general equations of a PID controller structure in the time domain and in the frequency domain are given in Equations (3.75) and (3.76) respectively, where u is the controller signal and e is the error signal.

$$u(t) = K_P\, e(t) + K_I \int e(t)dt + K_D \frac{de(t)}{dt} \tag{3.75}$$

$$u(s) = K_P e(s) + \frac{K_I}{s} e(s) + K_D s e(s) \tag{3.76}$$

3.2.2.2 Linear Active Disturbance Rejection Controller (LADRC)

During the flight of a flapping-wing MAV, there are unpredictable effects such as external disturbances, and nonlinearities that are not modelled. To perform a flight, the system must be controlled by dealing with these uncertainties. In this study, a robust controller that compensates the disturbances and provides a smooth flight is worked on. Proposed by Han (2009), ADRC is a disturbance-rejecting control method that treats the internal uncertainties, the external disturbances and the coupling effects on a nonlinear system together as total disturbances (Suhail et al., 2019). This way, the complexity of the implementation of nonlinear controllers to the system disappears (Gao, 2006). Another advantage of the ADRC is that the controller bandwidth (ω_c) and the observer bandwidth (ω_o) are the only two parameters to deal with which are highly effective on the closed-loop system performance (Tan & Fu, 2015).

ADRC consists of a Tracking Differentiator (TD), a Proportional-Derivative (PD) controller, and an Extended State Observer (ESO). The Tracking Differentiator is used to smooth the reference input (r) and outputs it together with its differential signal as the extended reference signal ($\hat{r}$) (Tan & Fu, 2015; Zhu et al., 2019)

In control engineering, an observer is used to obtaining data that are not measurable or are costly to measure. In some applications, in order to decrease the cost or the system's weight, the number of sensors that are being used is kept low deliberately. In addition, sensor outputs can be found to be insufficient to rely on. Therefore, observers are used to estimating variables instead of sensors or together with sensors (Radke & Gao, 2006).

An Extended State Observer was first proposed by Han (1995). Different than other observers, an ESO estimates a system's un-modelled or incorrectly modelled dynamics, as well as total disturbances. Therefore, an ESO is the foremost component of an ADRC.

Consider a dynamical system, espressed as in Equations (3.77) to (3.79).

$$\dot{x}_1 = x_2 \tag{3.77}$$

$$\dot{x}_2 = f(x_1, x_2, w(t), t) + bu \tag{3.78}$$

$$y = x_1 \tag{3.79}$$

In this problem, x_1 is the state which is desired to be controlled. The term $f\big(x_1, x_2, w(t)\big)$ can be treated as the total disturbance which must be dealt with by manipulating u, so u needs to be manipulated such that $y = x_1$ follows the reference input. Total disturbances are given in the extended state of the observer which is z_3 for a second order ADRC.

$$u = \frac{u_0 - z_3}{b_0} \tag{3.80}$$

After Equation (3.80) is substituted into Equation (3.78), Equation is obtained.

$$\dot{x}_2 = f(x_1, x_2, w(t), t) + b\,\frac{u_0 - z_3}{b_0} \tag{3.81}$$

Since b_0 is the approximation of b, and z_3 is the estimation of the total disturbances, it is assumed that $z_3 \approx f\big(x_1, x_2, w(t)\big)$ and $b_0 \approx b$. Therefore, Equation (3.81) becomes Equation (3.82).

$$\dot{x}_2 = \ddot{x}_1 = u_0 = k_p(r - z_1) - k_d z_2 \tag{3.82}$$

Since z_1 is the estimations of x_1, and z_2 is the estimations of x_2, Equation (3.82) can be written as Equation (3.83) after the laplace transform is applied.

$$x_1 s^2 = k_p(r - x_1) - k_d x_1 s \tag{3.83}$$

After rearranging Equation (3.83), the closed-loop transfer function of the controller is obtained as Equation (3.84).

$$G(s) = \frac{x_1}{r} = \frac{y}{r} = \frac{k_p}{(s^2 + k_d s + k_p)} \tag{3.84}$$

The controller can be tuned with one paremeter which is the controller bandwidth (ω_c) by equating the characteristic equation of the controller to a desired characteristic equation given in Equation (3.85).

$$(s + \omega_c)^2 = s^2 + 2\omega_c s + \omega_c^2 \tag{3.85}$$

Therefore, the controller gains are selected accordingly as shown in Equation (3.86).

$$\begin{bmatrix} k_p \\ k_d \end{bmatrix} = \begin{bmatrix} \omega_c^2 \\ 2\omega_c \end{bmatrix} \tag{3.86}$$

3.2.2.2.1 Extended State Observer Design

Consider an observer that has the state-space representation given in Equations (3.87) and (3.88) (Tan & Fu, 2015).

$$\dot{z} = A_z z + B_z u + L_o(y - \hat{y}) \tag{3.87}$$

$$\hat{y} = C_z z \tag{3.88}$$

where,

$$A_z = \begin{bmatrix} 0 & 1 & 0 \\ 0 & 0 & 1 \\ 0 & 0 & 0 \end{bmatrix} \tag{3.89}$$

$$B_z = \begin{bmatrix} 0 \\ b \\ 0 \end{bmatrix} \tag{3.90}$$

$$C_z = \begin{bmatrix} 1 & 0 & 0 \end{bmatrix} \tag{3.91}$$

$$L_o = \begin{bmatrix} \beta_1 \\ \beta_2 \\ \beta_3 \end{bmatrix} \tag{3.92}$$

When Equation (3.88) is substituted into Equation (3.87),

$$\dot{z} = \underbrace{(A_z - L_o C_z)}_{A'_z} z + B_z u + L_o y \tag{3.93}$$

Therefore, the system might also be represented as Equation (3.94).

$$\dot{z} = A'_z z + B_z u + L_o y \tag{3.94}$$

where,

$$A'_z = A_z - L_o C_z = \begin{bmatrix} -\beta_1 & 1 & 0 \\ -\beta_2 & 0 & 1 \\ -\beta_3 & 0 & 0 \end{bmatrix} \tag{3.95}$$

When the Equations (3.90), (3.92) and (3.95), are substituted into Equation (3.93), the state space representation of the observer can be represented more clearly as Equation (3.96).

$$\dot{z} = \begin{bmatrix} -\beta_1 & 1 & 0 \\ -\beta_2 & 0 & 1 \\ -\beta_3 & 0 & 0 \end{bmatrix} \begin{bmatrix} z_1 \\ z_2 \\ z_3 \end{bmatrix} + \begin{bmatrix} 0 \\ b \\ 0 \end{bmatrix} u + \begin{bmatrix} \beta_1 \\ \beta_2 \\ \beta_3 \end{bmatrix} y \tag{3.96}$$

When Equation (3.96) is expended, and the laplace transformation is applied, it is written more explicitely as Equations (3.97) to (3.99).

$$z_1 = \frac{(y-z_1)\beta_1+z_2}{s} \tag{3.97}$$

$$z_2 = \frac{(y-z_1)\beta_2+bu+z_3}{s} \tag{3.98}$$

$$z_3 = \frac{(y-z_1)\beta_3}{s} \tag{3.99}$$

By substituting Equation (3.98) and (3.99) into Equation (3.97), Equation (3.100) is obtained.

$$z_1 = \frac{y(\beta_1 s^2+\beta_2 s+\beta_3)+bus}{s^3+\beta_1 s^2+\beta_2 s+\beta_3} \tag{3.100}$$

The observer gain matrix (L_o) is obtained by equating the characteristic equation which is the denominator of Equation (3.100) to the third order desired characteristic equation given in Equation (3.101).

$$(s+\omega_o)^3 = s^3 + 3\omega_o s^2 + 3\omega_o^2 s + \omega_o^3 \tag{3.101}$$

$$L_o = \begin{bmatrix} \beta_1 \\ \beta_2 \\ \beta_3 \end{bmatrix} = \begin{bmatrix} 3\omega_o \\ 3\omega_o^2 \\ \omega_o^3 \end{bmatrix} \tag{3.102}$$

As shown in Equation (3.102), the observer gain is tuned with one paremeter which is the observer bandwidth (ω_o).

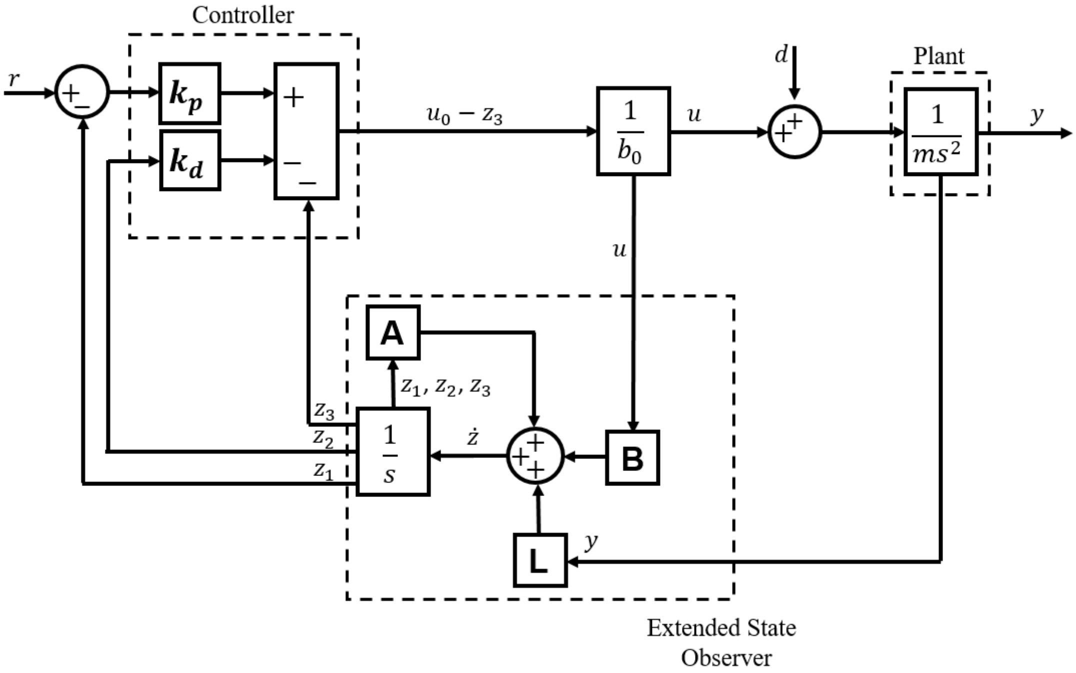

Figure 3.5 Block diagram of a second order ADRC

Note that, Figure 3.5 is a representation for a linear position controller. If an angular position is being controlled, then the term “m” in Figure 3.5 must be replaced with the inertia term of the relevant axis.

An ideal way for tuning/optimizing observer and controller bandwidth is presented by Gao (2006). In the current study, the gains are used as shown in Table 3.5.

Table 3.5 Tuned controller values and gains

	$\boldsymbol{\omega_c(Hz)}$	$\boldsymbol{\omega_o(Hz)}$	$\boldsymbol{k_p}$	$\boldsymbol{k_d}$	$\boldsymbol{\beta_1}$	$\boldsymbol{\beta_2}$	$\boldsymbol{\beta_3}$	$\boldsymbol{b_0}$
x	3	$7\omega_c$	9	6	63	1323	9261	$\frac{1}{m}$
y	5	$7\omega_c$	25	10	105	3675	42875	$\frac{1}{m}$
z	10	$10\omega_c$	100	20	300	30000	1000000	$\frac{1}{m}$
$\boldsymbol{\Phi}$	14	$7\omega_c$	196	28	294	28812	941192	$\frac{1}{I_{xx}}$
$\boldsymbol{\Theta}$	15	$7\omega_c$	225	30	315	33075	1157625	$\frac{1}{I_{yy}}$
$\boldsymbol{\varphi}$	10	$7\omega_c$	100	20	210	14700	343000	$\frac{1}{I_{zz}}$

In order to find out the order of a system, the number of integrators in the block diagram be counted (Han J., 2009). Including actuator dynamics in the controller design increases the system's bandwidth and might be needed to be dealt with by increasing the order of the ESO and the ADRC to three (Aydemir & Arikan, 2020). Calculations for the 3rd or higher orders of ADRC are given in detail by Güçlü (2020) and Aydemir (2016). In the current study, even if the actuator dynamics are also considered which augments the system to a 3rd order system, a 2nd degree of ADRC is found to be sufficient. However, the degree of order of the ADRC should be increased when a 2nd order ADRC is insufficient.

3.2.2.3 Inverse Mapping

The Inverse Mapping Block is mainly composed of lookup tables. A lookup table is the array of values that holds the previously collected input and output data. Then, it gives the corresponding output value to a given input according to its holding data.

3.2.2.4 Implementation of the Wing Model (Aerodynamic Model)

In the 3D flight control case where the ADRCs are utilized, the aerodynamic model that was introduced in Section 2 is implemented in the control structure by Matlab Functions, as shown in Figure 3.6. The cycle-averaged values of the forces and the moment acting on the wing roots are calculated according to the control input values coming from the inverse function blocks.

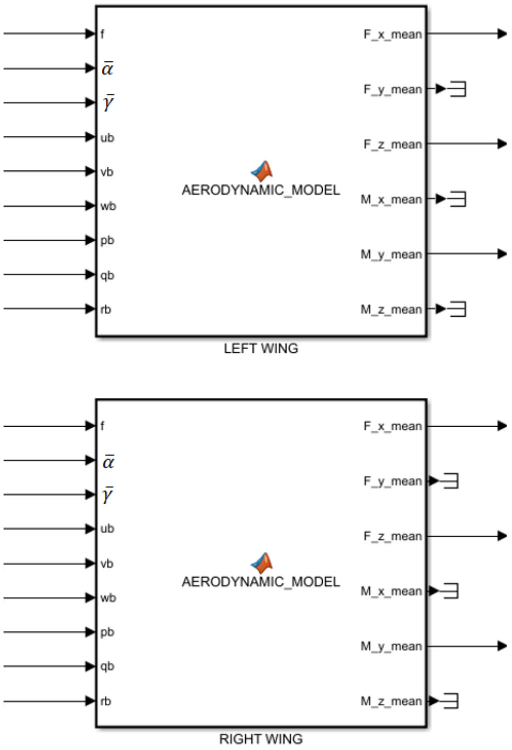

Figure 3.6 Aerodynamic model code that is embeded into Matlab Function blocks in MATLAB/Simulink

The created force in the y_B-axis and moments in the x_B and z_B axes are negligibly small during the flapping motion. Therefore they are not modelled in the aerodynamic model as shown in Figure 3.6. Still, it is possible to create moments around the axes mentioned above by creating asymmetric forces as insects do. For example, to create a positive roll moment (M_x), an asymmetric vertical force can be created where the upward force created by the left wing is higher than the upward force created by the right wing. The distance between the wing root and the body's center of gravity acts as a moment arm, and the value of the torque applied is equal to the distance times the difference of the forces.

3.3 Bio-Inspired Control of the Flapping-Wing MAV

3.3.1 Central Pattern Generators (CPGs)

CPG’s are biological neural networks that are located at the spinal cord and generate rhythmic motions of vertebrates (Kiehn & Butt, 2003). 2.7% of the central nervous system is located at the spinal cord, and motor behaviors such as walking, chewing, and breathing are controlled with CPGs there (Hartmann et at., 1994). CPGs produce rhythmic outputs without the need for rhythmic inputs from the brain or feedback mechanisms (Marder & Bucher, 2001; Steuer & Guertin, 2019). In addition to the vertebrates, Barnes & Gladden (2012) explain that CPGs can play a role in some insect flights, such as grasshoppers, and sensory inputs can also act as feedback and change central rhythm production.

3.3.2 CPG Model

The CPG model that is implemented to the controller is obtained from Chen et al. (2021), which is based on the model of Ijspeert & Crespi (2007). The equations of the CPG model is given in Equations (3.103) to (3.106).

$$\ddot{b} = k_b\big(0.25k_b(B - b) - \dot{b}\big) \tag{3.103}$$

$$\ddot{m} = k_m(0.25k_m(M - m) - \dot{m}) \tag{3.104}$$

$$\dot{P} = \left[\frac{(1+R)^2}{4R} - \frac{R^2-1}{4R} sign(sin(P))\right]\omega \tag{3.105}$$

$$\alpha = b + mcos(P) \tag{3.106}$$

The CPG model is adapted to the current study such that; b is the offset state that can be used as the mean feathering angle $(\bar{\alpha})$, m is the magnitude state, and can be used as the stroke positional amplitude (γ_{amp}). P is the phase state; k_b and k_m are the constants that determine the convergence rate of states b and m to values of B and M, respectively. R is the time ratio between downstroke and upstroke and fixed to 1.

The CPG model created in the Matlab/Simulink using Equations is given in Figure 3.7.

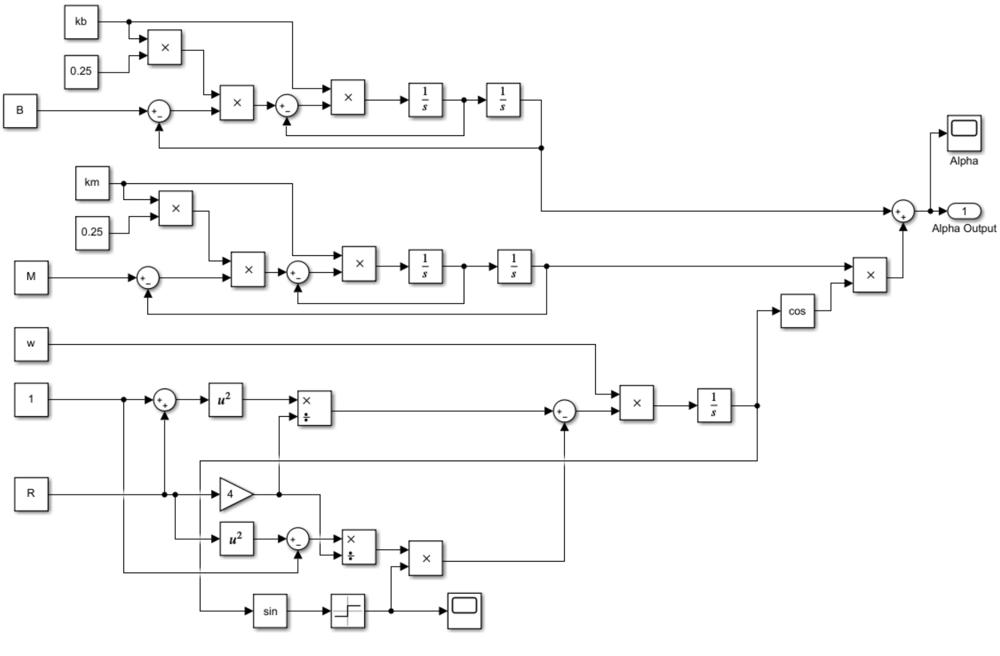

Figure 3.7 CPG model created in Matlab/Simulink using Equations

3.3.3 CPG Based Bio-inspired Closed-Loop Control

The model given in Section 3.3.2 is implemented into controller as shown in Figure 3.8.

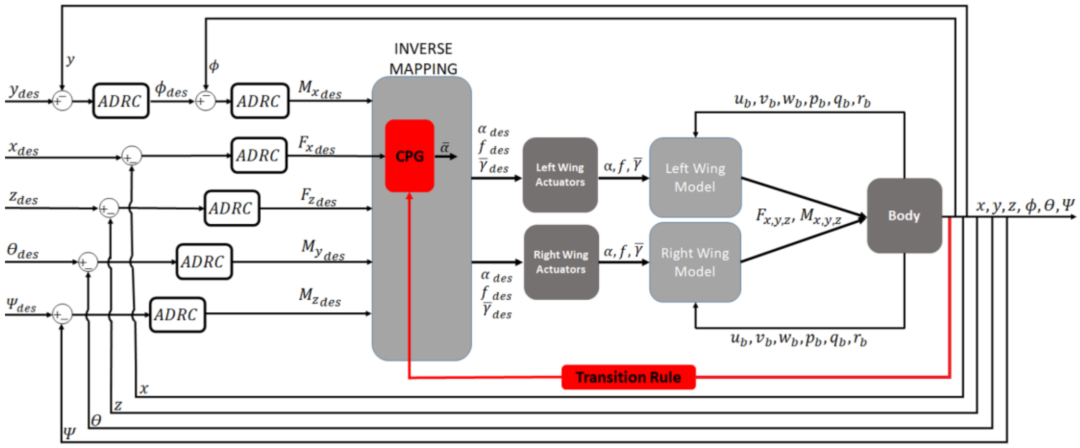

Figure 3.8 CPG imlemented control system demonstration for the 3D flight

Since the flapping motion is assumed to be generated with CPGs in this case, the Equations (3.69) and (3.70) may be rewritten as Equations (3.107) and (3.108).

$$\alpha_{des_l} = \bar{\alpha}_{CPG} + \Delta\bar{\alpha} \tag{3.107}$$

$$\alpha_{des_r} = \bar{\alpha}_{CPG} - \Delta\bar{\alpha} \tag{3.108}$$

In this study, CPGs are only responsible for control in one direction: the horizontal plane. Therefore, they are only employed to determine the mean feathering angle input but not the other controls. Considering the fact that the desired flapping frequency and the desired mean stroke positional angle are still getting directly from ADRCs, Equations (3.71) and (3.72) are still valid for flapping frequency calculations.

Using CPGs as the rhythmic signal generators aim to provide fast transitions between flight modes when necessary. For example, an immediate transition from hover mode to a sudden escape maneuver is possible with CPG inputs.

In the current section, the escape maneuver of a hawkmoth is imitated using a CPG implemented controller. A scenario presented in the literature is simulated (Cheng et al., 2011 & Animal Flight, 2013). Cheng et al. (2011) used a human hand to startle a hovering hawkmoth and make an immediate escape maneuver towards backward and recorded this with a high speed camera (Animal Flight, 2013). Figure 3.9 shows some instants from the escape maneuver of startled hawkmoth.

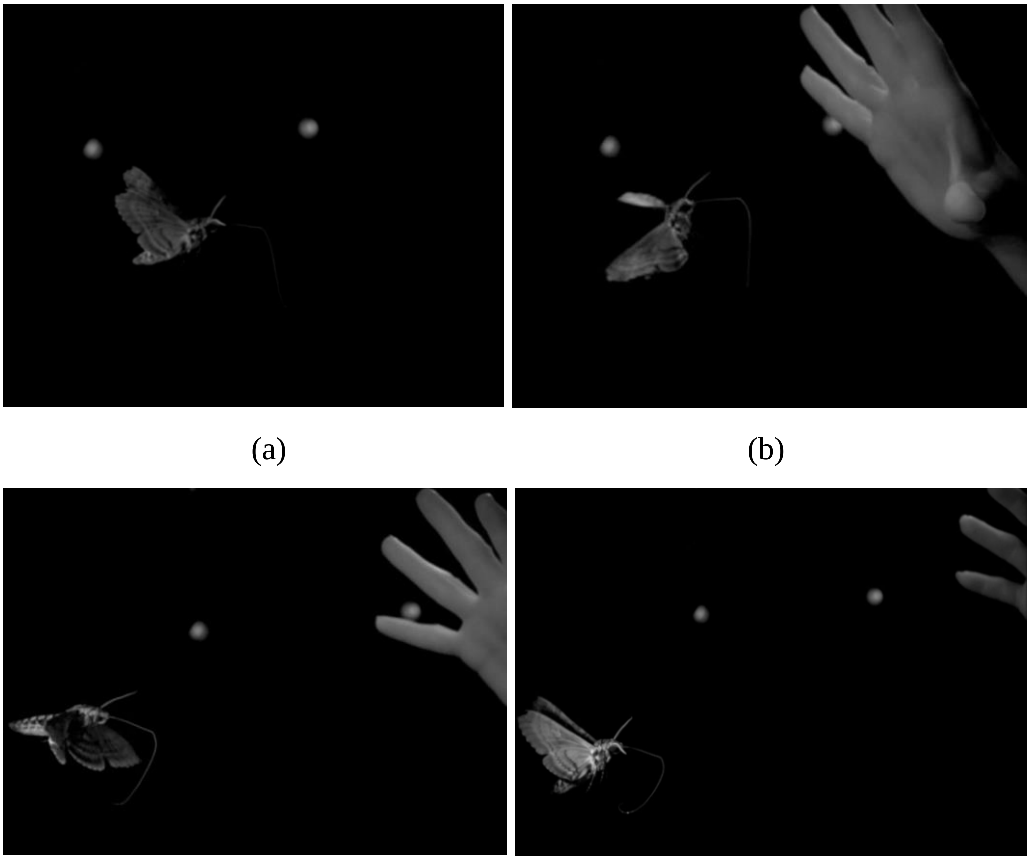
(a) (b)

(c) (d)

Figure 3.9 Instant shots of a startled hawkmoth (Animal Flight, 2013)

In Figure 3.9a, the hawkmoth is hovering, and in Figure 3.9b, it is instantly stimulated with a human hand. The hawkmoth immediately responds to the stimulation by changing its stroke plane angle, and consequently, the body pitch angle and escapes backward. In Figure 3.9c, it tilts itself down to recover its original body pitch angle but overshoots and in Figure 5.3d it recovers its original position.

In the current study, the instant of stimulation is determined simply by a 0 - 1 (zero - one) rule, and according to the rule, the hovering flapping-wing MAV will keep its position when the input is 0, which means there is no stimulation, but in the case of stimulation, the input is 1 so, the flapping-wing MAV will make an immediate escape towards backward by changing its mean feathering angle $(\bar{\alpha})$. At the instant of stimulation, the flapping-wing MAV does not use reference inputs as the primary reference but obeys the rule by following the CPG output.

Table 3.6 Flapping-wing MAV mode transition rule

Rule	**Mode**	**Wing Kinematic (α)**
0	Hover	$\bar{\alpha}$
1	Escape	$\bar{\alpha} - 3°$

CHAPTER 4

CONTROL SIMULATION RESULTS

Flight control simulations are performed in MATLAB/Simulink environment. A fixed time step of 0.001 seconds is preferred to increase the correctness of the solutions.

4.1 Longitudinal (3DOF) Control Results

During the studies, a typical scenario is tought up to be used for 2D flight simulations. The flight scenario is given in Table 4.1.

Table 4.1 Scenario to be simulated for the longitudinal flight

Time Period	**Desired Action**
0-10 seconds	Take off and reach a height of 20 cm
10-20 seconds	Hover for 10 seconds
20-40 seconds	Move 50 cm forward in the horizontal plane
40-50 seconds	Hover for 10 seconds
50-60 seconds	Land

4.1.1 LQR Results

According to the scenario presented in Table 4.1, simulation results are given in this section. The system was able to track the command inputs as shown in Figure 4.1, and other states are stabilized as shown in Figure 4.2.

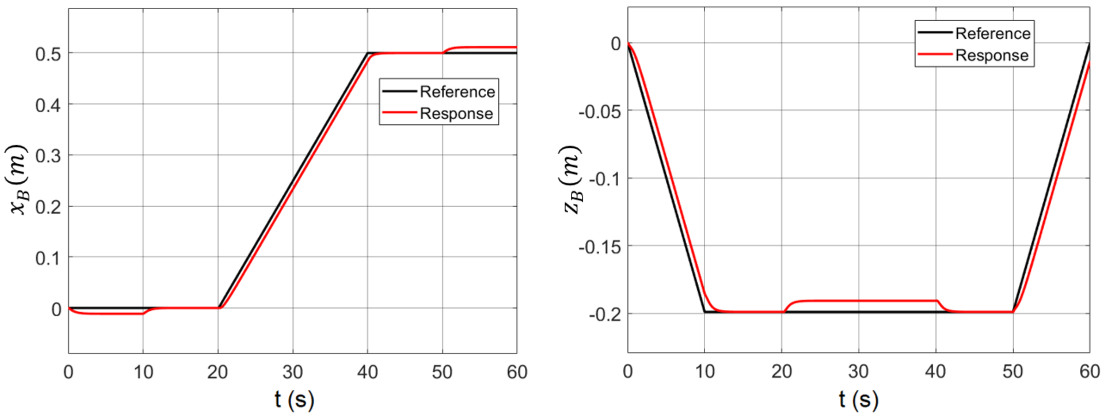

(a) (b)

Figure 4.1 The behavior of the system when the gain is calculated with the LQR technique (a) behavior on the horizontal plane (b) behavior on the vertical plane

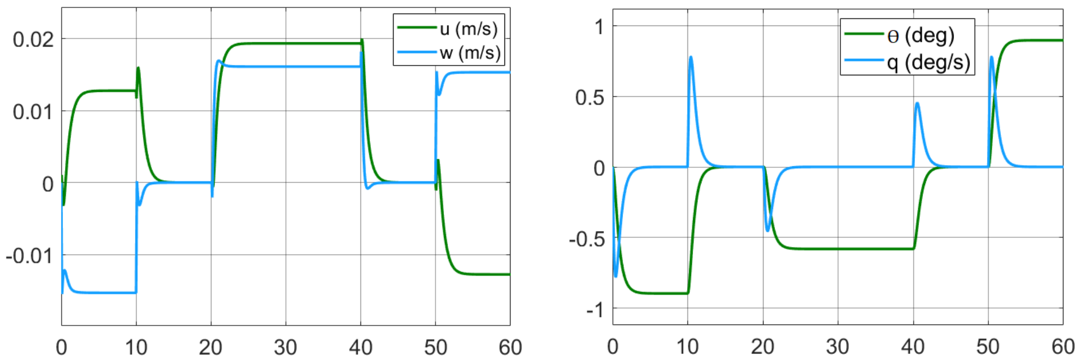

(a) (b)

Figure 4.2 System's other states' responses when the gains are calculated with the LQR technique (a) linear velocities (u and w), (b) body pitch angle (Θ) and body pitch rate (q)

Figure 4.3 gives the controller responses to make the system achieve the desired state values.

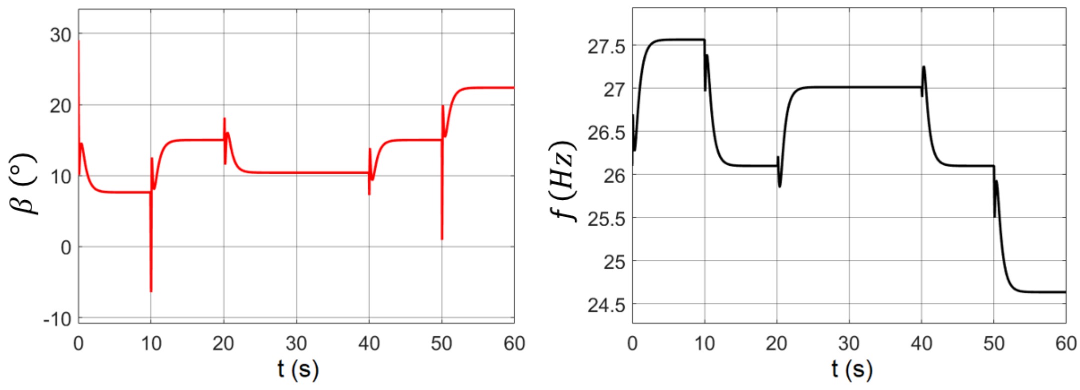

(a) (b)

Figure 4.3 Response of the controller when the gains are calculated with the LQR technique (a) changes in the stroke plane angle (β) (b) changes in the flapping frequency (f)

To test the controllers against the disturbances, a combination of perturbative inputs with varying frequencies are applied to the system responses, as shown in Figure 3.3. Instead of the sensory noise, these signals are considered as the perturbative forces and moments affecting the system. Care has been taken to ensure that the frequencies of the perturbation signals are within the system's bandwidth. The perturbative signals that are applied to position states of the system are given in Figure 4.4.

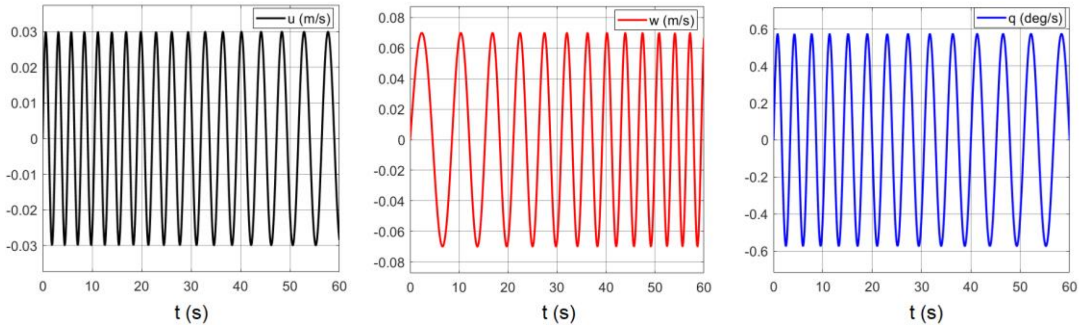

(a) (b) (c)

Figure 4.4 Disturbance Signals (a) applied to the linear velocity state x_b (b) applied to the linear velocity state z_b (c) applied to the pitching rate state q

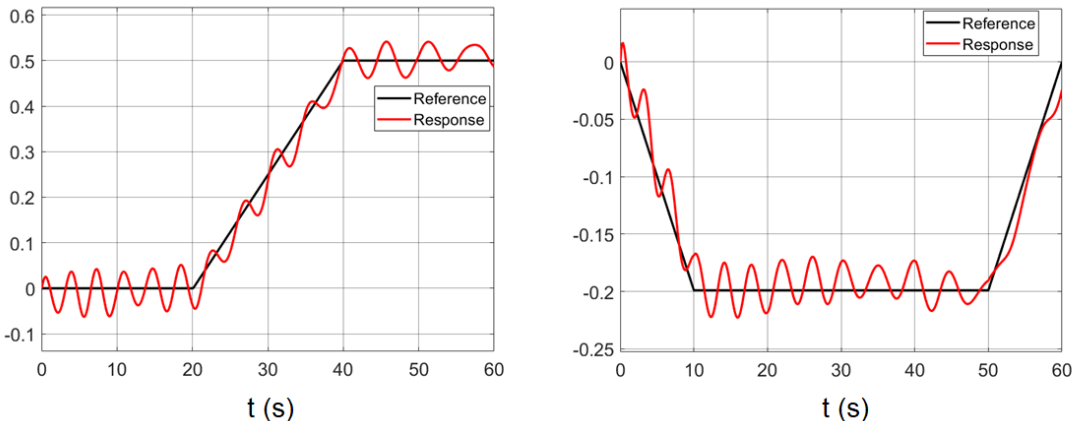

(a) (b)

Figure 4.5 The behavior of the system in the existance of disturbances when the gain is calculated with the LQR technique (a) behavior on the horizontal plane (b) behavior on the vertical plane

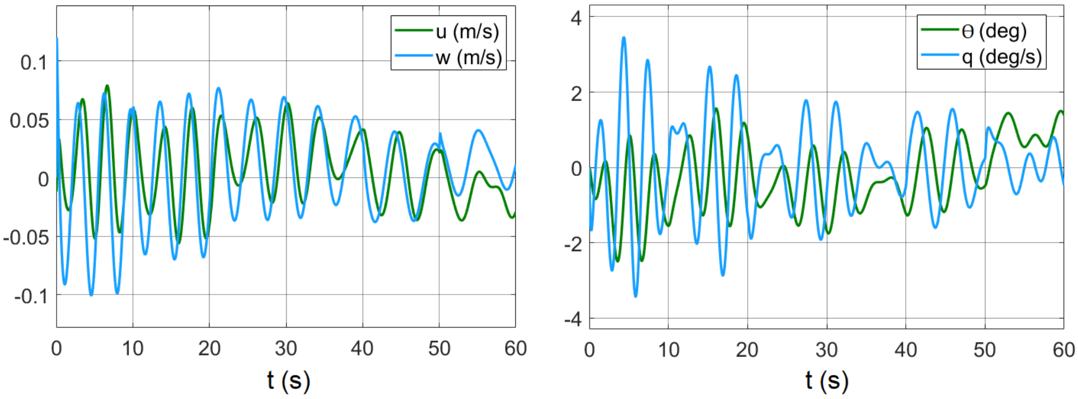

(a) (b)

Figure 4.6 System's other states' responses in the existence of disturbances when the gains are calculated with the LQR technique (a) linear velocities (u and w), (b) body pitch angle (Θ) and body pitch rate (q)

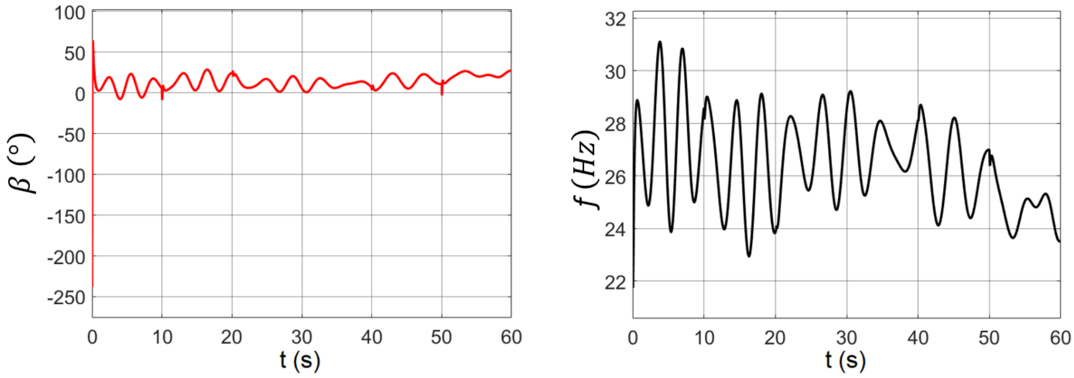

(a) (b)

Figure 4.7 Response of the controller in the existence of disturbances when the gains are calculated with the LQR method (a) changes in the stroke plane angle (β) (b) changes in the flapping frequency (f)

4.1.2 CDM Results

The scenario presented in Table 4.1 is simulated in this section, but this time using the controller based on CDM. The system was able to track the command inputs also with the CDM-based controller. The results are shown in Figure 4.8 and Figure 4.9.

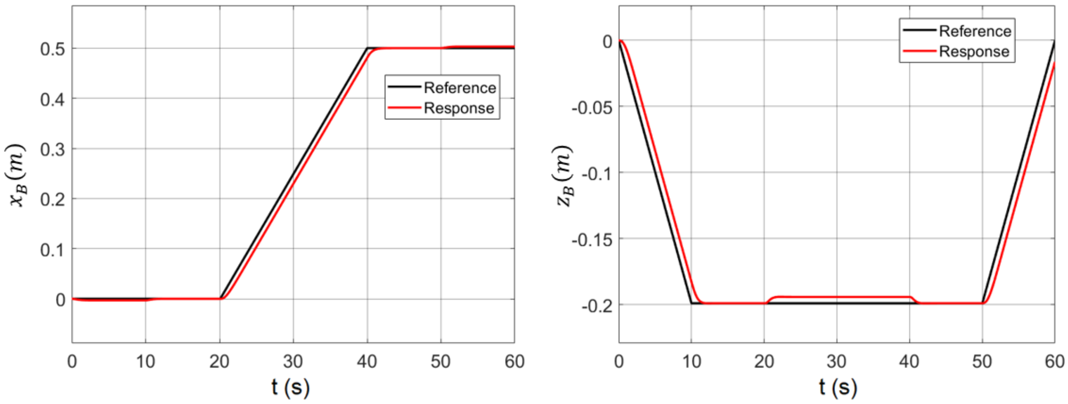

(a) (b)

Figure 4.8 The behavior of the system when the gain is calculated with the CDM (a) behavior on the horizontal plane (b) behavior on the vertical plane

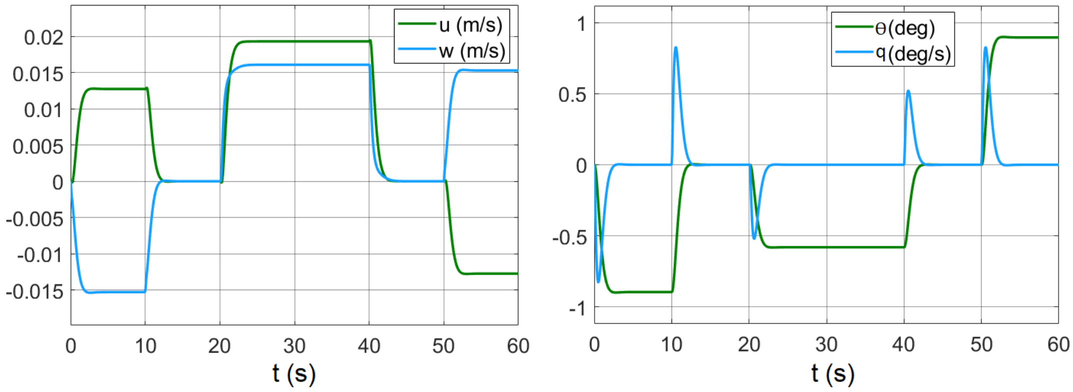

(a) (b)

Figure 4.9 System's other states' responses when the gains are calculated with the CDM (a) linear velocities (u and w), (b) body pitch angle (Θ) and body pitch rate (q)

The changes in the control signals are presented in Figure 4.10.

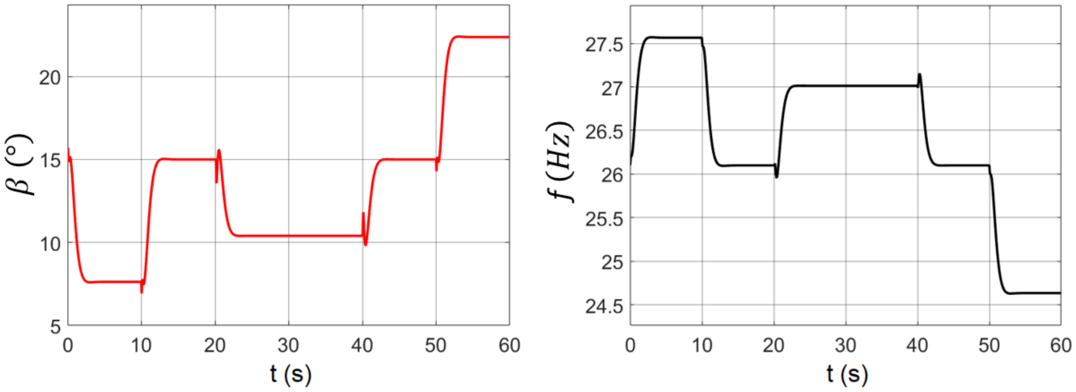

(a) (b)

Figure 4.10 Response of the controller when the gains are calculated with the CDM (a) changes in the stroke plane angle (β) (b) changes in the flapping frequency (f)

The disturbances given in Figure 4.4 are applied to the system and the controller was able to reject the disturbance as shown in Figure 4.11 and Figure 4.12.

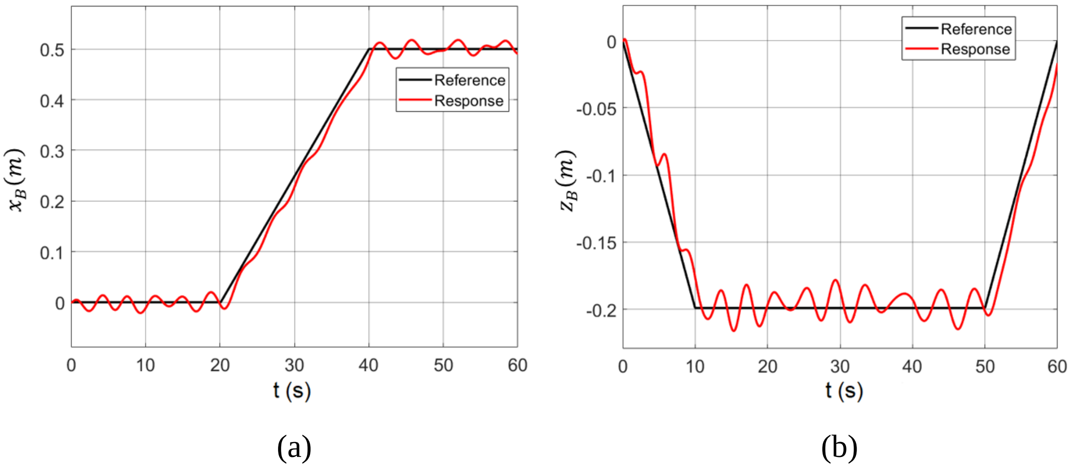

Figure 4.11 The behavior of the system in the existence of disturbances when the gain is calculated with the CDM (a) behavior on the horizontal plane (b) behavior on the vertical plane

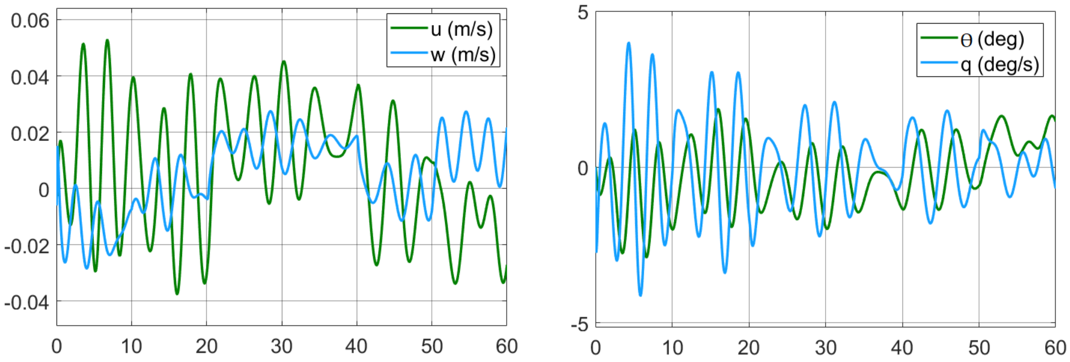

Figure 4.12 System's other states' responses in the existence of disturbances when the gains are calculated with the CDM (a) linear velocities (u and w), (b) body pitch angle (ϴ) and body pitch rate (q)

Figure 4.13 gives the response of the CDM controller when the system is forced to track the reference inputs. The fluctuations in control signals occurred to compensate for the disturbance signals.

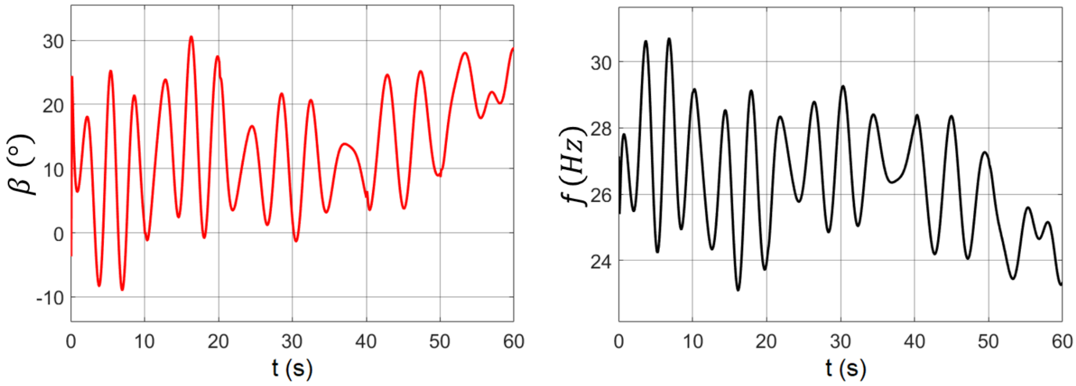

Figure 4.13 Response of the controller in the existence of disturbances when the gains are calculated with the CDM (a) changes in the stroke plane angle (β) (b) changes in the flapping frequency (f)

4.1.3 Comparison of the Controllers Designed for 2D Flight

Steady-state errors arose with the LQR controller between seconds 0-10, 20-40, and 50-60, which are the instants of reference input changes. However, no crucial steady-state error appeared with the CDM controller. The differences between the cases in the means of steady-state error level are observed more clearly with the undisturbed response comparisons shown in Figure 4.14.

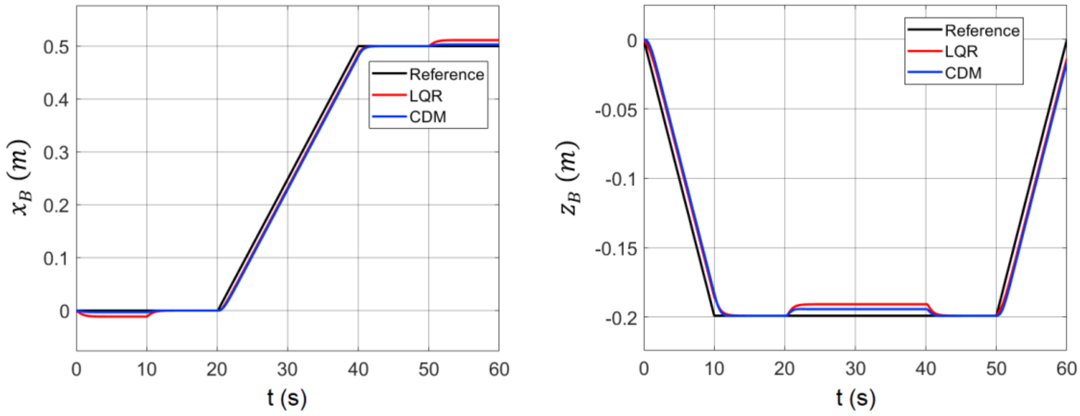

Figure 4.14 The behavior of the system with different control methods without any perturbative inputs (a) behavior on the horizontal plane (b) behavior on the vertical plane

The CDM-based control is also more satisfactory in disturbance rejection since the effects of the applied disturbances are attenuated more with the CDM-based controller than the LQR, as shown in Figure 4.15. On the other hand, non of the controllers outclass to the other in response times.

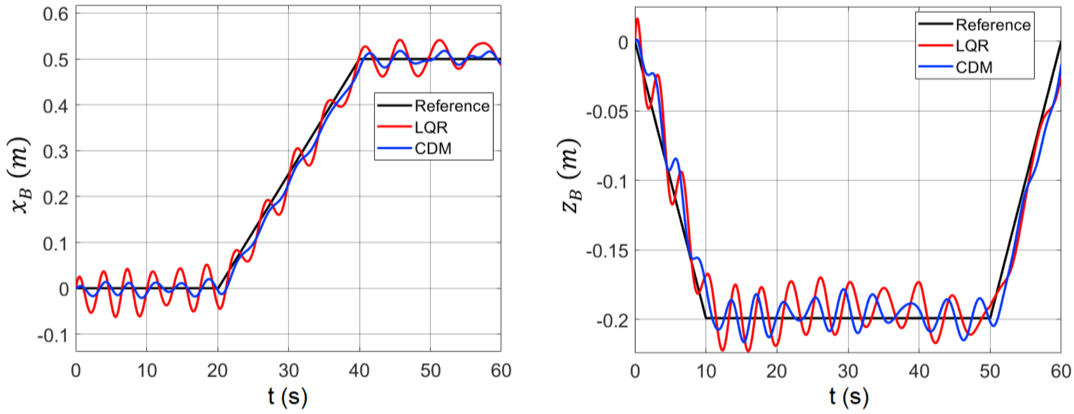

Figure 4.15 The behavior of the system with different control methods in the existance of disturbances (a) behavior on the horizontal plane (b) behavior on the vertical plane

Figure 4.16 and Figure 4.17 compare the controller efforts in the cases without and with disturbances, respectively. The difference in the controller responses is observed more clearly in Figure 4.16, with the case without added disturbance signals. The LQR controller realized more aggressive input effort compared to the CDM at the instants of reference input change.

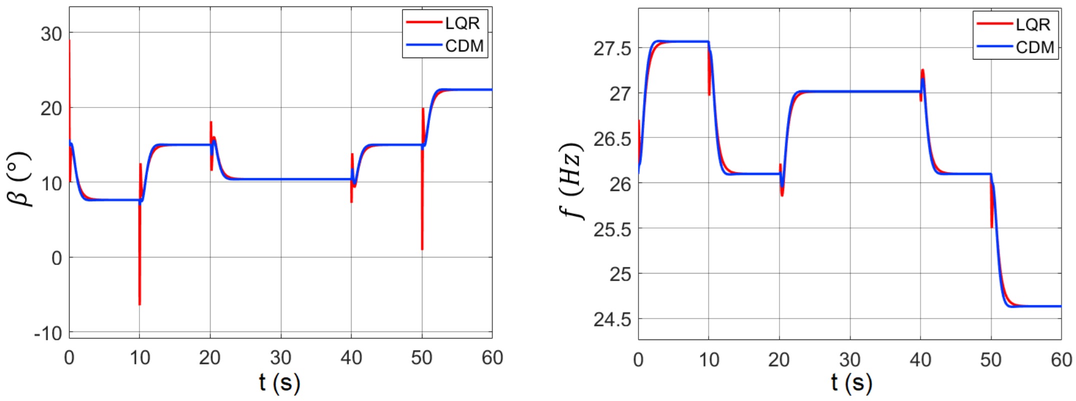

(a) (b)

Figure 4.16 The responses of the controllers with different control methods (a) stroke plane angle input (b) flapping frequency input

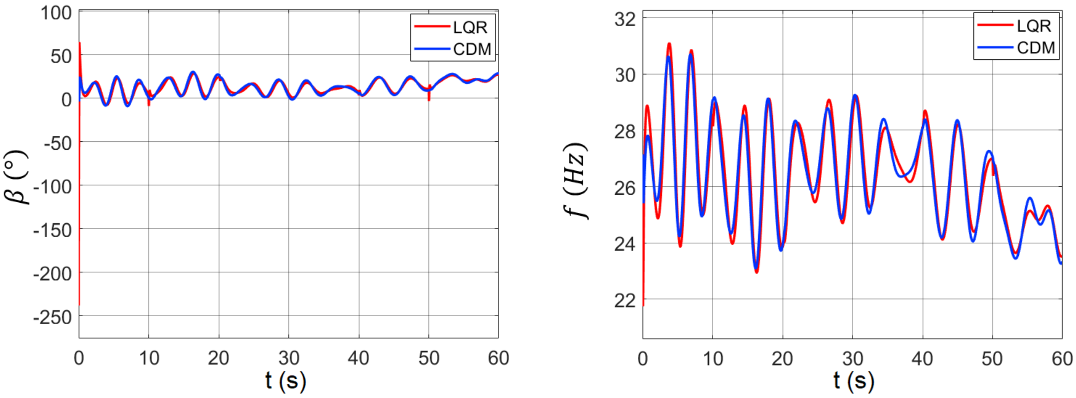

(a) (b)

Figure 4.17 The responses of the controllers with different control methods in the existance of disturbances (a) stroke plane angle input (b) flapping frequency input

Since the longitudinal and lateral dynamics of a flapping-wing MAV are decoupled during 3D flight as given in Figure 3.2, with a similar control approach also for the lateral dynamics, controlling a flapping-wing MAV in 3D flight is possible.

4.2 3D Flight Simulation Results

The scenario for the 3D flight simulations is given in Table 4.2.

Table 4.2 Scenario to be simulated for the 3D flight

Time Period	**Desired Action**
0-10 seconds	Take off and reach a height of 20 cm
10-20 seconds	Hover for 10 seconds
20-40 seconds	Move 50 cm forward in the x_G-axis
40-50 seconds	Hover for 10 seconds
50-70 seconds	Move 50 cm in the y_G-axis
70-80 seconds	Hover for 10 seconds
80-100 seconds	Get back to the initial position by moving backward in the x_G-axis and moving in the $-y_G$-axis at the same time
100-110 seconds	Hover for 10 seconds
110-120 seconds	Land

4.2.1 ADRC Results

In Figure 4.14 the response of the flapping-wing MAV to the reference inputs that are explicated in Table 4.2 are presented.

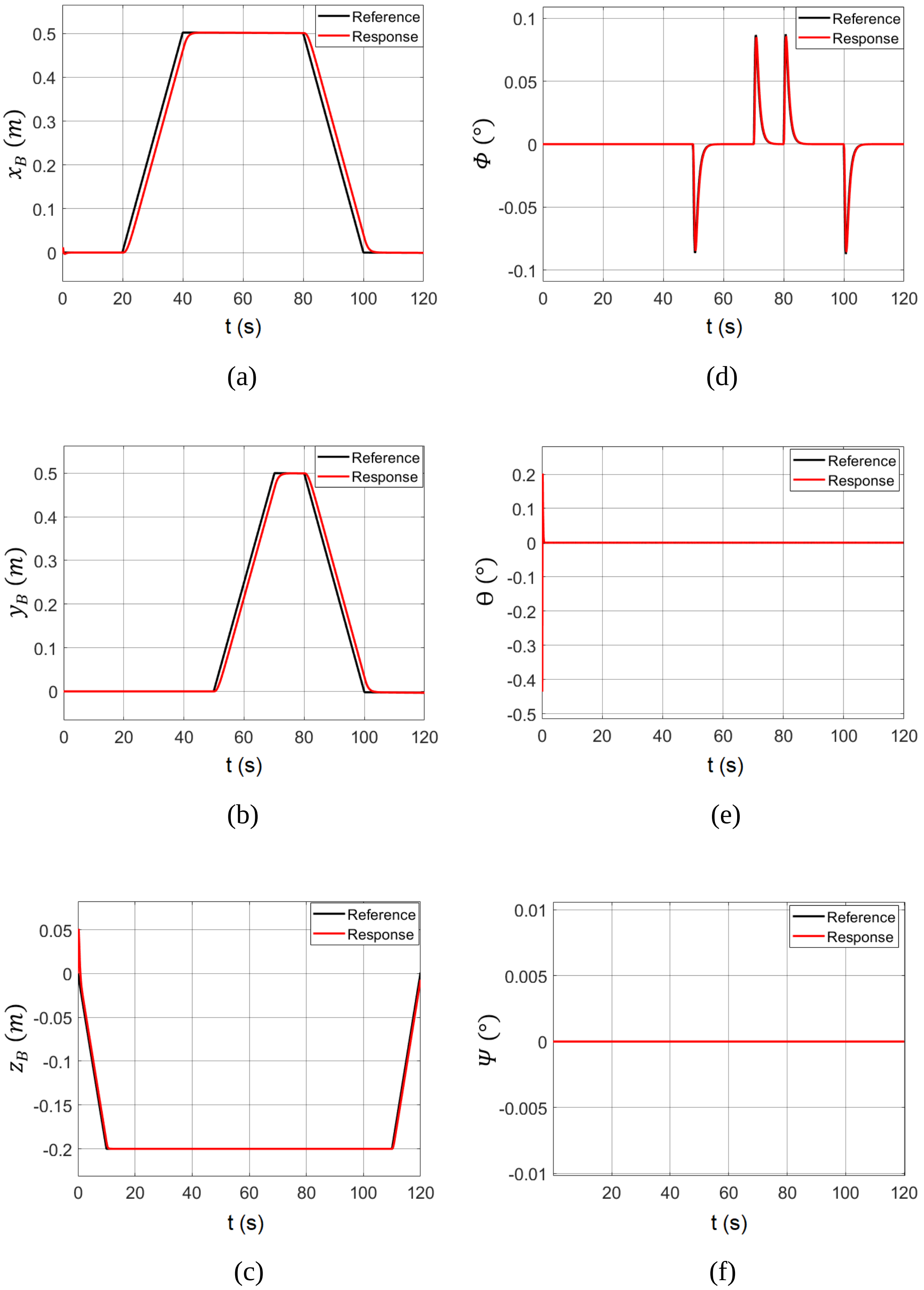

Figure 4.18 The behavior of the system with the ADRC (a-c) linear positions, (d-f) rotational positions

As shown in Figure 4.19, the flapping-wing MAV tracked the reference inputs with little controller effort.

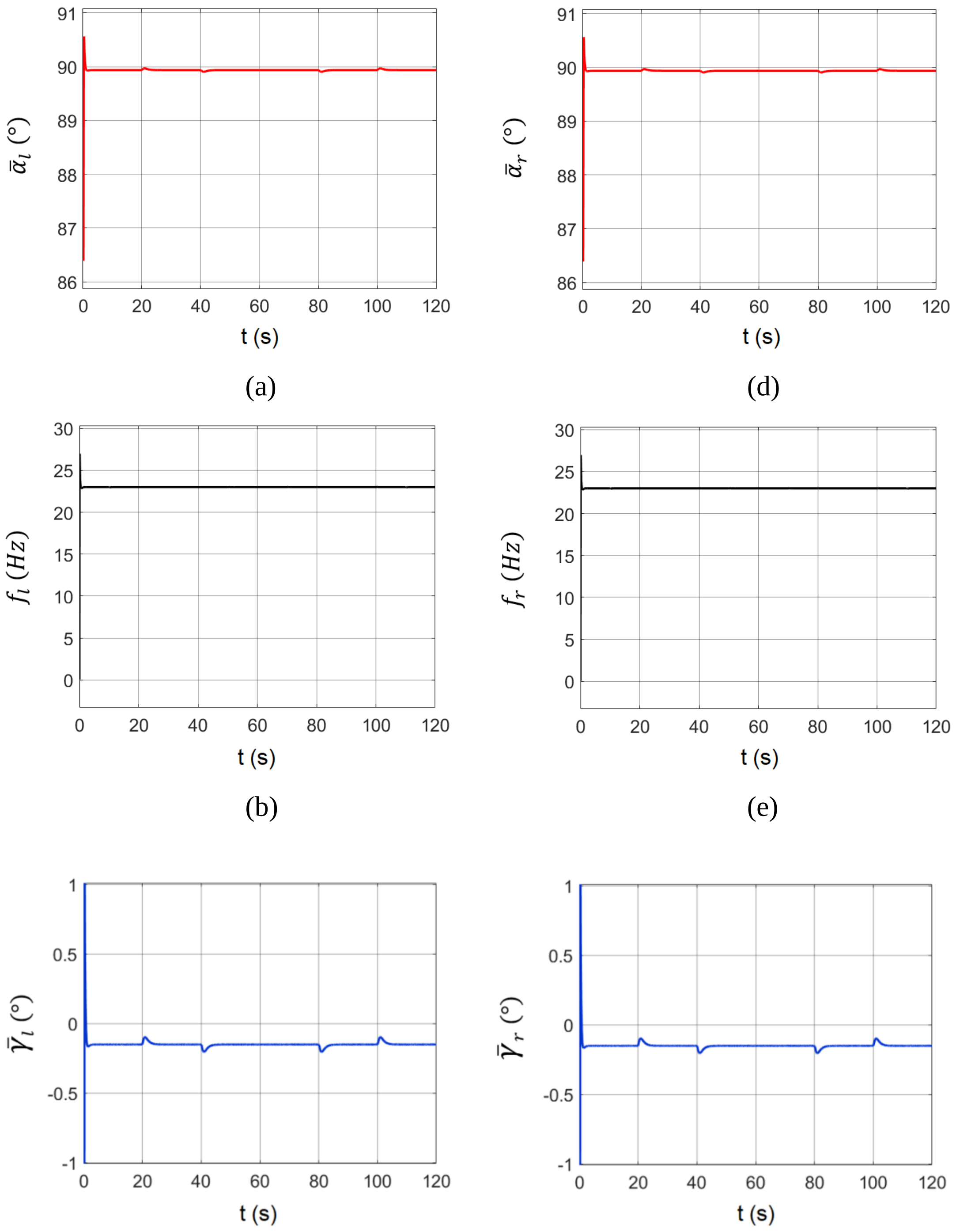

(a) (d)

(b) (e)

(c) (f)

Figure 4.19 Response of the controller (a-c) left wing controls (d-f) right wing controls

4.2.2 ADRC Results in The Existence of Disturbances

The robustness of the LADRC in 3D flight needs to be tested to ensure its employability for the real flight by adding disturbances to the system and adding some unmodelled nonlinearities to the wing model. Even a finely-modelled wing model may have some differences with the actual wing. Therefore, a controller that operates properly during simulations may still have incompleteness when used on the real system. In the current section, to test the solidity of the controller in the case of uncertainties and undermodelled wing features, some random changes are applied to the aerodynamic model without any changes in the inverse mapping block to create a poorly modelled wing case instead of adding only external disturbances. This way, the controller's ability to overcome the uncertainties is proven.

In Figure 4.20, the applied external disturbances and the ESO estimations are given.

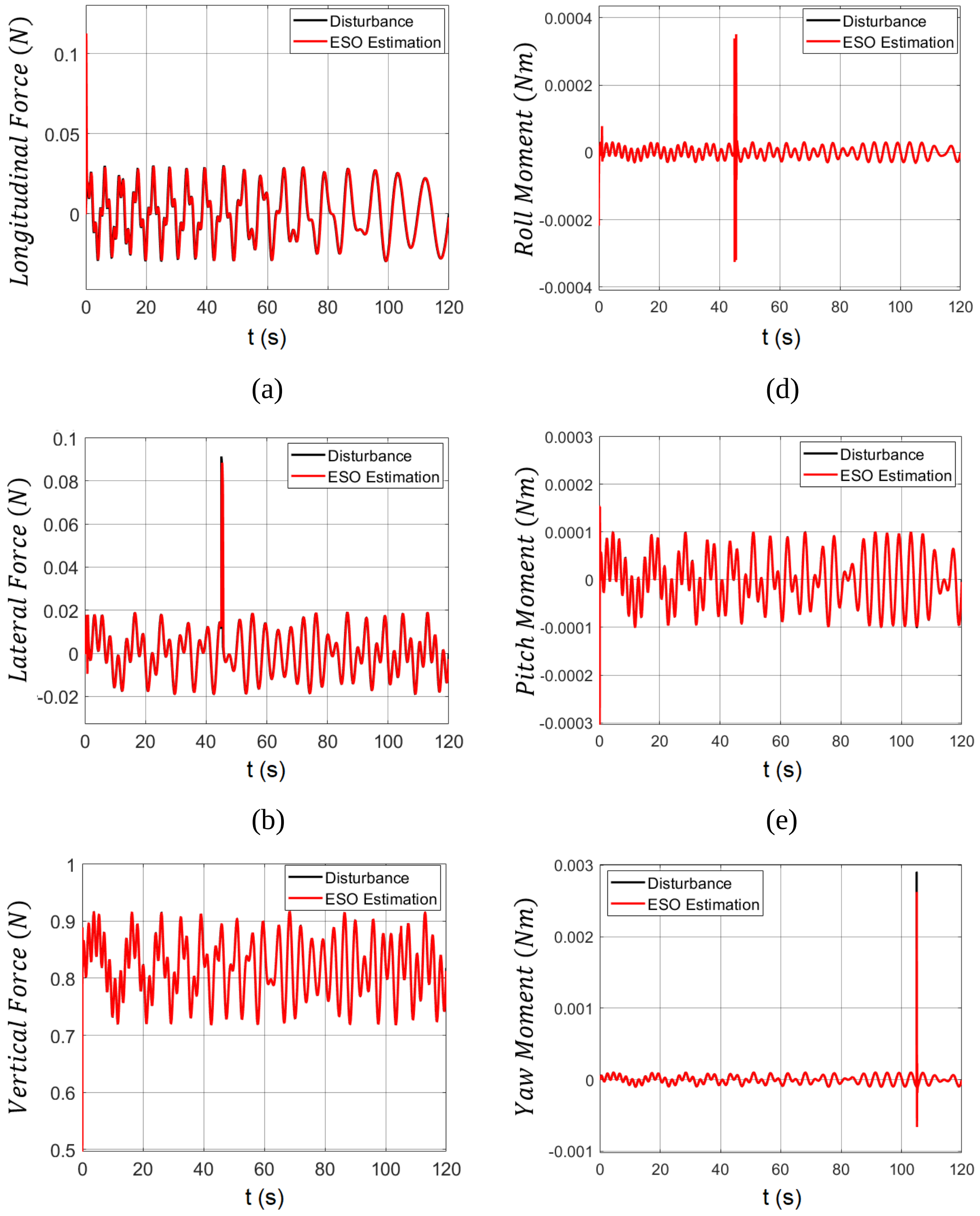

(a) (d)

(b) (e)

(c) (f)

Figure 4.20 Disturbances applied to each state and estimation of the ESO (a-c) Forces (d-f) Moments

The controller was able to reject the external disturbances and compensate for the uncertainties of the wing model. The system's response in the existence of disturbances is given in Figure 4.21.

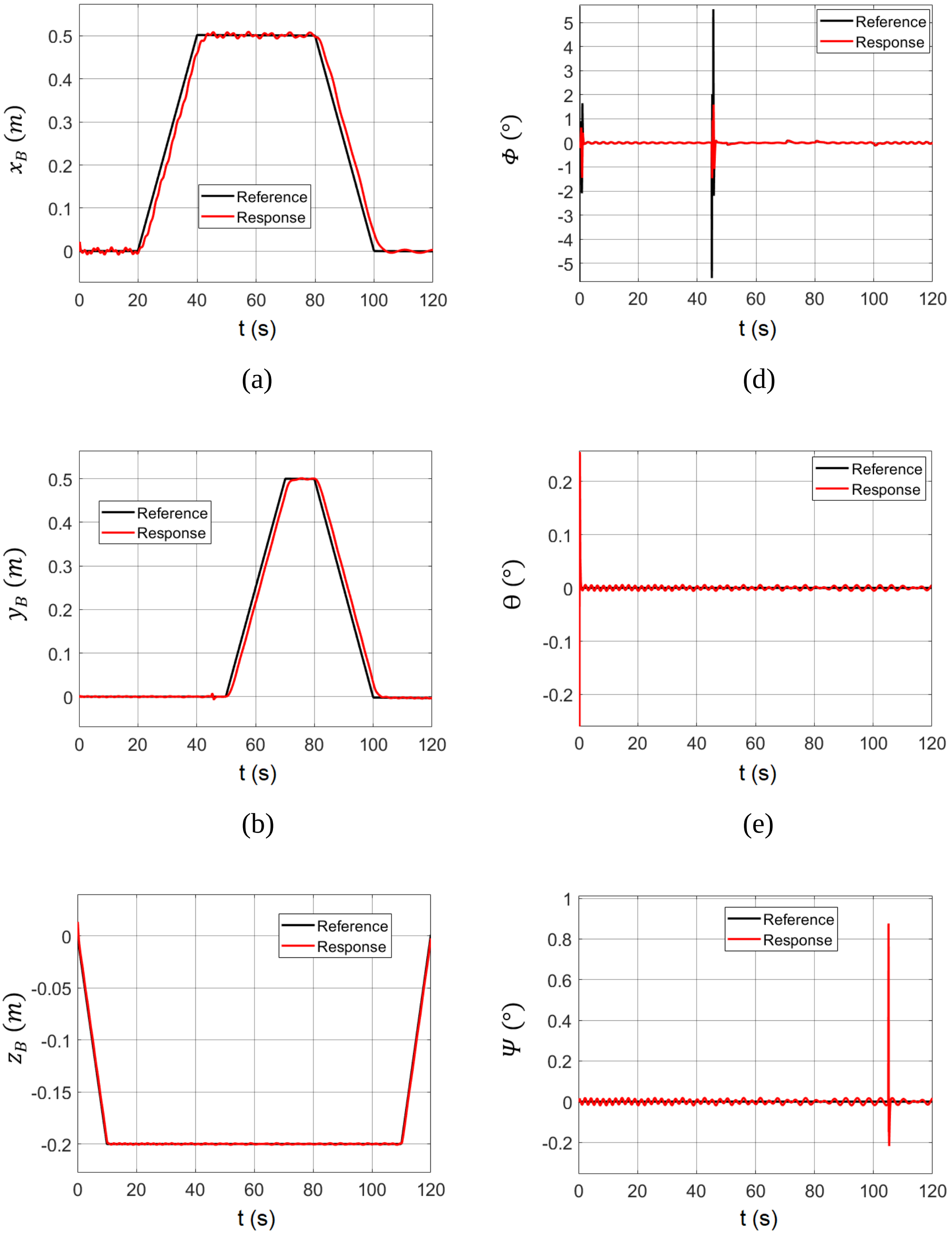

(a) (d)

(b) (e)

(c) (f)

Figure 4.21 The behavior of the system with the ADRC in the existence of disturbances (a-c) linear positions, (d-f) rotational positions

The controllers’ responses in the existence of disturbances and nonlinear wing uncertainties are given in Figure 4.22.

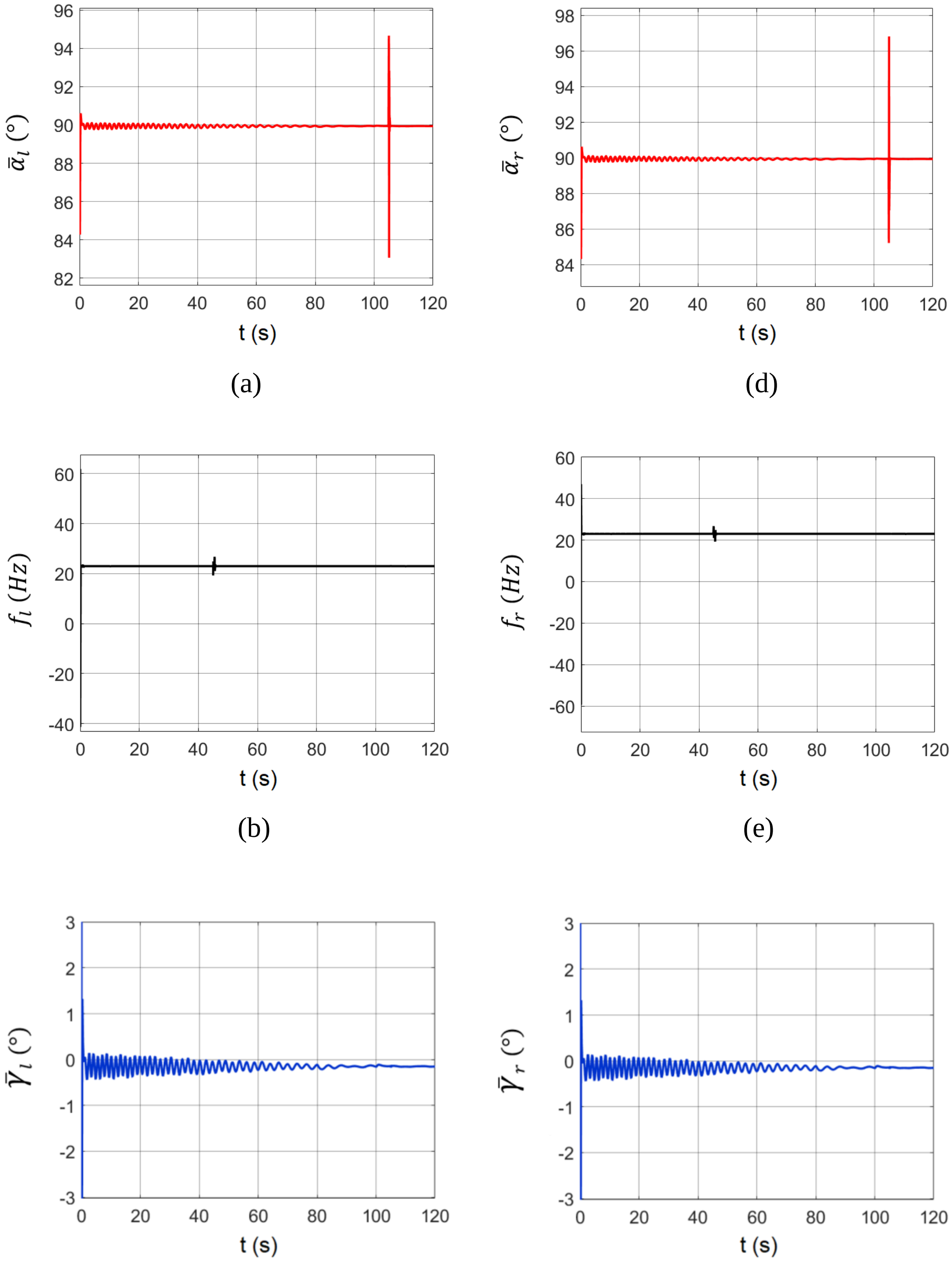

(a) (d)

(b) (e)

(c) (f)

Figure 4.22 Response of the controller in the existence of disturbances (a-c) left wing controls (d-f) right wing controls

4.3 Bio-inspired Control Simulation Results

In the current study, the modelled flapping-wing MAV does not have the same morphological parameters and dynamics with an actual hawkmoth. Therefore, this study does not aim to acquire the same kinematic changes with the sample mentioned above while performing the escape. However, developing the ability of a similar reflexive escape maneuver is targeted using CPGs.

For an immediate backward motion, a hawkmoth alters the mean feathering angle ($\bar{\alpha}$), and together with the backward motion, a total pitch torque is produced. In Figure 4.23, illustration of a hawkmoth escaping from an incoming threat is given (Cheng et al., 2011). The hovering hawkmoth in Phase 1 rapidly pitches itself up and orients its mean feathering angle in Phase 2 to make a sudden backward escape. Afterward, it recovers its original position together with some oscillations at its pitching angle in Phases 3 and 4.

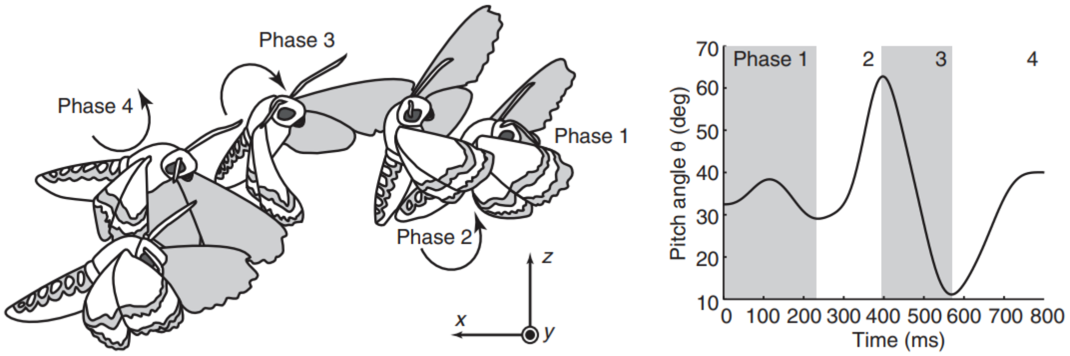

Figure 4.23 Illustration of a hawkmoth's escape maneuver towards backward (Cheng et al. 2011)

As shown in Figure 4.24, at the 100th second, the transition rule becomes 1, which represents there is a treath and the transition from the hover mode to an immediate escape must occur. 0.5 seconds later, the transition rule turns back to 0, and the flapping-wing MAV continues following the reference input.

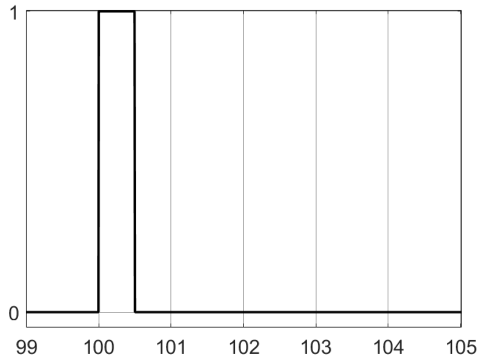

Figure 4.24 The variation of the transition rule which determines the transition instants between flight modes

The reason for determining the stimulation time as 100th second is that to make sure the transient responses of the system completely die out and the flapping-wing MAV is purely hovering so that the reaction of the flapping-wing MAV to the stimulation can clearly be observed.

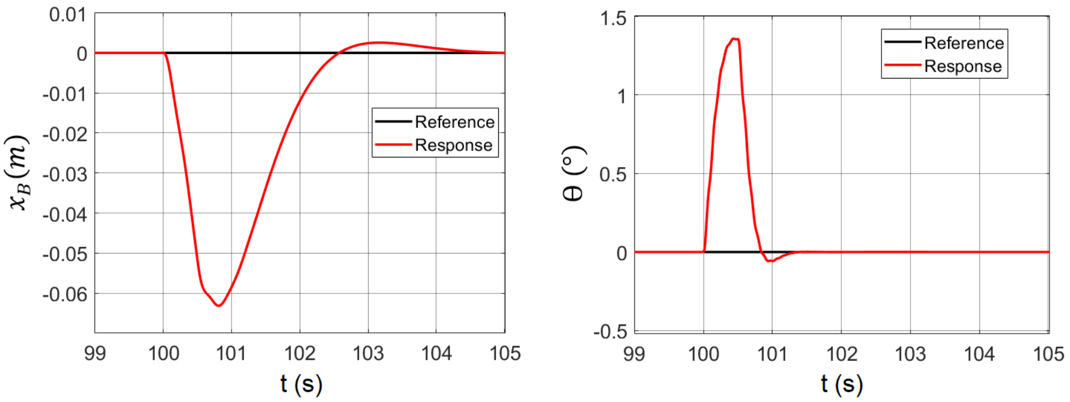

Figure 4.25 The behavior of the flapping-wing MAV with the CPG-based controller to stimulation

As shown in Figure 5.16a, in the existence of any threat coming from en face, regardless of the command input is, the flapping-wing MAV makes an immediate escape nearly 6 cm through backward. Due to the translation of the body, pitch torque occurs, and body pitch position also fluctuates, as shown in Figure 4.25b, similarly to Figure 5.14b. However, unlike a real hawkmoth, no significant, distinguishable loss of altitude is observed during simulations, as shown in Figure 4.26.

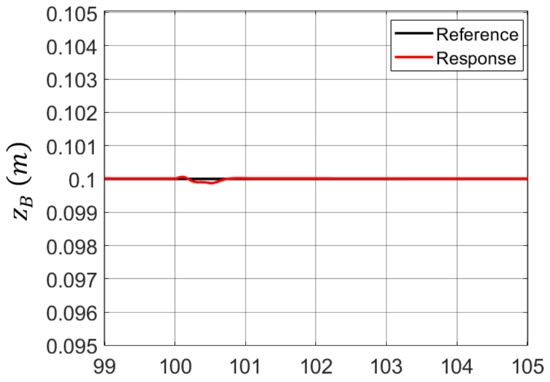

Figure 4.26 The behavior of the flapping-wing MAV in the vertical plane in the case of stimulation

The effects of the backward motion on the altitude state are compensated by the ADRC that is still in charge with controlling the flapping-wing MAV in vertical plane by altering the flapping frequency as shown in Figure 4.27b.

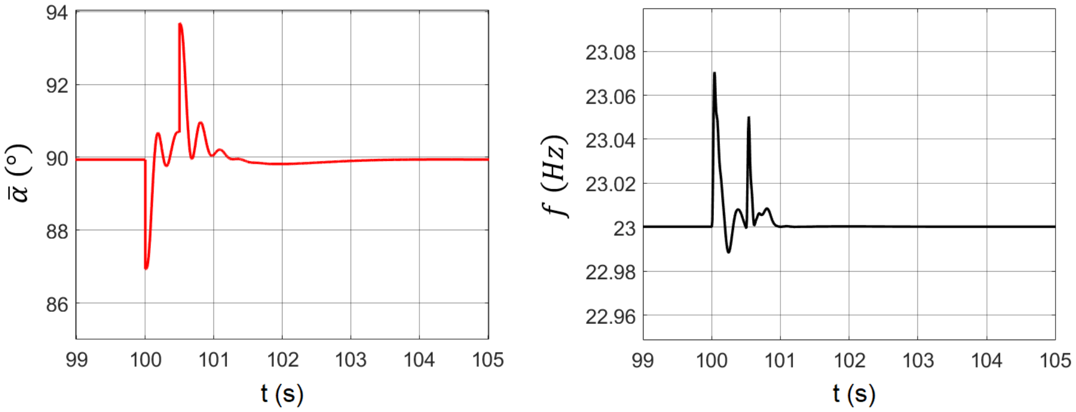

(a) (b)

Figure 4.27 Controllers' responses to the stimulation (a) change of the mean feathering angle ($\bar{\alpha}$) by CPG (b) change of the flapping frequency (f) by ADRC

CHAPTER 5

CONCLUSION AND DISCUSSION

Among the essential outputs achieved during the study is combining the nonlinear aerodynamic model with the models needed to design the control systems. This model calculates the aerodynamic forces and pitching moment created by the flapping motion and surpasses alternating techniques with lower computational costs. This way, the realistic insect wing model is included in the system, and designing control systems for various conditions and objectives became possible. Within future studies, different wing models in different sizes and morphology can quickly be introduced to the code and evaluated in the means of suitability for the ongoing flapping-wing MAV project.

The aerodynamic model developed was validated by comparing its results with the CFD and experimental results. Thus, other than the control simulations, the one who is conducting numerical or experimental studies may forecast approximate results before everlasting numerical analyses or expensive experiments using this aerodynamic model.

In the 2D flight case, an optimal control solution is achieved with LQR control, and the controller performance is compared with another gain calculation technique, the CDM. The CDM worked well in attenuating the effects of the external disturbances. The steady-state error was more distinctive with the LQR control than with the CDM. In the 3D flight case, robust flight simulations against the effects of inaccurate dynamic models and external disturbances are achieved using ADRC. With the ESO estimating the total disturbances, the ADRC can compensate for the effects of unknown dynamics, external disturbances, and imperfections of mathematical models caused by various assumptions. Because of the disturbance rejection ability of ADRC independent from detailed models, it is easily used for different control objectives that prioritize robustness including flapping-wing MAV applications.

An artificial CPG model that outputs the rhythmic flapping motion is implemented into the control structure to get activated in the case of a danger depending on the determined scenario. Designing a CPG-based controller makes achieving an immediate escape maneuver possible without needing feedback information to the mean controller, ADRC. The drawback of the CPG implemented controller in this study comes out because of the incompatibility of the aerodynamic model with the CPG basis. The CPG model outputs a continuous rhythmic signal, while the aerodynamic model developed in the current study gives the averaged values of the forces and moments, according to the mean wing kinematics that are inputted. To adapt the CPG to the aerodynamic model, averaged values of the CPG’s rhythmic output are provided to the aerodynamic model. However, because of the delay that occurred while calculating the mean value of the CPG signal, this adapting method reduced the supremacy of the CPGs in reaction time at mode transition. Therefore, if a more sophisticated CPG-based controller is desired to be simulated, including a realistic wing model, the aerodynamic model created in this study needs to be modified accordingly.

CHAPTER 6

FUTURE WORKS

The first thing to be done in the future is to create a more sophisticated CPG-based control algorithm that includes a wide range of danger and obstacle avoidance capabilities.

Since the stability of the biological flyers in the longitudinal and the lateral plane is provided passively by the vibration in the vertical axis, the need for constant feedback information for stability disappears, which yields less control effort. Power constraints, one of the significant problems in flapping flight, might be overcome by utilizing the vibrational stability effect of the high-frequency flapping motion. Therefore, benefiting from the vibrational stability phenomenon may enable the future flapping-wing MAVs to have operational capabilities.

In the scope of the work to be continued, a flapping-wing MAV control approach that utilizes the vibrational stability effect can be worked on together with a more sophisticated CPG-based control. With this consept, low power consumption levels will be aimed meanwhile sudden mode changes such as transition from hover to escape mode can be achieved by CPGs. This way, capabilities of the flapping-wing MAVs can get a little bit closer to the perfection behind the flight of the biological flyers.

REFERENCES

Agrawal, A., & Agrawal, S. K. (2009). Design of bio-inspired flexible wings for flapping-wing micro-sized air vehicle applications. Advanced Robotics, 23(7-8), 979-1002.

Ahmed, T., & Kurtuluş, D. F. (2021). Unsteady Aerodynamics of Cambered Airfoils at Low Reynolds Number. 10th Ankara International Aerospace Conference

Al-Mahasneh, A. J., Anavatti, S. G., & Garratt, M. A. (2017). Altitude identification and intelligent control of a flapping-wing micro aerial vehicle using modified generalized regression neural networks. In 2017 IEEE Symposium Series on Computational Intelligence (SSCI) (pp. 1-6). IEEE.

Animal Flight (2013). Startled Hawkmoth [Video]. YouTube. https://www.youtube.com/watch?v=BaE_KohggXQ

Ashraf, M., Lai, J., & Young, J. (2007). Numerical analysis of flapping-wing aerodynamics. 16th Australasian Fluid Mechanics Conference.

Au, L. T. K., Phan, H. V., Park, S. H., & Park, H. C. (2020). Effect of corrugation on the aerodynamic performance of three-dimensional flapping-wings. Aerospace Science and Technology, 105, 106041.

Aydemir, M., & Arıkan, K. B. (2020). Evaluation of the disturbance rejection performance of an aerial manipulator. Journal of Intelligent & Robotic Systems, 97(3-4), 451-469.

Aydemir, M. (2016). Disturbance Rejection Based Control of a Multirotor UAV. PhD Thesis, Mechatronics Engineering, Atılım University.

Bai, K., Luo, Y., Dan, Z., Zhang, S., Wang, M., Qian, Q., & Zhong, J. (2020). Extended State Observer based Attitude Control of a Bird-like Flapping-wing Flying Robot. Journal of Bionic Engineering, 17(4), 708-717.

Bal, C., Koca, G. O., Korkmaz, D., Akpolat, Z. H., & Ay, M. (2019). CPG-based autonomous swimming control for multi-tasks of a biomimetic robotic fish. Ocean Engineering, 189, 106334.

Banazadeh, A., & Taymourtash, N. (2016). Adaptive attitude and position control of an insect-like flapping-wing air vehicle. Nonlinear Dynamics, 85(1), 47-66.

Barnes, W. P., Gladden M. H. (2012). Feedback and motor control in invertebrates and vertebrates. Springer Science & Business Media.

Bayiz, Y. E., Hsu, S. J., Aguiles, A. N., Shade-Alexander, Y., & Cheng, B. (2019). Experimental Learning of a Lift-Maximizing Central Pattern Generator for a Flapping Robotic Wing. In 2019 International Conference on Robotics and Automation (ICRA) (pp. 1997-2003). IEEE.

Beddoes, T. S., (1984). Practical computation of unsteady lift. Vertica, Vol. 8, No.1, pp 55-71, Pergamon Press Ltd. UK.

Bektaş, M., Güler, M. A., & Kurtuluş, D. F. (2019). Numerical investigation of a Hawkmoth wing undergoing pure plunge motion in hover. 10th Ankara International Aerospace Conference

Bektaş, M. (2020). Biyo-esinlenmiş çırpan kanat modellerinin aeroelastik analizleri. Master's thesis, Mechanical Engineering, TOBB University of Economics and Technology.

Bektaş, M., Güler, M. A., & Kurtuluş, D. F. (2020). One-way FSI analysis of bio-inspired flapping-wings. International Journal of Sustainable Aviation, 6(3), 172-194.

Bennett, L. (1977). Clap and fling aerodynamics-an experimental evaluation. Journal of Experimental Biology, 69(1), 261-272.

Berg, C. V. D., & Ellington, C. P. (1997). The three–dimensional leading–edge vortex of a ‘hovering’model hawkmoth. Philosophical Transactions of the Royal Society of London. Series B: Biological Sciences, 352(1351), 329-340.

Bhatia, M., Patil, M., Woolsey, C., Stanfordx, B., & Beran, P. (2012). Lqr controller for stabilization of flapping-wing MAVs in gust environments. In AIAA Atmospheric Flight Mechanics Conference (p. 4867).

Bisplinghoff R. L., Ashley, H. (1996). Principles of Aeroelasticity, Dover Publications.

Biswal, S., Mignolet, M., & Rodriguez, A. A. (2019). Modeling and control of flapping-wing micro aerial vehicles. Bioinspiration & biomimetics, 14(2), 026004.

Biswal, S. (2015). Modeling and control of flapping-wing micro aerial vehicles. Master's thesis, Arizona State University.

Blom, J. D. (2010). Unmanned aerial systems: A historical perspective (Vol. 45). Kansas: Combat Studies Institute Press.

Bohorquez, F., Samuel, P., Sirohi, J., Pines, D., Rudd, L., & Perel, R. (2003). Design, analysis and hover performance of a rotary wing micro air vehicle. Journal of the American Helicopter Society, 48(2), 80-90.

Bouabdallah, S. (2007). Design and control of quadrotors with application to autonomous flying (No. THESIS). Epfl.

Calis, O., Arikan, K. B., & Kurtulus, D. F. (2019). Control of a flapping-wing micro air vehicle for navigation. 10th Ankara International Aerospace Conference

Calis, O., Arikan, K. B., & Kurtulus, D. F. (2021). Modeling the flapping motion via quasi-steady approach and controlling the longitudinal dynamics of a flapping-wing MAV. 11th Ankara International Aerospace Conference

Cao, Z., Zhang, D., Hu, B., & Liu, J. (2019). Adaptive path following and locomotion optimization of snake-like robot controlled by the central pattern generator. Complexity, 2019.

Cebeci, T., Platzer, M., Chen, H., Chang, K. C., & Shao, J. P. (2005). Analysis of low-speed unsteady airfoil flows. Springer Berlin Heidelberg.

Cheng, B., Deng, X., & Hedrick, T. L. (2011). The mechanics and control of pitching manoeuvres in a freely flying hawkmoth (Manduca sexta). Journal of Experimental Biology, 214(24), 4092-4106.

Cheng, B., & Deng, X. (2011). Translational and rotational damping of flapping flight and its dynamics and stability at hovering. IEEE Transactions on Robotics, 27(5), 849-864.

Chen, J., Yin, B., Wang, C., Xie, F., Du, R., & Zhong, Y. (2021). Bioinspired Closed-loop CPG-based Control of a Robot Fish for Obstacle Avoidance and Direction Tracking. Journal of Bionic Engineering, 18(1), 171-183.

Chin, D. D., & Lentink, D. (2016). Flapping-wing aerodynamics: from insects to vertebrates. Journal of Experimental Biology, 219(7), 920-932.

Chung, S. J., & Dorothy, M. (2010). Neurobiologically inspired control of engineered flapping flight. Journal of guidance, control, and dynamics, 33(2), 440-453.

Deng, X., Schenato, L., Wu, W. C., & Sastry, S. S. (2006a). Flapping flight for biomimetic robotic insects: Part I-system modeling. IEEE Transactions on Robotics, 22(4), 776-788.

Deng, X., Schenato, L., & Sastry, S. S. (2006b). Flapping flight for biomimetic robotic insects: Part II-flight control design. IEEE Transactions on Robotics, 22(4), 789-803.

Dickinson, M. H., & Gotz, K. G. (1993). Unsteady aerodynamic performance of model wings at low Reynolds numbers. Journal of experimental biology, 174(1), 45-64.

Dickinson, M. H., Lehmann, F. O., & Sane, S. P. (1999). Wing rotation and the aerodynamic basis of insect flight. Science, 284(5422), 1954-1960.

Du, G., & Sun, M. (2008). Effects of unsteady deformation of flapping-wing on its aerodynamic forces. Applied Mathematics and Mechanics, 29(6), 731-743.

Ellington, C. P. (1984). The aerodynamics of hovering insect flight. I. The quasi-steady analysis. Philosophical Transactions of the Royal Society of London. B, Biological Sciences, 305(1122), 1-15.

Ellington, C. P., Van Den Berg, C., Willmott, A. P., & Thomas, A. L. (1996). Leading-edge vortices in insect flight. Nature, 384(6610), 626-630.

Engels, T., Wehmann, H. N., & Lehmann, F. O. (2020). Three-dimensional wing structure attenuates aerodynamic efficiency in flapping fly wings. Journal of the Royal Society Interface, 17(164), 20190804.

Esfahani, J. A., Barati, E., & Karbasian, H. R. (2015). Fluid structures of flapping airfoil with elliptical motion trajectory. Computers & Fluids, 108, 142-155.

Etkin, B. (2005). Dynamics of atmospheric flight. Dover Publications.

Everaerts, J. (2008). The use of unmanned aerial vehicles (UAVs) for remote sensing and mapping. The International Archives of the Photogrammetry, Remote Sensing and Spatial Information Sciences, 37(2008), 1187-1192.

Fei, F., Tu, Z., Yang, Y., Zhang, J., & Deng, X. (2019, May). Flappy hummingbird: An open source dynamic simulation of flapping-wing robots and animals. In 2019 International Conference on Robotics and Automation (ICRA) (pp. 9223-9229). IEEE.

Ferdaus, M. M., Anavatti, S. G., Garratt, M. A., & Pratama, M. (2018). Development of c-means clustering based adaptive fuzzy controller for a flapping-wing micro air vehicle. Journal of Artificial Intelligence and Soft Computing Research, 9.

Frank, S. (2011). Vortex tilting and the enhancement of spanwise flow in flapping-wing flight. Master's thesis, Aerospace Engineering, University of Central Florida.

Galiński, C. (2006). Gust resistant fixed wing micro air vehicle. Journal of aircraft, 43(5), 1586-1588.

Gao, Z. (2006). Scaling and bandwidth-parameterization based controller tuning. In Proceedings of the American control conference (Vol. 6, pp. 4989-4996).

Garcia, H., Abdulrahim, M., & Lind, R. (2003). Roll control for a micro air vehicle using active wing morphing. In AIAA Guidance, Navigation, and Control Conference and Exhibit (p. 5347).

Greeter, J. S., & Hedrick, T. L. (2016). Direct lateral maneuvers in hawkmoths. Biology open, 5(1), 72-82.

Güçlü, A. (2020). Designing autopilot and guidance algorithms to control translational and rotational dynamics of a fixed wing VTOL UAV. PhD Thesis, Middle East Technical University.

Han, J. (2009). From PID to active disturbance rejection control. IEEE transactions on Industrial Electronics, 56(3), 900-906.

Han, J. S., & Han, J. H. (2019). A contralateral wing stabilizes a hovering hawkmoth under a lateral gust. Scientific reports, 9(1), 1-13.

Han, J. S., Chang, J. W., Kim, J. K., & Han, J. H. (2015a). Role of trailing-edge vortices on the hawkmothlike flapping-wing. Journal of Aircraft, 52(4), 1256-1266.

Han, J. S., Kim, J. K., Chang, J. W., & Han, J. H. (2015b). An improved quasi-steady aerodynamic model for insect wings that considers movement of the center of pressure. Bioinspiration & biomimetics, 10(4), 046014.

Han, J. H., & Nguyen, A. T. (2017). Dynamic stability of flapping-wing micro air vehicles with unsteady aerodynamic model. In Fluids Engineering Division Summer Meeting (Vol. 58042, p. V01AT01A002). American Society of Mechanical Engineers.

Han, J (1995). The" Extended State Observer" of a Class of Uncertain Systems [J]. Control and Decision, 1.

Hanrahan, S., (2006) Photo of a Manduca Sexta, Texas A&M University, Department of Entomology.

Hartmann, P., Ramseier, A., Gudat, F., Mihatsch, M. J., & Polasek, W. (1994). Normal weight of the brain in adults in relation to age, sex, body height and weight. Der Pathologe, 15(3), 165-170.

Hashemi, S. M., Botez, R. M., & Grigorie, L. T. (2020). Adaptive fuzzy control of chaotic flapping relied upon lyapunov-based tuning laws. In AIAA AVIATION 2020 FORUM (p. 3193).

He, W., Huang, H., Chen, Y., Xie, W., Feng, F., Kang, Y., & Sun, C. (2017). Development of an autonomous flapping-wing aerial vehicle. Science China Information Sciences, 60(6), 063201.

Hines, L. L., Arabagi, V., & Sitti, M. (2011). Free flight simulations and pitch and roll control experiments of a sub-gram flapping-flight micro aerial vehicle. In 2011 IEEE International Conference on Robotics and Automation (pp. 1-7). IEEE.

Ijspeert, A. J., & Crespi, A. (2007). Online trajectory generation in an amphibious snake robot using a lamprey-like central pattern generator model. In Proceedings 2007 IEEE International Conference on Robotics and Automation (pp. 262-268). IEEE.

Jadhav, S. S., Lua, K. B., & Tay, W. B. (2019). Effect of clap-and-fling mechanism on force generation in flapping-wing micro aerial vehicles. Bioinspiration & biomimetics, 14(3), 036006.

Jones, A. R., Medina, A., Spooner, H., & Mulleners, K. (2016). Characterizing a burst leading-edge vortex on a rotating flat plate wing. Experiments in Fluids, 57(4), 52.

Jones, K., Platzer, M., Jones, K., & Platzer, M. (1997). Numerical computation of flapping-wing propulsion and power extraction. In 35th Aerospace Sciences Meeting and Exhibit (p. 826).

Kara, S. E. (2014). Control of Two Wheel Self Stabilizing Mobile Robot With a Simple Arm. Master’s Thesis, Mechatronics Engineering, Atilim University.

Karásek, M., & Preumont, A. (2012a). Flapping flight stability in hover: A comparison of various aerodynamic models. International Journal of Micro Air Vehicles, 4(3), 203-226.

Karásek, M., & Preumont, A. (2012b). Simulation of flight control of a hummingbird like robot near hover. Engineering Mechanics, 322.

Katz, J., & Plotkin, A. (2001). Low-speed aerodynamics (Vol. 13). Cambridge university press.

Kaya, M., & Tuncer, I. H. (2007). Nonsinusoidal path optimization of a flapping airfoil. AIAA journal, 45(8), 2075-2082.

Keennon, M., Klingebiel, K., Won, H. (2012). Development of the nano hummingbird: A tailless flapping-wing micro air vehicle. 50th AIAA Aerospace Sciences Meeting including the New Horizons Forum and Aerospace Exposition, p. 588, doi: 10.2514/6.2012-588.

Kiehn, O., & Butt, S. J. (2003). Physiological, anatomical and genetic identification of CPG neurons in the developing mammalian spinal cord. Progress in neurobiology, 70(4), 347-361.

Kim, J. K., & Han, J. H. (2013). Control effectiveness analysis of the hawkmoth Manduca sexta: a multibody dynamics approach. International Journal of Aeronautical and Space Sciences, 14(2), 152-161.

Kim, J. K., & Han, J. H. (2014). A multibody approach for 6-DOF flight dynamics and stability analysis of the hawkmoth Manduca sexta. Bioinspiration & biomimetics, 9(1), 016011.

Kim, J. K., Han, J. S., Lee, J. S., & Han, J. H. (2015). Hovering and forward flight of the hawkmoth Manduca sexta: trim search and 6-DOF dynamic stability characterization. Bioinspiration & biomimetics, 10(5), 056012.

Kim, Y. C., & Manabe, S. (2001). Introduction to coefficient diagram method. IFAC Proceedings Volumes, 34(13), 147-152.

Koehler, C., Wischgoll, T., Dong, H., & Gaston, Z. (2011). Vortex visualization in ultra low Reynolds number insect flight. IEEE transactions on visualization and computer graphics, 17(12), 2071-2079.

Konstadinopoulos, P., Thrasher, D. F., Mook, D. T., Nayfeh, A. H., & Watson, L. (1985). A vortex-lattice method for general, unsteady aerodynamics. Journal of aircraft, 22(1), 43-49.

Krishna, S., Green, M. A., & Mulleners, K. (2018). Flowfield and force evolution for a symmetric hovering flat-plate wing. AIAA Journal, 56(4), 1360-1371.

Kurtulus, D. F., Farcy, A., & Alemdaroglu, N. (2004). Numerical calculation and analytical modelization of flapping motion in hover. In First European Micro Air Vehicle Conference and Flight Competition, Braunschweig Germany (pp. 13-14).

Kurtulus D. F. (2005) Numerical and experimental analysis of fapping motion in hover, application to micro air vehicles. Ph.D. thesis, Joint Ph.D thesis Poitiers University/ENSMA (Poitiers France) and METU (Ankara-Turkey)

Kurtulus, D. F., Farcy, A., & Alemdaroglu, N. (2005). Unsteady aerodynamics of flapping airfoil in hovering flight at low Reynolds numbers. In 43rd AIAA Aerospace Sciences Meeting and Exhibit (p. 1356).

Kurtulus, D. F., David, L., Farcy, A., & Alemdaroglu, N. (2006a). A parametrical study with laser sheet visualization for an unsteady flapping motion. In 36th AIAA Fluid Dynamics Conference and Exhibit (p. 3917).

Kurtulus, D. F., David, L., Farcy, A., & Alemdaroglu, N. (2006b). A parametrical study with laser sheet visualization for an unsteady flapping motion. In 36th AIAA Fluid Dynamics Conference and Exhibit (p. 3917).

Kurtulus, D. F., David, L., Farcy, A., & Alemdaroglu, N. (2008). Aerodynamic characteristics of flapping motion in hover. Experiments in Fluids, 44(1), 23-36.

Kurtulus D. F. (2011a) Introduction to micro air vehicles: concepts, design and applications, VKI LS 2011-04, Recent developments in unmanned aircraft systems, (UAS, including UAV and MAV), Ed. Carbonaro M., Decuypere R., ISBN-13 978-2-87516-017-1, pp. 219-255.

Kurtulus D. F. (2011b) Unsteady Aerodynamics of Flapping Aerofoils: Case Studies with Experimental, Numerical, Theoretical and Soft Computing Methods, Recent Developments in Unmanned Aircraft Systems (UAS, including UAV and MAV), VKI LS 2011-04, ISBN-13 978-2-87516-017- 1, p: 1-36, April 2011.

Kurtulus DF (2015) On the unsteady behavior of the flow around NACA 0012 airfoil with steady external conditions at Re=1000, International Journal of Micro Air Vehicles, Vol 7, No 3, pp 301-326

Kurtulus, D. F. (2016). On the wake pattern of symmetric airfoils for different incidence angles at Re= 1000. International Journal of Micro Air Vehicles, 8(2), 109-139.

Kurtulus, D. F. (2018). Aerodynamic loads of small-amplitude pitching NACA 0012 airfoil at Reynolds number of 1000. AIAA Journal, 56(8), 3328-3331.Küssner, H. G. (1936). Zusammenfassender Bericht über den instationären Auftrieb von Flügeln. Luftfahrtforschung, 13(12), 410-424.

Kurtulus D. F. (2019) Unsteady Aerodynamics of a Pitching NACA 0012 Airfoil at Low Reynolds number. International Journal of Micro Air Vehicles, Vol 11, pp 1-21, November 2019 doi:10.1177/1756829319890609.

Kurtulus, D. F. (2021). Vortex flow aerodynamics behind a symmetric airfoil at low angles of attack and Reynolds numbers. International Journal of Micro Air Vehicles, 13, 17568293211055653.

Kurtulus, D.F. (2022) Critical Angle and Fundamental Frequency of Symmetric Airfoils at Low Reynolds Numbers, Journal of Applied Fluid Mechanics Volume 15, Number 3, May 2022

La Mantia, M., & Dabnichki, P. (2009). Unsteady panel method for flapping foil. Engineering analysis with boundary elements, 33(4), 572-580.

Lee, J. S., Kim, J. K., & Han, J. H. (2015). Stroke plane control for longitudinal stabilization of hovering flapping-wing air vehicles. Journal of Guidance, Control, and Dynamics, 38(4), 800-806.

Lee, J. W., Nguyen, A. T., & Han, J. H. (2018). Longitudinal flight control of bioinspired flapping-wing micro air vehicle with extended unsteady vortex-lattice method. In 31st Congress of the International Council of the Aeronautical Sciences (ICAS 2018). ICAS, September.

Lehmann, F. O. (2004). The mechanisms of lift enhancement in insect flight. Naturwissenschaften, 91(3), 101-122.

Lehmann, F. O., Sane, S. P., & Dickinson, M. (2005). The aerodynamic effects of wing–wing interaction in flapping insect wings. Journal of Experimental Biology, 208(16), 3075-3092.

Leishman, J. G. (2002). Challenges in modeling the unsteady aerodynamics of wind turbines. In Wind Energy Symposium (Vol. 7476, pp. 141-167).

Lentink, D., & Dickinson, M. H. (2009). Rotational accelerations stabilize leading edge vortices on revolving fly wings. Journal of experimental biology, 212(16), 2705-2719.

Lentink, D. (2013). Flying like a fly. Nature, 498(7454), 306-307.

Liang, S., Song, B., Xuan, J., & Li, Y. (2020). Active disturbance rejection attitude control for the dove flapping-wing micro air vehicle in intermittent flapping and gliding flight. International Journal of Micro Air Vehicles, 12, 1756829320943085.

Lian, Y. (2009). Numerical investigation of boundary effects on flapping-wing study. In 47th AIAA Aerospace Sciences Meeting including The New Horizons Forum and Aerospace Exposition (p. 539).

Li, J., Li, R., & Zheng, H. (2016). Quadrotor modeling and control based on linear active disturbance rejection control. In 2016 35th Chinese Control Conference (CCC) (pp. 10651-10656). IEEE.

Li, L., Wang, H., & Cui, L. (2021). Attitude control of flapping-wing aircraft based on energy optimization and ESO. Biomimetic Intelligence and Robotics, 100005.

Liu, H., & Aono, H. (2009). Size effects on insect hovering aerodynamics: an integrated computational study. Bioinspiration & Biomimetics, 4(1), 015002.

Long, L. N., & Fritz, T. E. (2004). Object-oriented unsteady vortex lattice method for flapping flight. Journal of Aircraft, 41(6), 1275-1290.

Lua, K. B., Lee, Y. J., Lim, T. T., & Yeo, K. S. (2017). Wing–wake interaction of three-dimensional flapping-wings. AIAA journal, 55(3), 729-739.

Ma'arif, A., Cahyadi, A. I., Herdjunanto, S., & Wahyunggoro, O. (2020). Tracking control of high order input reference using integrals state feedback and coefficient diagram method tuning. IEEE Access, 8, 182731-182741.

Madangopal, R., Khan, Z. A., & Agrawal, S. K. (2006). Energetics-based design of small flapping-wing micro air vehicles. IEEE/ASME Transactions on Mechatronics, 11(4), 433-438.

Manabe, S. (1998). Coefficient diagram method. IFAC Proceedings Volumes, 31(21), 211-222.

Mao, S., & Gang, D. U. (2003). Lift and power requirements of hovering insect flight. Acta Mechanica Sinica, 19(5), 458-469.

Marden, J. H. (1987). Maximum lift production during takeoff in flying animals. Journal of experimental Biology, 130(1), 235-258.

Marder, E., & Bucher, D. (2001). Central pattern generators and the control of rhythmic movements. Current biology, 11(23), R986-R996.

McMichael, J. & Francis, Col. (1997). Micro Air Vehicles-Toward a New Dimension in Flight.

Miller, L. A., & Peskin, C. S. (2005). A computational fluid dynamics ofclap and fling'in the smallest insects. Journal of Experimental Biology, 208(2), 195-212.

Nakatani, Y., Suzuki, K., & Inamuro, T. (2016). Flight control simulations of a butterfly-like flapping-wing–body model by the immersed boundary–lattice Boltzmann method. Computers & Fluids, 133, 103-115.

Nakata, T., & Liu, H. (2012). Aerodynamic performance of a hovering hawkmoth with flexible wings: a computational approach. Proceedings of the Royal Society B: Biological Sciences, 279(1729), 722-731.

Newcome, L. R. (2004). Unmanned aviation: a brief history of unmanned aerial vehicles. AIAA.

Nguyen, A. T., & Han, J. H. (2018). Wing flexibility effects on the flight performance of an insect-like flapping-wing micro-air vehicle. Aerospace science and Technology, 79, 468-481.

Nguyen, A. T., Han, J. S., & Han, J. H. (2016). Effect of body aerodynamics on the dynamic flight stability of the hawkmoth Manduca sexta. Bioinspiration & biomimetics, 12(1), 016007.

Nise, N. S. (2020). Control systems engineering. John Wiley & Sons.

Ökmen, A. A., Arıkan, K. B., & Kurtuluş, D. F. Modeling of the Hawkmoth Wing and Its Implementation in a Flapping Wing Mechanism. 10th Ankara International Aerospace Conference

Pohly, J. A., Salmon, J. L., Bluman, J. E., Nedunchezian, K., & Kang, C. K. (2018). Quasi-Steady versus Navier–Stokes solutions of flapping-wing aerodynamics. Fluids, 3(4), 81.

Polykretis, I., Tang, G., & Michmizos, K. P. (2020). An astrocyte-modulated neuromorphic central pattern generator for hexapod robot locomotion on Intel's Loihi. In International Conference on Neuromorphic Systems 2020 (pp. 1-9).

Qin, L., Zhou, W., & Jiang, W. (2017). Active disturbance rejection control system design for quadrotor. In 2017 36th Chinese Control Conference (CCC) (pp. 6530-6534). IEEE.

Radke, A., & Gao, Z. (2006). A survey of state and disturbance observers for practitioners. In 2006 American Control Conference (pp. 6-pp). IEEE.

Ramamurti, R., & Sandberg, W. (2001). Simulation of flow about flapping airfoils using finite element incompressible flow solver. AIAA journal, 39(2), 253-260.

Rifai, H., Marchand, N., & Poulin, G. (2008). Bounded control of a flapping-wing micro drone in three dimensions. In 2008 IEEE International Conference on Robotics and Automation (pp. 164-169). IEEE.

Roccia, B. A., Preidikman, S., Massa, J. C., & Mook, D. T. (2013). Modified unsteady vortex-lattice method to study flapping-wings in hover flight. AIAA journal, 51(11), 2628-2642.

Sane, S. P., & Dickinson, M. H. (2002). The aerodynamic effects of wing rotation and a revised quasi-steady model of flapping flight. Journal of experimental biology, 205(8), 1087-1096.

Sane, S. P. (2003). The aerodynamics of insect flight. Journal of experimental biology, 206(23), 4191-4208.

Simpson, R. J., Palacios, R., & Murua, J. (2013). Induced-drag calculations in the unsteady vortex lattice method. AIAA journal, 51(7), 1775-1779.

Sims, T. W., Palazotto, A. N., & Norris, A. (2010). A structural dynamic analysis of a Manduca sexta forewing. International Journal of Micro Air Vehicles, 2(3), 119-140.

Shyy, W., Aono, H., Kang, C. K., & Liu, H. (2013). An introduction to flapping-wing aerodynamics (Vol. 37). Cambridge University Press.

Shyy, W., Trizila, P., Kang, C. K., & Aono, H. (2009). Can tip vortices enhance lift of a flapping-wing?. AIAA journal, 47(2), 289-293.

Smith, M., Wilkin, P., & Williams, M. (1996). The advantages of an unsteady panel method in modelling the aerodynamic forces on rigid flapping-wings. The journal of experimental biology, 199(5), 1073-1083.

Srygley, R. B., & Thomas, A. L. R. (2002). Unconventional lift-generating mechanisms in free-flying butterflies. Nature, 420(6916), 660-664.

Steuer, I., & Guertin, P. A. (2019). Central pattern generators in the brainstem and spinal cord: an overview of basic principles, similarities and differences. Reviews in the Neurosciences, 30(2), 107-164.

Sufiyan, D., Pheh, Y. H., Win, L. T. S., Win, S. K. H., Soh, G. S., & Foong, S. (2020). A central pattern generator-based control strategy of a nature-inspired unmanned aerial vehicle. In 2020 IEEE/ASME International Conference on Advanced Intelligent Mechatronics (AIM) (pp. 1641-1647). IEEE.

Suhail, S. A., Bazaz, M. A., & Hussain, S. (2019). Altitude and attitude control of a quadcopter using linear active disturbance rejection control. In 2019 International Conference on Computing, Power and Communication Technologies (GUCON) (pp. 281-286). IEEE.

Sun, C., Liu, M., Liu, C. A., Feng, X., & Wu, H. (2021). An Industrial Quadrotor UAV Control Method Based on Fuzzy Adaptive Linear Active Disturbance Rejection Control. Electronics, 10(4), 376.

Sun, M. (2014). Insect flight dynamics: stability and control. Reviews of Modern Physics, 86(2), 615.

Sun, M., & Wang, J. K. (2007). Flight stabilization control of a hovering model insect. Journal of Experimental Biology, 210(15), 2714-2722.

Sun, Z., Wu, L., Guo, Z., & Zhang, H. (2020). Research on Roll Attitude Control of UAV Based on Active Disturbance Rejection Control. In IOP Conference Series: Earth and Environmental Science (Vol. 428, No. 1, p. 012083). IOP Publishing.

Taha, H. E., Hajj, M. R., & Nayfeh, A. H. (2012). Flight dynamics and control of flapping-wing MAVs: a review. Nonlinear Dynamics, 70(2), 907-939.

Taha, H. E., Kiani, M., Hedrick, T. L., & Greeter, J. S. (2020). Vibrational control: A hidden stabilization mechanism in insect flight. Science robotics, 5(46), eabb1502-eabb1502.

Tan, W., & Fu, C. (2015). Linear active disturbance-rejection control: Analysis and tuning via IMC. IEEE Transactions on Industrial Electronics, 63(4), 2350-2359.

Tang, J., Viieru, D., & Shyy, W. (2008). Effects of Reynolds number and flapping kinematics on hovering aerodynamics. AIAA journal, 46(4), 967-976.

Theodorsen, T., & Mutchler, W. H. (1935). General theory of aerodynamic instability and the mechanism of flutter.

Trizila, P., Kang, C. K., Aono, H., Shyy, W., & Visbal, M. (2011). Low-Reynolds-number aerodynamics of a flapping rigid flat plate. AIAA journal, 49(4), 806-823.

Truong, Q. T., Nguyen, Q. V., Truong, V. T., Park, H. C., Byun, D. Y., & Goo, N. S. (2011). A modified blade element theory for estimation of forces generated by a beetle-mimicking flapping-wing system. Bioinspiration & biomimetics, 6(3), 036008.

Tuncer, I. H., & Platzer, M. F. (2000). Computational study of flapping airfoil aerodynamics. Journal of aircraft, 37(3), 514-520.

Usherwood, J. R., & Ellington, C. P. (2002). The aerodynamics of revolving wings I. Model hawkmoth wings. Journal of Experimental biology, 205(11), 1547-1564.

Verboom, J. L., Tijmons, S., De Wagter, C., Remes, B., Babuska, R., & de Croon, G. C. (2015). Attitude and altitude estimation and control on board a flapping-wing micro air vehicle. In 2015 IEEE International Conference on Robotics and Automation (ICRA) (pp. 5846-5851). IEEE.

Wagner, H. (1925) Uber die entstehung des dynamischen auftriebes von tragflügeln. Z. Angew. Math. Mech. 5, 17–35.

Wang, J., Han, P., Zhu, R., Liu, G., Deng, X., & Dong, H. (2018). Wake capture and aerodynamics of passively pitching tandem flapping plates. In 2018 Fluid Dynamics Conference (p. 3236).

Wang, Z. J., Birch, J. M., & Dickinson, M. H. (2004). Unsteady forces and flows in low Reynolds number hovering flight: two-dimensional computations vs robotic wing experiments. Journal of Experimental Biology, 207(3), 449-460.

Wang, Z., Gao, Q., & Zhao, H. (2017). CPG-inspired locomotion control for a snake robot basing on nonlinear oscillators. Journal of Intelligent & Robotic Systems, 85(2), 209-227.

Ward, T. A., Fearday, C. J., Salami, E., & Binti Soin, N. (2017). A bibliometric review of progress in micro air vehicle research. International Journal of Micro Air Vehicles, 9(2), 146-165.

Weis-Fogh, T. (1973). Quick estimates of flight fitness in hovering animals, including novel mechanisms for lift production. Journal of experimental Biology, 59(1), 169-230.

Wenfu, X. U., Erzhen, P. A. N., Juntao, L. I. U., Yihong, L. I., & Han, Y. U. A. N. (2021). Flight control of a large-scale flapping-wing flying robotic bird: System development and flight experiment. Chinese Journal of Aeronautics.

Willmott, A. P., & Ellington, C. P. (1997). The mechanics of flight in the hawkmoth Manduca sexta. I. Kinematics of hovering and forward flight. The Journal of experimental biology, 200(21), 2705-2722.

Wissa, B. E., Elshafei, K. O., & El-Badawy, A. A. (2020). Lyapunov-based control and trajectory tracking of a 6-DOF flapping-wing micro aerial vehicle. Nonlinear Dynamics, 99(4), 2919-2938.

Wright, J. R., & Cooper, J. E. (2015). Introduction to aircraft aeroelasticity and loads. 2nd edition, John Wiley & Sons.

Xie, F., Zhong, Y., Du, R., & Li, Z. (2019). Central pattern generator (CPG) control of a biomimetic robot fish for multimodal swimming. Journal of Bionic Engineering, 16(2), 222-234.

Xiong, Y., & Sun, M. (2009). Stabilization control of a bumblebee in hovering and forward flight. Acta Mechanica Sinica, 25(1), 13-21.

Xu, N., & Sun, M. (2014). Lateral dynamic flight stability of a model hoverfly in normal and inclined stroke-plane hovering. Bioinspiration & biomimetics, 9(3), 036019.

Yu, B., Kim, S., & Suk, J. (2019). Robust Control based on ADRC and DOBC for Small-Scale Helicopter. IFAC-PapersOnLine, 52(12), 140-145.

Żbikowski, R. (2002). On aerodynamic modelling of an insect–like flapping-wing in hover for micro air vehicles. Philosophical Transactions of the Royal Society of London. Series A: Mathematical, Physical and Engineering Sciences, 360(1791), 273-290.

Zhang, J., Cheng, B., & Deng, X. (2016). Instantaneous wing kinematics tracking and force control of a high-frequency flapping-wing insect MAV. Journal of Micro-Bio Robotics, 11(1), 67-84.

Zhang, Y. L., & Sun, M. (2010). Dynamic flight stability of hovering model insects: theory versus simulation using equations of motion coupled with Navier–Stokes equations. Acta Mechanica Sinica, 26(4), 509-520.

Zhu, G., Qi, J., & Wu, C. (2019). Landing control of fixed-wing uav based on adrc. In 2019 Chinese Control Conference (CCC) (pp. 8020-8025). IEEE.